University of Alberta

North Atlantic Ocean and Sea Ice Modeling and Data Assimilation

by

Sanjay S.P. Rattan

A thesis submitted to the Faculty of Graduate Studies and Research
in partial fulfillment of the requirements for the degree of

Doctor of Philosophy

Department of Earth and Atmospheric Sciences

Edmonton, Alberta
Spring, 2008

Library and Archives Canada

Published Heritage Branch

395 Wellington Street
Ottawa ON K1A 0N4
Canada

Bibliothèque et Archives Canada

Direction du Patrimoine de l'édition

395, rue Wellington
Ottawa ON K1A 0N4
Canada

Your file Votre référence
ISBN: 978-0-494-45587-6
Our file Notre référence
ISBN: 978-0-494-45587-6

NOTICE:
The author has granted a non-exclusive license allowing Library and Archives Canada to reproduce, publish, archive, preserve, conserve, communicate to the public by telecommunication or on the Internet, loan, distribute and sell theses worldwide, for commercial or non-commercial purposes, in microform, paper, electronic and/or any other formats.

The author retains copyright ownership and moral rights in this thesis. Neither the thesis nor substantial extracts from it may be printed or otherwise reproduced without the author's permission.

AVIS:
L'auteur a accordé une licence non exclusive permettant à la Bibliothèque et Archives Canada de reproduire, publier, archiver, sauvegarder, conserver, transmettre au public par télécommunication ou par l'Internet, prêter, distribuer et vendre des thèses partout dans le monde, à des fins commerciales ou autres, sur support microforme, papier, électronique et/ou autres formats.

L'auteur conserve la propriété du droit d'auteur et des droits moraux qui protège cette thèse. Ni la thèse ni des extraits substantiels de celle-ci ne doivent être imprimés ou autrement reproduits sans son autorisation.

In compliance with the Canadian Privacy Act some supporting forms may have been removed from this thesis.

While these forms may be included in the document page count, their removal does not represent any loss of content from the thesis.

Conformément à la loi canadienne sur la protection de la vie privée, quelques formulaires secondaires ont été enlevés de cette thèse.

Bien que ces formulaires aient inclus dans la pagination, il n'y aura aucun contenu manquant.

Canada

Abstract

A number of experiments have been performed with the Subpolar Ocean Model (SPOM) and the Nucleus for European Modeling of the Ocean (NEMO) coupled ocean-sea ice model to improve the models and then to utilize them for scientific process studies of the North Atlantic ocean and sea ice.

An important issue facing eddy-permitting models of the North Atlantic is salinity drift of the Labrador Sea. There are a number of causes for this problem mainly arising from misrepresentations of the export of sea-ice from the Arctic Ocean, river runoff, meltwater from the Greenland ice cap and salt transport originating from the eastern subpolar gyre. In this study we investigate the salt transport originating from the eastern subpolar gyre, using two solutions of the NEMO model with different water formations. Analysis shows a gradual progression of Subpolar Mode Water (SMPW) properties from the eastern subpolar gyre to the Labrador Sea through Cape Farewell, implying the eastern subpolar gyre as an important source of the salt for Labrador Sea.

In order to reduce the problem of model drift, we implement variable eddy transfer coefficient in the Gent and McWilliams eddy parameterization, and a recent semi-diagnostic assimilation method (SDV) in the SPOM model. The combined approach reduces the drift in freshwater content of the Labrador Sea almost completely, while simultaneously improving its circulation. Previous eddy-permitting modeling studies in the sub-polar North Atlantic have failed to provide accurate representation of circulations and freshwater content simultaneously. The SDV approach also represents the total and eddy heat and freshwater transports equally well.

The SDV approach is also implemented in the NATL4 configuration of the NEMO model. The configuration reproduces realistic large-scale spatial and seasonal variations of sea ice in terms of concentration, thickness and extent, in agreement with observations. NATL4 has also captured important ice features along Eastern Canadian and Greenland coasts, a deficiency observed in the few previous coupled ocean-sea ice modeling studies in this region. Two sensitivity studies performed show that the sea ice in the model is sensitive to both oceanic eddy parameterization and oceanic data assimilation, with sensitivity to former being larger.

Acknowledgement

I wish to thank firstly my supervisor Paul G. Myers. I am indebted to him for his guidance in the production of this thesis and the wealth of knowledge he shared with me on an understandable level. He also supported me through his research grants in the first 20 months of this study. Through his grants I also managed to attend a number of conferences and workshops where I presented results of this thesis: Canadian Meteorological and Oceanographic Society (CMOS) Conference in St. Johns, Newfoundland (2007), Sea Ice Workshop in Victoria (2006), Canadian CLIVAR (Climate Variability) Workshop in Victoria (2006), OPA/NEMO Ocean Modeling Workshop in Grenoble, France (2006), and Bedford Institute of Oceanography (2007).

I would also like to thank my supervisory committee members: Andrew G. Bush and John D. Wilson for monitoring my progress, providing me critical feedbacks on my performance and recommending me for a number of scholarships that helped me financially to complete this thesis.

Other financial support for this work was provided by National Science and Engineering Research Council of Canada (NSERC: $42, 000), Walter H. Jones Graduate Fellowship ($9, 572), Institute of Geophysics Dr. Hibbs Memorial Scholarship ($2,000), Institute of Geophysics Travel Award ($500), 3 terms of teaching assistantships provided by Department of Earth and Atmospheric Science, CMOS bursary ($250), and CMOS Edmonton Branch bursary ($150).

Table of Contents

Chapter 1: Introduction 1
1.1 Circulation 2
1.2 Water masses 5
1.3 Labrador Sea Water and North Atlantic Deep Water 7
1.4 Subpolar modeling 11
1.5 Sea Ice 14
1.6 Ocean Data Assimilation 16
1.7 Thesis outline/Plan 18
Bibliography 20
Chapter 2: Background on ocean modeling and ocean models 24
2.1 Equations of motion 24
2.2 Averaged equations of motion 28
2.3 Approximations and scaling 33
2.4 Horizontal tracer physics 36
2.5 Vertical physics 38
2.5.1 Turbulent kinetic energy equation 39
2.5.2 Convection 42
2.5.3 Vertical velocity 42
2.6 Boundary and initial conditions 43
2.6.1 Momentum fluxes 43
2.6.2 Heat and freshwater fluxes 44
2.6.3 Lateral boundary conditions 45
2.7 Semidiagnostic scheme 46
2.8 North Atlantic ocean models and configurations 47
2.8.1 Geopotential models 48
2.8.2 Isopycnal models 49
2.8.3 Sigma models 50
2.8.4 Hybrid models 50
2.8.5 Model intercomparison 51
2.9 Assessment and validation of results 56
Bibliography 58
Appendix 2.1 Reynolds decomposition 64
Appendix 2.2 Laws of diffusion 67
Appendix 2.3 Models of baroclinic instability 68
Appendix 2.4 Variable eddy diffusivity (κ) computation 70

Chapter 3: Role of eddies in heat and freshwater transport in the Labrador Sea 72
3.1 Introduction 72
3.2 Methods 75
3.3 Model 77
3.4 Results and discussion 78
3.4.1 Annual mean fields 79
3.4.2 Freshwater content 83

3.4.3 Role of eddies 85
3.4.3.1 Freshwater content 86
3.4.3.2 Heat transport 88
3.4.3.3 Freshwater transport 91
3.5 Summary 93
3.6 Acknowledgements 98
Bibliography 99
Chapter 4: Impact of Subpolar Mode Water on Labrador Sea Water formation 103
4.1 Introduction 103
4.2 Model description and experiments 106
4.3 Results 108
4.3.1 NATL4 108
4.3.2 Labrador Sea Water 110
4.3.3 Irminger Current 115
4.3.4 Subpolar Mode Water 116
4.3.5 Validation of results 120
4.4 Discussion and conclusion 121
4.5 Acknowledgements 123
Bibliography 124
Chapter 5: Sea ice representation in the NATL4 configuration of NEMO 128
5.1 Introduction 128
5.2 Model and method 130
5.3 Mean ice fields 133
5.3.1 Sea ice concentration 133
5.3.2 Sea ice thickness 138
5.3.3 Sea ice extent 141
5.4 Sensitivity analysis 143
5.4.1 Sensitivity to oceanic assimilation 143
5.4.2 Sensitivity to eddy representation 148
5.5 Summary and conclusion 155
5.6 Acknowledgements 157
Bibliography 158
Chapter 6: General discussion and conclusion 161
Bibliography 166

List of Tables

Table 2.1 Zonal momentum equation	33
Table 2.2 Meridional momentum equation	34
Table 2.3 Vertical momentum equation	34
Table 2.4 North Atlantic models	52
Table 2.5 North Atlantic models	52
Table 2.6 Tracer mixing schemes	53
Table 2.7 Momentum mixing schemes	54
Table 3.1 Summary of experiments	79
Table 3.2 Root mean square error	85
Table 3.3 Summary of results	98
Table 4.1 Summary of experiments	107
Table 4.2 Summary of validation of results	121
Table 5.1 Summary of experiments	133

List of Figures

Figure 1.1	Subpolar gyre circulation	3
Figure 3.1	Annual mean salinity fields	80
Figure 3.2	Annual mean salinity fields	81
Figure 3.3	Annual mean salinity fields	82
Figure 3.4	Labrador Sea box	83
Figure 3.5	Freshwater content	86
Figure 3.6	Upper layer freshwater content	87
Figure 3.7	Zonally integrated heat transport	89
Figure 3.8	Meridionally integrated heat transport	90
Figure 3.9	Zonally integrated freshwater transport	92
Figure 3.10	Meridionally integrated freshwater transport	93
Figure 3.11	Depth integrated freshwater transport	94
Figure 4.1	Salinity profiles	109
Figure 4.2	Transformation rates	111
Figure 4.3	Labrador Sea Water salinities and temperature	113
Figure 4.4	Mixed layer depth	114
Figure 4.5	Cape Farewell properties	117
Figure 4.6	Cape Farewell temperature and heat transport	118
Figure 4.7	Subpolar Mode Water salinities and temperature	119
Figure 5.1	Sea ice concentration for September and December	135
Figure 5.2	Sea ice concentration for March and June	136
Figure 5.3	Sea ice thickness	137
Figure 5.4	Sea ice extent	138
Figure 5.5	Region A (SDVar-Pvar) ice concentration	145
Figure 5.6	Region B (SDVar-Pvar)	146
Figure 5.7	Region C (SDVar-Pvar)	147
Figure 5.8	Region A (Pvar-PCon) ice concentration	149
Figure 5.9	Region A (Pvar-PCon) ocean surface currents	150
Figure 5.10	Region B (Pvar-PCon)	151
Figure 5.11	Region C (Pvar-PCon)	152

Glossary

baroclinic instability	Instability arising in rotating, stratified fluids that are subject to horizontal temperature gradient. In this process the available potential energy is converted to kinetic energy (of the eddies).
barotropic instability	The source of energy in this case is associated with the horizontal variations in the velocity of the mean flow (velocity or current shear).
B and C grids	Two forms of discretizations used to represent arrangement of variables in a numerical model in order to conserve properties in a numerical model.
configuration	A configuration is a subset of an ocean model built basically by differing horizontal and vertical grid resolutions, other numerical details and ocean physics.
data assimilation	Procedure in which observations are combined with model output whereby observations correct model errors and the models extrapolate the data information in space, and time, yielding a more complete picture.
diapycnal surface	Surface perpendicular to an isopycnal surface (cross-isopycnal).
divergence	An operator that measures the magnitude of a vector field's source or sink at a given point; the divergence of a vector field is a scalar.
eddy permitting	Ocean models whose grid resolution is smaller than coarse resolution climate models (i.e. smaller than about 1^{o} grid resolution) but larger than eddy resolving models: normally in the range $1/3^{o}$ -$1/9^{o}$.
eddy resolving	Ocean models whose grid resolution is smaller than the local Rossby radius of deformation, for example, lower than at most $1/10^{o}$ in the Labrador Sea.
geopotential coordinate	Z coordinate or height as a vertical coordinate.
gradient	The gradient of a scalar field is a vector field which points in the direction of the rate of increase of the scalar field and whose magnitude is the greatest rate of change.

hybrid coordinate	A combination of geopotential, sigma and height coordinates.
hydrography	Temperature and salinity properties of a water mass.
isopycnal coordinate	Constant density surfaces as a vertical coordinate.
isobaths	Contours of equal depths in the ocean.
isopycnal	Surface of constant density.
parameterization	The mathematical representation of unresolved processes.
sigma coordinate	Surfaces in this coordinate follow model terrain.
subgridscale	Processes that occur at dimensions smaller than the "resolvable" grid resolution.
thermohaline circulation	The global density driven circulation of the oceans, driven by the formation and sinking of deep water in the North Atlantic.

List of Abbreviations

1.5TC	1.5 Turbulent Closure Scheme
CFCAS	Canadian Foundation for Climate and Applied Science
CICE	Community Ice CodE
CIS	Canadian Ice Service
CME	Community Modeling Effort
COAPS	Center for Ocean-Atmospheric Prediction Studies
CTD	Conductivity, Temperature, Depth
DAMEE	Data Assimilation and Model Evaluation Experiment
DSOW	Denmark Straight Overflow Water
ECMWF	European Center for Medium-Range Weather Forecast
EGC	East Greenland Current
EGCC	East Greenland Counter Current
ETOPO5	Earth TOPOgraphy- 5 minute
FW	Fresh water
GFDL	Geophysical Fluid Dynamics Laboratory
HYCOM	Hybrid Coordinate Ocean Model
IC	Irminger Current
IPCC	International Panel on Climate Change
ISOW	Iceland Scotland Overflow Water
IW	Irminger Water
KPP	K-Profile Parameterization
KT	Kraus-Turner Parameterization
LC	Labrador Current
LHS	Left Hand Side
LIM	LouvaIn-la-Neuve
LODYC	Laboratoire d'Oceanographie DYnamique et Climatologie
LSW	Labrador Sea Water
MICOM	Miami Isopycnal Coordinate Ocean Model
MOC	Meridional Overturning Circulation
MY	Mellor-Yamada parameterization
NAC	North Atlantic Current
NADW	North Atlantic Deep Water
NAO	North Atlantic Oscillation
NCAR	National Center for Atmospheric Research
NEMO	Nucleus for European Modeling of the Ocean
NOAA	National Oceanic and Atmospheric Administration
NODC	National Oceanographic Data Center
NSERC	National Science and Engineering Research Council
OPA	Ocean PArallelise
PC	Prognostic Constant Scheme
POM	Princeton Ocean Model
POP	Parallel Ocean Program
PV	Prognostic Variable Scheme
RHS	Right Hand Side

RMSE	Root Mean Square Error
RRMW	Reykjanes Ridge Mode Water
SDC	Semidiagnostic Constant Scheme
SDV	Semidiagnostic Variable Scheme
SEACOOS	Southeast Atlantic Coastal Forecast System
SPC	Semiprognostic Constant Scheme
SPMW	Subpolar Mode Water
SPOM	Subpolar Ocean Model
SPV	Semiprognostic Variable Scheme
Sv	Sverdrup
TKE	Turbulent Kinetic Energy
UNESCO	United Nations Educational, Scientific and Cultural Organization
WGC	West Greenland Current

List of Symbols

ρ	Density
ρ_c	Climatological density
ρ_m	Model computed density
ρ_o	Average density of sea water
σ	Isopycnal
u	Zonal velocity
v	Meridional velocity
w	Vertical velocity
p	Pressure
u'	Zonal velocity (unresolved term)
v'	Meridional velocity (unresolved term)
w'	Vertical velocity (unresolved term)
p'	Pressure (unresolved term)
u^*	Gent and McWilliams zonal velocity
v^*	Gent and McWilliams meridional velocity
w^*	Gent and McWilliams vertical velocity
x	Coordinate axis in the ***i*** direction
y	Coordinate axis in the **j** direction
z	Coordinate axis in the **k** direction
F	Force
U	$= (u,v,w)$, 3 dimensional velocity vector
V	Volume
A_h	Horizontal viscosity coefficient
A_v	Vertical viscosity coefficient
K_h	Horizontal diffusivity coefficient
K_v	Vertical diffusivity coefficient
κ	Kappa; Gent and McWilliams eddy diffusivity coefficient
τ	Wind stress
τ_x	Zonal wind stress
τ_y	Meridional wind stress
s_{rho}	Isopycnal slope
T	Eady growth rate
L	Length scale of baroclinic zone
f	Coriolis parameter
Ri	Richardson number
g	Gravitational constant (=9.8 m/s^2)
S_r	Reference salinity (=35.0)
C_p	Specific heat capacity (4×10^{-3} J kg^{-1} $^oK^{-1}$)
T	Temperature
S	Salinity
Ω	Earth's angular acceleration (7.292×10^{-5} rad/s)
ϕ	Degrees latitude from the equator
t	Time
h_p	Height of a density surface
ε	Dissipation term of the turbulent kinetic energy equation

P_{rt}	Prandtl number
N	Brunt Vaisala frequency
l_k	Mixing turbulent length scale
l_e	Dissipation turbulent length scale
C_D	Drag coefficient
u_b	Bottom zonal velocity
e_b	Bottom turbulent kinetic energy
E	Evaporation rate
P	Precipitation rate
R	Runoff rate

Chapter 1

Introduction

The North Atlantic ocean is the best understood and most intensively studied of all the ocean basins in the world (Haine et al., 2007). The subpolar gyre which forms the northern part of this ocean basin, however, is not a very well understood region in comparison with the rest of the North Atlantic ocean. Its significance lies in it being the site for the formation of Labrador Sea Water (LSW) which plays an important role in the lower limb of the global thermohaline circulation (Dickson and Brown, 1994) that consequently affects earth's climate through redistribution of heat. The sub-polar gyre is enclosed mainly by land in the west (eastern Canada, Davis Strait and Hudson Strait), north (Greenland-Scotland Ridge) and east (European continental shelf) and by the North Atlantic Current (NAC) in the south. The basic ocean circulation structure of the subpolar gyre is set up by the large-scale atmospheric forcing and the underlying topography. During winter, it is also affected by the presence of sea ice in the northern and western areas. In this chapter a general discussion of the basic features of the subpolar gyre including circulation, water masses, LSW and North Atlantic Deep Water (NADW), subpolar gyre modeling, sea ice, and ocean data assimilation are described. A thesis outline is given in the final section of this chapter.

1.1 Circulation

The major currents in the subpolar gyre have been described by a number of early studies (Worthington, 1976; Olbers et al., 1985; Schmitz and McCartney, 1993) and recent studies (Cuny et al., 2002; Haine et al., 2007). The source of the warm and saline waters in the subpolar gyre is the NAC (Fig. 1) which enters near Newfoundland and travels almost longitudinally to the western European Basin. At this point some of the NAC flows past Ireland, the Faroes, and into the Norwegian Seas while the rest circulates along the Reykjanes Ridge to form the Irminger Current (IC) which eventually circulates the eastern subpolar gyre water mass cyclonically around the boundary of the Labrador Sea. The IC transports relatively warm ($3.5 - 6°C$) and salty (34.88-35.1) water in a jet following the continental slope and within about 100 km of the shelf break (Cuny et al., 2002). The mean transport of this water mass across a vertical crossection near Cape Farewell was estimated as 8.5-11 Sv (Clarke, 1984) while Pickart et al. (2005) estimated a transport of 13.6 Sv for the IC just east of Cape Farewell.

The importance of IC in the Labrador Sea lies in its role on Labrador Sea convection. This buoyant boundary current generates "Irminger eddies" that carry a large heat and freshwater flux from boundaries into the deep convection region (Katsman et al., 2004; Lilly et al., 2003; Straneo, 2006). The narrow and steep continental slope off southwest Greenland is a well-known source of eddies, playing a role during both pre and post convection periods (Cuny et al., 2002). Lilly et al. (1999) during their deployment of a mooring and float also observed eddy activity. Further, Lilly & Rhines (2002) identified two cyclones and four anticyclones at the Bravo moorring station in the Labrador Sea during June-Nov 1994. Warm cyclones appeared to originate in the Irminger boundary current, while cold anticyclones were products of deep convection. Hence these studies show that the water transported into the interior of the Labrador Sea is associated with the Irminger Current eddies, implying

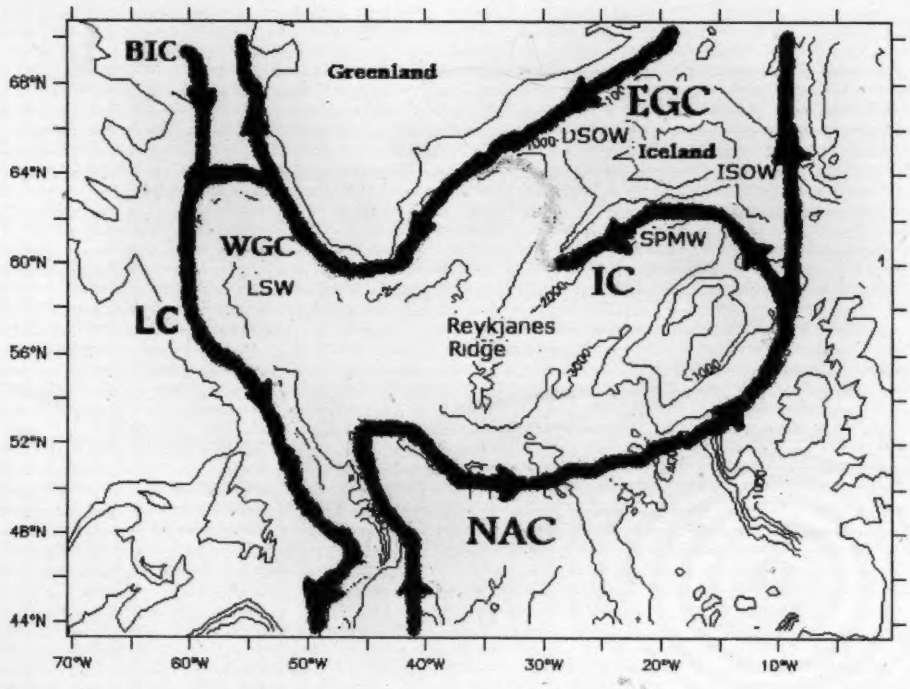

Figure 1.1: The subpolar gyre cartoon showing the major currents: North Atlantic Current (NAC), Irminger Current (IC), East Greenland Current (EGC), West Greenland Current (WGC), Labrador Current (LC), Baffin Island Current (BIC), and approximate locations of major water masses: Iceland-Scotland Overflow Water (ISOW), Denmark Strait Overflow Water (DSOW), Subpolar Mode Water (SPMW) and Labrador Sea Water (LSW). Also shown are depth contours at 1000 m intervals.

the significance of IC and its eddies on Labrador Sea deep convection.

The other important currents are the East and West Greenland Currents (EGC, WGC). Unlike the NAC and IC, the EGC and WGC are cold and fresh currents in the subpolar gyre, originating from the Nordic Seas. The EGC along its pathway from Fram Strait to Cape Farewell at the southernmost point of Greenland exchanges water with the Arctic and the Nordic seas (Rudels et al., 2002). At Fram Strait near a depth of 100m, temperatures could be as low as -1.5°C with a salinity of 34. 3 (Rudels et al., 2002) while further southwards near Denmark Strait temperatures rise to $3 - 6$°C and salinities increase to 34.75-34.85 (Holliday et al., 2006). Historical

estimates of volume transport of the EGC along the pathway are between 0.7-3 Sv (Pickart et al., 2005). A much lesser known current associated with the EGC and known as the East Greenland Coastal Current (EGCC) (having a volume transport of about 0.8-2 Sv; Pickart et al., 2005) follows closely the EGC but is closer towards the coast as the name implies (Holliday et al., 2007).

At the southern tip of Greenland, the EGC and EGCC merge and become the WGC that flows along the western coast of Greenland. The warm and salty IC lies below the cold and fresh WGC, and slightly offshore. The WGC flows northwestward along the Greenland shelf with a transport of roughly 3 Sv as measured at Cape Farewell (Clarke, 1984) and with an approximate speed of 35 cm/s obtained using surface drifters (Cuny et al., 2002). Near Cape Farewell, Cuny et al. (2002) found maximum speed using surface drifters in May 1997 of about 0.9 m/s which is consistent with Holliday et al. (2007) (using Acoustic Doppler Current Profiler data of August and September 2005) who have found 1.0 m/s. The temperature of WGC is about -1.8°C and salinity is about 34.5 (Cuny et al., 2002).

Along the Labrador Slope flows the Labrador Current (LC). It is a continuation of the Baffin Island Current (BIC) originating from Baffin Bay in the Canadian Archipelago. After the BIC passes Hudson Strait and begins to flow over the continental shelf and the upper slope off Labrador it is known as LC (Lazier and Wright, 1993). Although the water properties in BIC and LC (temperature of ~ -1.5°C and salinity ≤ 34; Cuny et al., 2002) are the same, there is a difference in their structure arising from a change in depth over which the BIC flows (600 m) to a shallower flowing LC (200 m) (Lazier and Wright, 1993). In the transition region between the Greenland and Labrador slopes, the currents have, on average, half the speed of the WGC (35 cm/s). Just north of the Hamilton Bank, the LC speed is 20 cm/s close to the 1000m isobath and 12cm/s above the lower slope (Lazier and Wright, 1993). The LC has a summer transport of around 11 Sv with an annual range of 4 Sv (Lazier and

Wright, 1993). Modified SPMW that has travelled to the Labrador basin by the IC is located below the LC and is also known as the deep LC (Lazier and Wright, 1993).

1.2 Water Masses

Underlying the surface circulation described in section 1.1 is locally formed intermediate Subpolar Mode Water (SPMW), although the exact number of water mass in the subpolar gyre varies due to naming variations or classifications in different studies (eg. Reynaud et al., 1995; Haine et al., 2007). SPMW is a general term for convectively formed water mass in the subpolar gyre (McCartney and Talley, 1982; Johnson and Gruber, 2007). It is characterized by a distinct thermostad (a region of reduced vertical temperature gradient-Johnson and Gruber, 2007; Hanawa and Talley, 2001). The strengths of these thermostads range from 8-10^oC in the eastern subpolar gyre to below 3.5^oC in the Labrador Sea. In the eastern subpolar gyre, the SPMW properties differ on its location with respect to the NAC. To the east of NAC, the SPMW is saltier, warmer and less stratified due to its formation by wintertime cooling while SPMW west of the NAC is cooler, fresher, denser and more stratified as it is influenced by the sub-Arctic intermediate water (Johnson and Gruber, 2007). The SPMW in the Labrador Sea being quite an extreme case of SPMW, is known as LSW. (From now onwards SPMW in the Labrador Sea will be refereed to as LSW, whereas SPMW in the eastern subpolar gyre will be mentioned simply as SPMW although a brief outline of the subdivisions of the eastern SPMW is mentioned in the following paragraphs in this section). A detailed description of LSW is outlined in the next section.

A form of SPMW which is an intermediate between LSW and the eastern SPMW is the Irminger Water (IW; Myers et al., 2007) or Irminger Sea Water (McCartney 1984; McCartney and Tally, 1984) since it passes the Irminger Basin of the eastern

subpolar gyre. The IW is essential to the convection process in the Labrador Sea as it is the heat source balancing the wintertime cooling to the atmosphere. It is thus part of the restratification process after convection and it keeps the Labrador Sea ice free (Lilly et al., 1999; Lazier 1973). The IW mass generally has temperatures and salinities within the range $3.5 - 6°C$ and 34.88-35.1 respectively (Cuny et al., 2002; Clarke, 1984; Reynaud et al., 1995; Ribergaard, 2006) with transport estimates of 8.5-11 Sv (Clarke, 1984) and 13.6 Sv (Pickart et al., 2005) from a total transport past Cape Farewell ranging 34 to 50 Sv (Clarke 1984; Gana and Provost 1993; Reynaud et al., 1995). The transport estimates vary due to the definition of the Greenland slope at Cape Farewell. Recent estimates also exist from two data sets used by Myers et al. (2007) to examine the historical variability of the IW along a section at Cape Farewell over the last 50 years. At Cape Farewell using data from International Council for the Exploration of the Sea (ICES) Myers et al. (2007) found that for the period 1984-2005 the IW transports are 3.8± 0.9 Sv, 7.5± 1.7 $\times 10^{13}$ J/s of heat, and 8.5± 1.8 mSv of freshwater referenced to 35. A significant variability in the salinity, size and position of the IW core over time were also found to exist (Myers et al., 2007) and is driven by the North Atlantic Oscillation (NAO). The low phase of the NAO was associated with enhanced heat losses in the eastern subpolar gyre that led to an increase in the production of IW, with a correlation coefficient between Cape Farewell volume transport and winter NAO index of -0.42 at 99% significance level (Myers et al., 2007).

A type of SPMW identified recently in the far eastern subpolar gyre along the eastern flank of the Reykjanes Ridge is known as the Reykjanes Ridge Mode Water (RRMW; Theirry and Mercier, 2007). It is formed between the 1000 m and 2000 m isobaths along the ridge with mean temperature and salinities of 7°C and 35.13 respectively. Unlike the other types of SPMW found in the subpolar gyre having an origin in the NAC, RRMW comes from the North Iceland Basin. Using CTD

data from 1990-2006, Theirry and Mercier (2007) have observed a large variability in temperature and salinity fields of this form of SPMW: the temperature and salinity increased by 1.41°C and 0.11 respectively from 1995 to 2003. Almost simultaneously Theirry and Mercier (2007) also observed NAO index dropping from large positive values to a large negative value (in 1996) and then rising again to positive values but not as large as in the pre-1996 period, implying (at least a statistical) link between RRMW properties and NAO. Hence the NAO driven variabilities in RRMW (Theirry and Mercier; 2007) and IW (Myers et al., 2007) imply that the SPMW is in large forced by the NAO.

Below the intermediate SPMW masses of the eastern subpolar gyre, LSW that has spread from the Labrador Sea is found (McCartney, 1992; Yashayaev et al., 2007). Further below the LSW, are deep water masses that form the deep component of the meridional overturning circulation (MOC). These water masses are formed in the Nordic Seas and flow over the Greenland-Iceland-Scotland ridge, hence being known as the overflow waters. The main channels for the overflow waters are Faroe Bank Channel in the east and the Denmark Strait in the west. The overflow water in the Faroe Bank Channel is known as the Iceland-Scotland Overflow Water (ISOW) whereas in the Denmark Strait is known as the Denmark Strait Overflow Water (DSOW). Saunders (2001) has summarized from a number of studies of the properties of the ISOW and DSOW. ISOW has mean temperatures of -0.7°C to 3°C and salinities of 34.9-35.1 while DSOW has mean temperatures of -1°C to 2°C and salinities of 34.7-35.0. For waters colder than 3°C mean volume transports of ISOW have been observed as 1.9 Sv whereas for waters colder than 2°C mean volume transports of DSOW have been observed as 2.5 Sv (Saunders, 2001).

1.3 Labrador Sea Water and North Atlantic Deep Water

LSW as mentioned earlier is a special type of SPMW found in the subpolar gyre. LSW is characteristically cold (temperature of 3.4°C) and fresh (salinity of 34.88) (Talley and McCartney, 1982) with a density of $\sigma = 27.74 - 27.80$ (for "classical LSW") while some authors further add an "upper LSW" (Pickart et al., 1996) with density of $\sigma = 27.68 - 27.74$. In density crossections it can be also seen as a layer of minimum density gradient or pycnostad (Lazier et al., 2002). The LSW can be traced at intermediate depths (500-2000 m) across the North Atlantic Ocean, to the south and to the east of the Labrador Sea (Cunningham and Haine, 1995; Sy et. al, 1997; Talley et al., 1982). It basically follows three pathways (Sy et al., 1997): northeastward in the Irminger basin, eastward near 50^oN latitude with several bifurcations east of the Mid-Atlantic Ridge, and southward as part of the Deep Western Boundary Current. Earlier studies have used indirect measurements to infer the residence time and pathways of the LSW within the basin. For example, Cunningham and Haine (1995) used minimum in potential vorticity as a tracer for LSW pathway. Direct measurements by Lavender et al (2000) using more than 200 subsurface floats show that about 40% of the floats from the region of deep convection in the Labrador Sea left the basin within one year and were rapidly transported in the anticyclonic flow to the Irminger basin, and also eastwards to the subpolar gyre, indicating the pathway of the LSW in agreement with earlier indirect inferences. The LSW is an important component of the climate system. Long-term variability in the formation process and subsequent spreading of these water masses may alter the meridional heat flux, a central component of the climate system.

Large variations in LSW properties also exist. Observation of temperature and salinity properties of the 1990s (Lazier et al., 2002) showed that in the first half of that decade (years 1990-1993) the mean temperature of the 500-2000 m layer had decreased by 0.1^oC and the salinity had increased by 0.01. For the period (1994-1999) and at a

depth of 1000 m Lazier et al. (2002) show temperature increases of about 0.5^oC and a salinity decrease of about 0.01. Yashayaev et al. (2007) also show LSW in the AR7 (his Fig. 1) crossections with salinities of 34.88-34.90 (1960), 34.84 (1994) and 34.84 (2004). The volumetric density curve (σ_2 - potential density anomaly referenced to 2000 dbar; Yashayaev et al., 2007) shows a large variability: increasing from 36.89 in 1987 to a peak of 36.96 in 1994, a decrease to 36.89 is achieved in just 4 years (in 1998) followed by further gradual decrease to 36.85 in 2005. A recent study by Myers and Donnelly (2007) also found a shift from formation in the range $\sigma > 27.725$ during the early 1990s to convection in the range $\sigma = 27.675 - 27.725$ in the later part of the 1990s, which again implies a change in the properties of the LSW: from classical to lighter upper LSW. Hence temperature and salinity properties from these various studies show a build up of LSW in 1987-1994 and a subsequent decrease in the following decade.

LSW is renewed locally through convective mixing during the winter (Marshall and Schott, 1999) and the depth of convection is proportional to the volume of LSW formed. The LSW can be traced at intermediate depths (500-2000 m) across the North Atlantic Ocean, although the convection depth varies from year to year and decade to decade (McCartney and Talley, 1984; Aagard et al., 1985; Dickson and Brown, 1994; Dickson et al., 1996). A number of studies (eg. Steffen and D-Assaro, 2002; Pickart et al., 2002; Lazier et al., 2002; Yashayaev et al., 2007) show large variations (100 m to 2400 m) in the maximum winter-time mixed layer depths observed in the Labrador Sea. Steffen and D-Assaro (2002) deployed Lagrangian floats in the interior of Labrador Sea, yielding maximum mixed layer depths of 990 db and 650 db respectively for the winters of 1997 and 1998. Data obtained by Pickart et al. (2002) during a cruise visit of the Labrador Sea in the winter of 1997 shows mixed layer depths of upto 1500 m. The AR7W (his Fig. 1) crossections in the Labrador Sea in Lazier et al. (2002) show the mixed layer depths upto 2300 m in 1990 to 1993 and

upto 1000 m from 1994 to 1999. Yashayaev et al. (2007) also show a large variability in mixed layer depths as evident from salinity crossections in their study: 2000 m in 1960, 2400 m in 1994 and 1300 m in 2004. The layer thickness of $\triangle\sigma_2 = 0.01\, kg\, m^{-3}$ volumetric curve (Yashayaev et al., 2007) correspondingly increases from 350 m in 1987 to a peak of 1100 m in 1994, a decrease to 300 m in 1998 followed by depths varying between 350 m and 750 m upto 2005. Hence these studies show a maximum mixed layer depth in 1994 followed by a gradual decline, consistent with the LSW temperature and salinity properties.

The varying properties of the LSW as stated above indeed imply that the formation rate of the LSW have undergone considerable change. Although it is harder to estimate, a time series of the LSW formation rate (amount of LSW formed over a period) has recently started to emerge. For the period 1988-1994 Rhein et al. (2002) obtained 8.1-10.8 Sv while a reduced formation rate of 1.8-2.4 Sv was obtained for the period 1995-1997 using chlorofluorocarbon (CFC) inventory data. Haine et al. (2003) obtained 7 Sv for 1986-1988 using modelling studies with CFC while Brandt et al. (2007) obtained 7.9 Sv for the same period using another model. Hydrographic data of Yashayaev and Clarke (2006) obtained 4.5 Sv for the period 1987-1992. For 2001-2003 period, Kieke et al. (2006) obtained a lower rate of formation of 2.5 Sv using CFC inventory data. The formation rate thus determined is also dependent on the method used for its calculation (eg., hydrography, model, tracers and surface fluxes). Nevertheless, all the studies show increased formation rate during the active convection of the early 1990s followed by a decrease. A summary of various formation rates is outlined by Haine et al. (2007). The most recent estimate of LSW formation rate of Myers and Donelly (2007) using surface fluxes also shows this trend. Formation rates of between 1.2 and 2.0 Sv for $\sigma > 27.725$ and 0.9 and 2.4 Sv for $\sigma = 27.675 - 27.725$ have been obtained over the years 1960-1999, with the densities indicating a change from classical to upper LSW.

The LSW plays a significant role in the production of North Atlantic Deep Water (NADW) (Dickson and Brown, 1994) which affects the MOC that drives the global thermohaline circulation. The importance of the global thermohaline circulation is that it redistributes heat and salt globally in the ocean, driven by ocean surface fluxes of heat and freshwater, and as a result is known to be involved in major changes in the earth's climate. Apart from the LSW, the other main contributor to the formation of the NADW is the Greenland-Iceland-Scotland overflow water (ISOW and DSOW). Other lesser contributions to NADW are SPMW, Antarctic Bottom Water and Mediterranean Water (Haine et al., 2007). In this study mostly the LSW and SPMW will be discussed especially in chapter 4.

The formation of NADW is a result of increase in ocean salinity arising from processes (especially deep convection and brine rejection) that affect the underlying salinity. LSW and SPMW are formed mostly through deep convection resulting from erosion of surface stratification during intense surface cooling and evaporation by strong winter winds (Talley and McCartney, 1982; Cuny et al., 2002). Brine rejection (Stossel et al., 2002) which occurs during the formation of sea ice when saltier brine is left behind, also leads to an increase in seawater salinity. The latter process highlights the significance of sea ice on NADW formation. The role of salinity on NADW formation also signals the significance of accurately representing salinity in ocean models. Excessive salt would lead to unreasonably high production of NADW. Conversely, freshwater added to the ocean through precipitation and melting sea ice weakens the NADW.

1.4 Sub-Polar Modeling

Numerous modeling studies have been performed to analyze the circulation in the sub-polar North Atlantic and the Labrador Sea (eg. Eden and Boning, 2002), however,

the prognostic three dimensional modeling in this region is still not as advanced as the mid-latitude and low-latitude regions (Myers, 2002). Models ranging from ocean models, coupled ocean-sea ice and coupled ocean-sea ice-atmosphere are being used. A coupled ocean-sea ice model would better represent freshwater fluxes than an ocean only model, while a coupled ocean-sea ice-atmosphere would even better represent air-sea fluxes than a coupled ocean-sea ice model but the emphasis on a coupled ocean-sea ice-atmosphere model is beyond the scope of this study.

Despite the various modeling work in the North Atlantic including the subpolar gyre there have been certain deficiencies in modeling, requiring further development. In the mid nineties Boning et al. (1995) using various runs of the Geophysical Fluid Dynamics Laboratory (GFDL) model (Bryan, 1969; Cox, 1984) ocean circulation model with different horizontal resolutions ($1/6^o - 1.2^o$), wind and thermohaline forcing, and mixing parameters showed that the mixing was always concentrated in the western boundary layer resulting in an underestimation of the meridional overturning circulation (MOC). Substantial improvements, however, were achieved using the Gent and McWilliams (GM, 1990) eddy parameterization. Willebrandt et al. (2001) further confirmed sensitivity of model simulations to mixing and other subgridscale processes in a comparison of three different types of numerical models (level, isopycnal and sigma) of the North Atlantic.

One of the modeling efforts known as the US-German "Community Modelling Effort (CME)" in support of the World Ocean Circulation Experiment (Boning and Bryan, 1996) found that the model failed to simulate the observed eddy variability (Treguier, 1992) in the northeastern parts of the subpolar gyre. Other aspects of modeling such as the simulation of the outflow of the ISOW and DSOW showed these outflows to be quite significant as they considerably influenced the MOC strength and structure (Willebrandt et al., 2001). By the late 1990's the majority of the simulations had been performed using the GFDL ocean model, and with the dependence

of model solutions on the parameterization of subgridscale processes (eg. Bryan, 1987) having been established, it emphasized the importance of subgridscale parameterization. Willebrandt et al. (2001) suggested that in order to reduce excessive diapycnal mixing, the GM (1990) parameterization could be used instead of the horizontal biharmonic diffusion scheme. Deacu and Myers (2005) implemented the GM (1990) parameterization in a subpolar ocean model (SPOM; Myers, 2002) and found improved circulation with considerable reduction in salinity drift in the subpolar gyre.

The effect of topography on ocean circulation was also mentioned in a number of studies (Willebrandt et al., 2001; Myers and Deacu, 2004). Willebrandt et al. (2001) found that local representations in topography would have large scale implications on pathway of the North Atlantic Current off Flemish Cap. Myers and Deacu (2004) found that with partial cell representation (Adcroft et al., 1997) where the bottom-most finite cell in each column was partially filled with topography the ocean circulation improved (but with deteriorated hydrography). A recent comparison of the subpolar gyre in four high resolution models (Treguier et al., 2005) also shows deteriorated hydrography in the Labrador Sea. Hence some of the modelling studies have not led to simultaneous improvements in circulation and hydrography which is quite important since LSW, SPMW and NADW formation as mentioned earlier are dependent on accurately representing hydrogaphy (especially salinity). Utilization of coupled ocean-sea ice models and data assimilation are two of the options that could be looked into in order to better represent freshwater processes and reduce model drift. As a result sea ice modeling and data assimilation discussions are outlined next.

1.5 Sea Ice

Sea ice is an important component of the coupled ocean-ice-atmosphere system. Modulating surface albedo, turbulent air-sea energy exchange, upper ocean stratification, transporting relatively fresh surface water equatorward, densifying water through brine rejection, and serving as an insulation between the atmosphere and the ocean (Derser et al., 2002; Parkinson et al., 1999) are some of its roles. It exhibits substantial interannual, seasonal and regional variability (Deser et al., 2002; Overland and Wang, 2007; Parkinson et al., 1999). A regional projection of sea ice by the International Panel on Climate Change Fourth Assessment Report (IPCC AR4) based on a comparison of 20 models shows a consistent loss of greater than 40% in sea ice area by 2050 for the North Atlantic, especially the Eastern Greenland coasts (Overland and Wang, 2007). This has important climatic, economic and ecological implications for the ice covered northern regions and therefore warrants a careful study.

In the North Atlantic during winter sea ice is found in the Gulf of St. Laurence, Labrador Sea, Buffin and Hudson Bays, and East Greenland Sea (Parkinson et al., 1999). In the Labrador Sea during winter (December-March) sea ice extends from the Davis Strait to the southwestern tip of Greenland and along the Labrador coast to Newfoundland and Gulf of St. Laurence. In the Hudson Bay, sea ice coverage continues for several months of the year due to enclosure by the Canadian Archipelago (Parkinson et al., 1999). Presence of sea ice is found even in the minimum sea ice coverage months of August to October in Hudson Bay. In the Greenland Sea sea ice extents range from a minimum of $0.35 \times 10^6 km^2$ in September to a maximum $0.92 \times 10^6 km^2$ in March (Parkinson et al., 1999). Large internannual variability in ice extents also exist on the Labrador coast and has been found to be related to sea surface temperature fluctuations in the subpolar North Atlantic (Deaser et al., 2002). Using ice extent data from 1978-1996 Parkinson et al. (1999) found Labrador Sea and Baffin Bay ice extents increasing from $1.3 \times 10^6 km^2$ in 1978 to $1.5 \times 10^6 km^2$ in

1996. Gulf of St. Laurence also showed variability ($0.18 - 0.25 \times 10^6 km^2$). However, opposite trends of sea ice extents have been found in Greenland Sea. Greenland Sea winter ice extents have been found to have decreased from $1 \times 10^6 km^2$ to $0.8 \times 10^6 km^2$ over the 19 year period (Parkinson et al., 1999) while no change was observed in the trend for the same period in Hudson Bay ($1.25 \times 10^6 km^2$).

A few modelling studies have been performed to analyze the climatological representation of sea ice in the sub-polar North Atlantic in coupled ocean-sea ice models (eg. Melia, 2002; Timmermann et al., 2005). Melia (2002) and Timmermann et al. (2002) used different coupled ocean-sea ice models to study the evolution of North Atlantic sea ice. These studies realistically captured the annual cycle of sea ice growth and decay, with modelled ice extent, thickness and drift being in close agreement with observations. However, fine details of sea ice representation in certain regions of the North Atlantic are still missing in these studies, requiring further modeling studies.

1.6 Ocean Data Assimilation

In data assimilation we invoke an optimal combination of model output and observations to determine the state of the ocean. On their own, insufficient and sparse observations provide an incomplete picture of the ocean, while a model always has deficiencies (both random and systematic) arising from numerical errors and dynamical approximations (Pinardi and Woods, 2002; Chassignet and Verron, 2006).

Though data assimilation is generally used for hindcasting and forecasting the ocean state it can be also used in prognostic 3D modeling of the ocean, to correct the ocean model by reducing bias and drifts in the model (Thompson et al., 2006; Greatbatch et al., 2004) through "nudging". Actually, all forms of Kalman Filter (Evensen, 2002) used widely in atmospheric data assimilation for weather forecasting correspond to "nudging" (Thompson et al., 2006). Early methods such as Sarmiento

and Bryan (1982) have used "nudging" by adding Newtonian relaxation terms to the tracer equations to assimilate climatological temperature and salinity into the ocean model. This method has proven very useful over the years. However, one serious drawback of this scheme is that while the model temperature and salinity are forced towards mean climatology the eddy field is not left to evolve freely. Two recent methods known as spectral nudging (Thompson et al., 2006) and the semidiagnostic approach (Zhai et al., 2004) have attempted to "nudge" temperature and salinity towards climatology without any constraints on the eddy field.

In spectral nudging (Thompson et al., 2006) the model is forced towards climatological temperature and salinity in predetermined (eg. seasonal) frequency and wave-number bands. This method, when applied to an eddy-permitting model of the North Atlantic, maintained a statistical steady state over the several decades of integration with no evidence of bias and drift, i.e. with reasonable agreement between model output and observations (Thompson et al., 2006). The other method, known as the semi-diagnostic method (Zhai et al., 2004), is a variant of the semi-prognostic method of Sheng et al. (2001). This method utilizes the climatological temperature and salinity fields to adjust the momentum balance of the model, while leaving the tracer equations fully prognostic and unconstrained, hence leaving the eddy fields to evolve freely. An advantage of the semi-diagnostic method (Zhai et al., 2004) over the semi-prognostic method (Sheng et al., 2001) and the corrected semi-prognostic method (Eden et al., 2004) is that it allows the large-scale mean flow of the model field to be fully constrained by climatology. However, in certain instances we do not require a full constraint to mean climatology but to a certain frequency band of the climatology (such as constraining only to the seasonal cycle and leaving higher frequency bands such as of the order of days to be free to evolve prognostically). In such cases we could use spectral nudging. Hence it appears that the spectral nudging approach could be extended to semidiagnostic/semiprognostic methods and a comparison be

made between these two schemes.

Apart from data assimilation other factors that could potentially contribute to the examination of or reduction of model drift are refined model grid resolution and improved subgridscale parameterizations. Recently Deacu and Myers (2005) succfessfully utilized an improved subgridscale parameterization scheme (Visbeck et at., 1997; Gent and McWilliams, 1990) in an ocean model, reducing the model drift. The combination of the improved subgridscale parameterization and a data assimilation procedure is a natural extension of earlier studies, and will be explored in this study in an ocean only model, and a coupled ocean-sea ice model. The impact of model drift will be shown in this study on two different types of models with different resolutions, with and without improved subgridscale parameterizations and ocean data assimilation.

1.7 Thesis Outline/Plan

The main objectives of this study are to improve an eddy-permitting ocean model and a coupled ocean-sea ice model of the North Atlantic, and to use the improved models for scientific process studies of the North Atlantic ocean and sea ice. Subgridscale parameterization, data assimilation and their impact on LSW, SPMW and NADW formation are some of the main topics of this study, although a comprehensive study pertaining to modeling of the North Atlantic ocean and sea ice is beyond the scope of this study. Hence we concentrate our attention on the following questions:

1. How can we reduce model salinity drift? Can we improve model hydrography and circulation simultaneously, while reducing the model drift?

2. What is the role of oceanic data assimilation and subgridscale parameterization on ocean hydrography and circulation? Does this combination reduce model drift?

3. What is the role of role oceanic eddies in heat and freshwater transport?

4. What is the role of different water masses in the subpolar gyre, how do they interact, and how do they affect NADW formation and consequently the meridional overturning circulation (MOC)?

5. What is the impact of oceanic subgridscale parameterization and oceanic data assimilation on sea ice properties such as concentration, thickness and extent?

In this study two eddy-permitting models will be used to study the subpolar North Atlantic. One is an ocean only model called the Subpolar Ocean Model (SPOM; Myers, 2002) while the other, called Nucleus for European Models of the Ocean (NEMO), is a coupled ocean-sea ice model (Madec, 1998). Further background on modeling and ocean models is outlined in chapter 2 which also serves as a general background to all the subsequent chapters. This thesis is written in a paper-based format with chapters 3-5 corresponding to a paper to be submitted to a journal. Chapter 3 discusses issues arising from questions 1-3 listed above, question 4 is discussed in chapter 4 while question 5 is discussed in chapter 5. A general discussion and conclusion is given in chapter 6.

Bibliography

[1] Adcroft, A., Hill, C., Marshall, J., 1997. Representation of topography by shaved cells in a height coordinate ocean model. Monthly Weather Review 125, 2293-2315.

[2] Blumberg, A.F., Mellor, G.L., 1987. A description of a three dimensional coastal ocean circulation model, three dimensional coastal ocean models, edited by N. Heaps, 208 pp, American Geophysical Union.

[3] Boning, C.W., Holland, W.R., Bryan, F.O., Danabasoglu, G., McWilliams, J.C., 1995. An overlooked problem in model simulations of the thermohaline and heat transport in the Atlantic ocean. Journal of climate 8, 515-523.

[4] Chassignet, E.P., Smith, L.T., Halliwell, G.R., Bleck, R., 2003. North Atlantic simulations with the Hybrid Coordinate Ocean Model (HYCOM): Impact of the vertical coordinate choice, reference pressure, and thermobaricity. Journal of Physical Oceanography 33, 2504-2526.

[5] Chassignet, E.P., Verron, J., 2005. Ocean weather forecasting: an integrated view of oceanography, Springer Ed., 577p.

[6] Cuny, J., Rhines, P.B., Niiler, P.P., Bacon, S., 2002. Labrador Sea boundary currents and the fate of Irminger Sea Water. Journal of Physical Oceanography 32, 627-647.

[7] Dickson, R.R., Brown, J., 1994. The production of North Atlantic Deep Water: sources, rates, pathways. Journal of Geophysical Research 99 (C6), 12319-12341.

[8] Evensen, G., 2002. Sequential data assimilation for nonlinear dynamics: the sensemble Klaman Filter in *Ocean forecasting- conceptual basis and applications,* Edited by Nadia Pinardi and John Woods.

[9] Fichefet, T., Morales Maqueda, M.A., 1997. Sensitivity of a global sea ice model to the treatment of ice thermodynamics and dynamics, Journal of Geophysical Research 102, 12609-12646.

[10] Gent, P.R., McWilliams, J.C., 1990. Isopycnal mixing in ocean circulation models. Jounal of Physical Oceanography 20, 150-155.

[11] Greatbatch, R.J., Sheng, J., Eden, C., Tang, L., Zhai, X., Zhao, J., 2004. The semi-prognostic method. Continental Shelf Research 24/18, 2149-2165.

[12] Griffies, S.M., Boning, C., Bryan, F.O., Chassignet, E.P., Gerdes, R., Hasumi, H., Hirst, A., Treguier, A., Webb, D., 2000: Developments in ocean climate modelling. Ocean Modelling 2, 123-192.

[13] Haine, T., Boning, C., Branch, P., Fischer, J., Funk, A., Kieke, D., Kvaleberg, E., Rhein, M., 2007. North Atlantic deep water transformation in the Labrador Sea, re-circulation through the subpolar gyre and discharge to the subtropics, in ASOF Science Book, edited by B. Dickson.

[14] Madec, G., Delecluse, P., Imbard, M., Levy, C., 1998. General circulation model reference manual, Notes de l'IPSL, Universite P. et M. Curie, B102 T15-ES, 4 place Jussie, Paris cedex 5, N°11, 91p.

[15] McCartney, M.S., 1984. Recirculating components to the deep boundary current of the northern North Atlantic. Progress in Oceanography 29, 283-383.

[16] McCartney, M.S., Talley, L.D., 1984. Warm-to-cold water conversion in the northern North Atlantic Ocean. Journal of physical oceanography 14, 922-935.

[17] Myers, P.G., 2002. SPOM: A regional model of the sub-polar North Atlantic. Atmosphere-Ocean 40, 445-463.

[18] Myers, P.G., and Deacu, D., 2004. Labrador sea freshwater content in a model with a partial cell topographic representation. Ocean modelling 6, pp. 359-377.

[19] Olbers, D.J., Wenzel, M., Willebrand, J., 1985. The influence of North Atlantic circulation patterns from climatological hydrographic data. Reviews of Geophysics 23, 313-356.

[20] Parkinson, C.L., Cavalieri, D.J., Gloersen, P., Zwally, H.J., Comiso, J., 1999. Arctic sea ice extents, areas, and trends, 1978-1996, Journal of Geophysical Research 104, 20837-20856.

[21] Pinardi, N., Woods, J., (Eds.) 2001. Ocean forecasting- conceptual basis and applications, Springer Verlag, Berlin, 496 pp.

[22] Pickart, R.S., Torres, D.J., Fratantoni, P.S., 2004. The East Greenland Spill Jet. Journal of Physical Oceanography 35, 1037-1053.

[23] Reynaud, T.H., Weaver, A.J., Greatbatch, R.J., 1995. Summer mean circulation of the northwestern Atlantic Ocean. Journal of Geophysical Research 100, 779-816.

[24] Rudels, B., Fahrbach, E., Meincke, J., Budeus, G., Eriksson, P., 2002. The east Greenland current and its contribution to the Denamark Strait overflow, ICES J. Mar. Sci. 59, 1133-1154.

[25] Saunders, P.M., 2001. The Dense Northern Overflows, in *Ocean Circulation and Climate,* edited by Siedler G, Church J and Gould J.

[26] Schmitz, W.J., McCartney, M.S., 1993. On the North Atlantic Circulation, Rev Geophys. 31, 29-49.

[27] Stössel, A., Yang, K., Kim, S., 2002. On the role of sea ice and convection in a global ocean model. Journal of physical oceanography 32, 1194-1208.

[28] Treguier, A.M., Theetten, S., Chassignet, E.P., Penduff, T., Smith, R., Talley, L., Beismann, J.O., Boning, C., 2005. The North Atlantic subpolar gyre in four high resolution models. Journal of Physical Oceanography 35, 757-774.

[29] Visbeck, M., Marshall, J., Haine, T., Spall, M., 1997. Specifications of eddy transfer coefficients in coarse-resolution ocean models, Journal of Physical Oceanography, 16, 680-693.

[30] Worthington, L.V., 1976. On the North Atlantic Circulation, 6, The John Hopkins Oceanographic Studies, 110 pp.

[31] Yashayaev, I.M., Bersch, M., van Aken, H.M., 2007. Spreading of the Labrador Sea Water to the Irminger Sea and Iceland Basin, Geophysical Research Letters 34, doi:10.1029/2006GL028999.

Chapter 2

Background on Ocean Modeling and Ocean Models

This chapter describes the primitive equations of ocean modeling and their decomposition into "resolved" and "unresolved" components. Important approximations such as incompressibility, Boussinesq, and hydrostatic are described before an outline of the lateral and vertical subgridscale parameterizations used in SPOM and NEMO models are discussed. Finally, a review of the major models of the North Atlantic ocean is presented. This chapter also presents a detailed description of the Gent and McWilliams parameterization of unresolved eddy motion in the ocean, variable eddy diffusivity coefficient and the semidiagnostic method which are the basis for the subsequent chapters.

2.1 Equations of Motion

The ocean, following the fundamental principles of fluid dynamics, can be represented by a set of equations: the continuity equation, the Navier Stokes equations (covering the three components of the motion), an equation for state and two equations for tracers (temperature and salinity). In this study, the equations used in the

two models (SPOM and NEMO) are written in spherical coordinates. For simplicity, the equations discussed here are written in the rectangular Cartesian latitude-longitude coordinates as:

(i) continuity equation:

$$\frac{\partial \rho}{\partial t} + \frac{\partial}{\partial x}(\rho u) + \frac{\partial}{\partial y}(\rho v) + \frac{\partial}{\partial z}(\rho w) = 0 \tag{2.1}$$

and in the vectorial form ($\mathbf{U} = (u, v, w)$) as:

$$\frac{\partial \rho}{\partial t} + \nabla \cdot (\rho \mathbf{U}) = 0 \tag{2.2}$$

where u, v, w are velocities in the x, y, z axes respectively and ρ is density. The "grad" (∇) operator is given as $(\frac{\partial}{\partial x}, \frac{\partial}{\partial y}, \frac{\partial}{\partial z})$. Since the ocean can be described as an incompressible fluid (Haidvogel and Beckmann, 1999; Kantha and Clayson, 2000a), ρ can be represented as a constant reference value ρ_0 ($\sim 1035\,\mathrm{kgm}^{-3}$; Kantha and Clayson, 2000a) and as a result the continuity equation reduces to:

$$\frac{\partial u}{\partial x} + \frac{\partial v}{\partial y} + \frac{\partial w}{\partial z} = \nabla \cdot \mathbf{U} = 0 \tag{2.3}$$

Thus the velocity divergence vanishes in an incompressible fluid. This (Eq. 2.3) is the form of continuity equation used in the two models in this study. Hence continuity equations in our models are equations of conservation of volume (Eq. 2.3) rather than mass (Eq. 2.2). The effect of neglecting the term $\frac{\partial \rho}{\partial t}$ from the continuity equation would have an effect on the calculation of vertical velocity w in a hydrostatic model (discussed in section 2.3) and sea level height (Greatbatch, 1994; Mellor and Ezer, 1995). However, these effects are not significant at basin scale ocean modeling as in this study.

(ii) Navier Stokes equations:

$$\frac{\partial u}{\partial t} + u\frac{\partial u}{\partial x} + v\frac{\partial u}{\partial y} + w\frac{\partial u}{\partial z} = -\frac{1}{\rho}\frac{\partial p}{\partial x} + fv - (2\Omega\cos\phi)w$$
$$\frac{\partial v}{\partial t} + u\frac{\partial v}{\partial x} + v\frac{\partial v}{\partial y} + w\frac{\partial v}{\partial z} = -\frac{1}{\rho}\frac{\partial p}{\partial y} - fu$$
$$\frac{\partial w}{\partial t} + u\frac{\partial w}{\partial x} + v\frac{\partial w}{\partial y} + w\frac{\partial w}{\partial z} = -\frac{1}{\rho}\frac{\partial p}{\partial z} - g + (2\Omega\cos\phi)u$$

where p is pressure; f is the Coriolis parameter ($f = 2\Omega\sin\phi$, $\Omega = 7.292 \times 10^{-5}$ rad/s, ϕ is in degrees latitude from the equator); and g is gravitational acceleration.

In ocean modeling, an important approximation known as the Boussinesq approximation is imposed on the Navier Stokes equations. This common assumption arises from the fact that in the world oceans the variations of density ρ are usually less than $\pm 2.5\%$ of the average density ρ_0 (Mellor and Ezer, 1995). The Boussinesq approximation takes into account the density variations in the context of buoyancy forces while it ignores density variations elsewhere. As a result the variable ρ is replaced by ρ_0 in the horizontal momentum equations (Kantha and Clayson, 2000a). In the vertical momentum equation, density ρ is replaced by $\rho = \rho_o + \hat{\rho}$ where $\hat{\rho}$ is variation of density from the average ρ_o. A similar definition also exists for pressure variations in the ocean: $p = p_o + \hat{p}$. The consequence of this on the bouyancy term (assuming (Holton, 1992) that $\frac{\hat{\rho}}{\rho_o} \ll 1$, $\frac{1}{(\rho_o+\hat{\rho})} \cong \frac{1}{\rho_o}\left(1 - \frac{\hat{\rho}}{\rho_o}\right)$, and $\frac{dp_o}{dz} = \rho_o g$) is as follows:

$$\begin{aligned} -\frac{1}{\rho}\frac{\partial p}{\partial z} - g &= -\frac{1}{(\rho_o+\hat{\rho})}\frac{\partial}{\partial z}(p_o + \hat{p}) - g \\ &\approx \frac{1}{\rho_o}\left(\frac{\hat{\rho}}{\rho_o}\frac{dp_o}{dz} - \frac{\partial \hat{p}}{\partial z}\right) \\ &= -\frac{1}{\rho_o}\left(\hat{p}g + \frac{\partial \hat{p}}{\partial z}\right) \\ &= -\frac{\hat{\rho}}{\rho_o}g - \frac{1}{\rho_o}\frac{\partial \hat{p}}{\partial z} \end{aligned}$$

Taking Boussinesq approximation into account the Navier Stokes equations then become:

$$\begin{aligned} &\frac{\partial u}{\partial t} + u\frac{\partial u}{\partial x} + v\frac{\partial u}{\partial y} + w\frac{\partial u}{\partial z} = -\frac{1}{\rho_o}\frac{\partial p}{\partial x} + fv - (2\Omega\cos\phi)w \\ &\frac{\partial v}{\partial t} + u\frac{\partial v}{\partial x} + v\frac{\partial v}{\partial y} + w\frac{\partial v}{\partial z} = -\frac{1}{\rho_o}\frac{\partial p}{\partial y} - fu \\ &\frac{\partial w}{\partial t} + u\frac{\partial w}{\partial x} + v\frac{\partial w}{\partial y} + w\frac{\partial w}{\partial z} = -\frac{\hat{\rho}}{\rho_o}g - \frac{1}{\rho_o}\frac{\partial \hat{p}}{\partial z} + (2\Omega\cos\phi)u \end{aligned} \tag{2.4}$$

The Boussinesq approximation when applied to ocean models implies incompressibility that leads to conservation of volume rather than mass in ocean models. The approximation has an effect on sea surface height through volumetric expansion and cooling arising from seasonal cooling and heating. In Boussinesq ocean models, the effect is corrected by a spatially uniform time dependent factor calculated from the volume-averaged density change (Greatbatch,1994; Mellor and Ezer, 1995).

(iii) tracer equations:

$$\begin{aligned} \frac{\partial T}{\partial t} + u\frac{\partial T}{\partial x} + v\frac{\partial T}{\partial y} + w\frac{\partial T}{\partial z} &= R^* \\ \frac{\partial S}{\partial t} + u\frac{\partial S}{\partial x} + v\frac{\partial S}{\partial y} + w\frac{\partial S}{\partial z} &= S^* \end{aligned} \tag{2.5}$$

where T is potential temperature and S is salinity, R^* is the divergence of (subgrid) radiative heat fluxes due to sunlight penetration and S^* is the divergence of (subgrid) freshwater fluxes due to precipitation. The above equations (eg. for T) can be also written in the flux form for conservation of properties during discretization as:

$$\frac{\partial T}{\partial t} + \frac{\partial}{\partial x}(uT) + \frac{\partial}{\partial y}(vT) + \frac{\partial}{\partial z}(wT) = T^*$$

(iv) equation of state:

$$\rho = \varrho(T, S, p) \tag{2.6}$$

The equation of state is an empirically derived complex polynomial (Jackett and McDougall, 1995; UNESCO, 1983).

Further it should be noted that the above equations of motion were derived following two additional assumptions made from scale analysis (Haidvogel and Beckmann, 1999; Holton, 1992; Kantha and Clayson, 2000a):

(i) spherical earth approximation: the geopotential surfaces are assumed to be spheres so that gravity is parallel to earth's radius.

(ii) thin shell approximation: the ocean depth is neglected compared to the earth's radius.

2.2 Averaged Equations of Motion

In order to solve the equations of motion numerically finite spatial grid intervals (represented by $\triangle x$, $\triangle y$, $\triangle z$ in the x, y, and z directions respectively) and a finite temporal grid (represented by $\triangle t$, the model time step) are required. Averages of the finite dimensions of a grid represent the "resolved" component of the equations while dimensions smaller than these are the "unresolved" component. To represent this formally, we decompose a variable r into a "resolved" part $\bar{r}$ (a mean component) and an "unresolved" part r' (a fluctuating component) such that $r = \bar{r} + r'$, where the averaging operator is defined by a grid-volume average representing a "resolved" field:

$$\bar{r}(x,y,z,t) = \frac{1}{(\triangle t)(\triangle x)(\triangle y)(\triangle z)} \int_{t-\frac{1}{2}\triangle t}^{t+\frac{1}{2}\triangle t} \int_{x-\frac{1}{2}\triangle x}^{x+\frac{1}{2}\triangle x} \int_{y-\frac{1}{2}\triangle y}^{y+\frac{1}{2}\triangle y} \int_{z-\frac{1}{2}\triangle z}^{z+\frac{1}{2}\triangle z} r(x',y',z',t')\, dz'\, dy'\, dx'\, dt'$$

Now we also need to include the effects of the "unresolved" component in a numerical model so that the effects of the "unresolved" component on the "resolved" part could be explicitly represented. This could be done through Reynolds averaging, a method of representing a variable as an average and a fluctuation from that average (Holton, 1992). Before averaging the equations of motion let's first stipulate (Haidvogel and Beckmann, 1999) that for any variable r or any two variables r_1 and r_2 the following properties hold for the idealised Reynolds averaging process:

$\overline{r'} = 0$; $\quad \bar{\bar{r}} = \bar{r}$; $\quad \overline{\bar{r}_1 r_2'} = 0$; $\quad \overline{\bar{r}_1 \bar{r}_2} = \bar{r}_1 \bar{r}_2$; $\quad \overline{r_1' r_2'} \neq 0$

Let's first decompose all the variables in the equations of motion by the Reynolds method:

$u = \bar{u}+u'$; $v = \bar{v}+v'$; $w = \bar{w}+w'$; $p = \bar{p}+p'$; $\hat{p} = \bar{\hat{p}}+\hat{p}'$; $\rho = \bar{\rho}+\rho'$; $\hat{\rho} = \bar{\hat{\rho}}+\hat{\rho}'$

Substituting these decomposed terms into the total equations of motion (section 2.1), taking an average of the equations (an ensemble average: different from the temporal and spatial averaging; Kantha and Clayson, 2000b) and then applying the averaging postulates given above yields the averaged (mean) equations of motion (for details of the derivation see Appendix 2.1):

$$\frac{\partial \bar{u}}{\partial t} + \bar{u}\frac{\partial \bar{u}}{\partial x} + \bar{v}\frac{\partial \bar{u}}{\partial y} + \bar{w}\frac{\partial \bar{u}}{\partial z} = -\frac{1}{\rho_0}\frac{\partial \bar{p}}{\partial x} + f\bar{v} - (2\Omega\cos\phi)\bar{w} - \left[\frac{\partial}{\partial x}\left(\overline{u'u'}\right) + \frac{\partial}{\partial y}\left(\overline{u'v'}\right) + \frac{\partial}{\partial z}\left(\overline{u'w'}\right)\right].$$

$$\frac{\partial \bar{v}}{\partial t} + \bar{u}\frac{\partial \bar{v}}{\partial x} + \bar{v}\frac{\partial \bar{v}}{\partial y} + \bar{w}\frac{\partial \bar{v}}{\partial z} = -\frac{1}{\rho_0}\frac{\partial \bar{p}}{\partial y} - f\bar{u} - \left[\frac{\partial}{\partial x}\left(\overline{v'u'}\right) + \frac{\partial}{\partial y}\left(\overline{v'v'}\right) + \frac{\partial}{\partial z}\left(\overline{v'w'}\right)\right]$$

$$\frac{\partial \bar{w}}{\partial t} + \bar{u}\frac{\partial \bar{w}}{\partial x} + \bar{v}\frac{\partial \bar{w}}{\partial y} + \bar{w}\frac{\partial \bar{w}}{\partial z} = -\frac{\bar{\hat{\rho}}}{\rho_o}g - \frac{1}{\rho_o}\frac{\partial \bar{\hat{p}}}{\partial z} + (2\Omega\cos\phi)\bar{u} - \left[\frac{\partial}{\partial x}\left(\overline{w'u'}\right) + \frac{\partial}{\partial y}\left(\overline{w'v'}\right) + \frac{\partial}{\partial z}\left(\overline{w'w'}\right)\right]$$

$$\frac{\partial u}{\partial x} + \frac{\partial v}{\partial y} + \frac{\partial w}{\partial z} = 0$$

$$\begin{aligned} \frac{\partial \overline{T}}{\partial t} + \bar{u}\frac{\partial \overline{T}}{\partial x} + \bar{v}\frac{\partial \overline{T}}{\partial y} + \bar{w}\frac{\partial \overline{T}}{\partial z} &= -\left[\frac{\partial}{\partial x}\left(\overline{u'T'}\right) + \frac{\partial}{\partial y}\left(\overline{v'T'}\right) + \frac{\partial}{\partial z}\left(\overline{w'T'}\right)\right] + \overline{R^*} \\ \frac{\partial \overline{S}}{\partial t} + \bar{u}\frac{\partial \overline{S}}{\partial x} + \bar{v}\frac{\partial \overline{S}}{\partial y} + \bar{w}\frac{\partial \overline{S}}{\partial z} &= -\left[\frac{\partial}{\partial x}\left(\overline{u'S'}\right) + \frac{\partial}{\partial y}\left(\overline{v'S'}\right) + \frac{\partial}{\partial z}\left(\overline{w'S'}\right)\right] + \overline{S^*} \end{aligned} \qquad (2.7)$$

Compared to the total equations (section 2.1) our new set of "averaged" equations (Eq. 2.7) have additional terms represented in square brackets, involving the effects of transport by the unresolved velocity fluctuations or "turbulence" on the mean state and mean motion. These are known as "unresolved" eddy (subgridscale) terms whereas the rest are the "resolved" terms. The "unresolved" or fluctuating components

(after being multiplied by ρ_o) are called Reynolds stresses (forces/unit area) in the momentum equations. Similar terms in the heat and salt transport equations are known as Reynolds fluxes (transports/unit area). Further, due to our earlier adoption of the Boussinesq approximation, the density flux terms such as $\overline{\rho' u'}$ are missing completely from the horizontal momentum and the continuity equations. The effect of these terms on basin scale ocean modeling as in this study would be negligible (Greatbatch, 1994; Mellor and Ezer, 1995).

Comparing the total equations (section 2.1) with Eq. 2.7 the additional variables (more unknowns than the number of equations) that have arisen in Eq. 2.7 due to the "unresolved" fluxes need to be parameterized. This is known as the closure problem. In order to close the equations, by analogy with the molecular case (molecular diffusion) the eddy diffusion model or K-theory parameterizes the fluxes (such as $\overline{u'u'}$) in terms of the mean velocity gradients by some sort of "viscosity" eg. $-\overline{u'u'} = A_{xx}\frac{\partial \overline{u}}{\partial x}$. (Note that for a horizontally uniform ocean, where $\frac{\partial \overline{u}}{\partial x} = 0$, this closure assumption implies that the subgridscale fluxes lead to the false result $-\overline{u'u'} = 0$, hence this is an example where this simple closure assumption breaks down.) The generalized form of this closure (K-theory) is normally written in tensorial form for the three momentum equations as:

$$\overline{u_i' u_j'} = A_{ij}\frac{\partial \overline{u_i}}{\partial x_j}$$

whereas for the tracer equations as:

$$\overline{u_i' T'} = K_i \frac{\partial \overline{T}}{\partial x_i}$$

$$\overline{u_i' S'} = K_i \frac{\partial \overline{S}}{\partial x_i}$$

K-theory is the simplest and the most widely used closure schemes. It states that tracer and momentum diffusions occur down the large scale ("resolved") gradients,

by analogy with Fick's Law of diffusion (see Appendix 2.2). The coefficients such as A_{xx} are called eddy viscosities while their counterparts in the tracer equations (K_x, K_y, K_z) are known as eddy diffusivities. Replacing the eddy flux divergences in the equations of motion with the parameterized terms yields:

$$\begin{aligned}
&\frac{\partial \bar{u}}{\partial t} + \bar{u}\frac{\partial \bar{u}}{\partial x} + \bar{v}\frac{\partial \bar{u}}{\partial y} + \bar{w}\frac{\partial \bar{u}}{\partial z} = -\frac{1}{\rho_0}\frac{\partial \bar{p}}{\partial x} + f\bar{v} - (2\Omega\cos\phi)\bar{w} \\
&\quad + \left[\frac{\partial}{\partial x}\left(A_{xx}\frac{\partial \bar{u}}{\partial x}\right) + \frac{\partial}{\partial y}\left(A_{xy}\frac{\partial \bar{u}}{\partial y}\right) + \frac{\partial}{\partial z}\left(A_{xz}\frac{\partial \bar{u}}{\partial z}\right)\right] \\
&\frac{\partial \bar{v}}{\partial t} + \bar{u}\frac{\partial \bar{v}}{\partial x} + \bar{v}\frac{\partial \bar{v}}{\partial y} + \bar{w}\frac{\partial \bar{v}}{\partial z} = -\frac{1}{\rho_0}\frac{\partial \bar{p}}{\partial y} - f\bar{u} \\
&\quad + \left[\frac{\partial}{\partial x}\left(A_{yx}\frac{\partial \bar{v}}{\partial x}\right) + \frac{\partial}{\partial y}\left(A_{yy}\frac{\partial \bar{v}}{\partial y}\right) + \frac{\partial}{\partial z}\left(A_{yz}\frac{\partial \bar{v}}{\partial z}\right)\right] \\
&\frac{\partial \bar{w}}{\partial t} + \bar{u}\frac{\partial \bar{w}}{\partial x} + \bar{v}\frac{\partial \bar{w}}{\partial y} + \bar{w}\frac{\partial \bar{w}}{\partial z} = -\frac{\bar{\rho}}{\rho_o}g - \frac{1}{\rho_o}\frac{\partial \bar{p}}{\partial z} + (2\Omega\cos\phi)\bar{u} \\
&\quad + \left[\frac{\partial}{\partial x}\left(A_{zx}\frac{\partial \bar{w}}{\partial x}\right) + \frac{\partial}{\partial y}\left(A_{zy}\frac{\partial \bar{w}}{\partial y}\right) + \frac{\partial}{\partial z}\left(A_{zz}\frac{\partial \bar{w}}{\partial z}\right)\right] \\
&\frac{\partial \bar{u}}{\partial x} + \frac{\partial \bar{v}}{\partial y} + \frac{\partial \bar{w}}{\partial z} = 0 \\
&\frac{\partial \overline{T}}{\partial t} + \bar{u}\frac{\partial \overline{T}}{\partial x} + \bar{v}\frac{\partial \overline{T}}{\partial y} + \bar{w}\frac{\partial \overline{T}}{\partial z} = \left[\frac{\partial}{\partial x}\left(K_x\frac{\partial \overline{T}}{\partial x}\right) + \frac{\partial}{\partial y}\left(K_y\frac{\partial \overline{T}}{\partial y}\right) + \frac{\partial}{\partial z}\left(K_z\frac{\partial \overline{T}}{\partial z}\right)\right] + \overline{R^*} \\
&\frac{\partial \overline{S}}{\partial t} + \bar{u}\frac{\partial \overline{S}}{\partial x} + \bar{v}\frac{\partial \overline{S}}{\partial y} + \bar{w}\frac{\partial \overline{S}}{\partial z} = \left[\frac{\partial}{\partial x}\left(K_x\frac{\partial \overline{S}}{\partial x}\right) + \frac{\partial}{\partial y}\left(K_y\frac{\partial \overline{S}}{\partial y}\right) + \frac{\partial}{\partial z}\left(K_z\frac{\partial \overline{S}}{\partial z}\right)\right] + \overline{S^*}
\end{aligned} \tag{2.8}$$

Note that we have assumed that the salt and heat diffusivities are the same. Since in the ocean, the vertical length scale (H = 10^3 m) is much smaller than the horizontal length scale (L = 10^6 m) we could separate the eddy viscosity term A_{ij} into a horizontal A_h and a vertical component A_v, implying $A_h \gg A_v$. We can also neglect the off diagonal diapycnal terms, leaving us with A_{ij} as a diagonal matrix (Haidvogel and Beckmann, 1999) with only the three principal axes (components) of the tensor. There is no reason a priori why one could not have "cross diffusion" (off diapycnal terms), however, this formulation is the most common because there is no observa-

tional evidence suggesting the necessity to include the off-diagonal components of the (full) eddy diffusivity tensor. For spatially and temporally constant viscosity and diffusivity coefficients, the gradients of the fluxes could be represented as Laplacians (∇^2) and the full form of the equations of motion is then (the over bar ($\bar{}$) representing mean "resolved" variables from now onwards are being suppressed to simplify notation and will be regarded as being implicit):

$$\begin{aligned}
\frac{\partial u}{\partial t} + u\frac{\partial u}{\partial x} + v\frac{\partial u}{\partial y} + w\frac{\partial u}{\partial z} &= -\frac{1}{\rho_0}\frac{\partial p}{\partial x} + fv - (2\Omega\cos\phi)w \\
&+ \left[A_h\left(\frac{\partial^2 u}{\partial x^2} + \frac{\partial^2 u}{\partial y^2}\right) + A_v\left(\frac{\partial^2 u}{\partial z^2}\right)\right] \\
\\
\frac{\partial v}{\partial t} + u\frac{\partial v}{\partial x} + v\frac{\partial v}{\partial y} + w\frac{\partial v}{\partial z} &= -\frac{1}{\rho_0}\frac{\partial p}{\partial y} - fu \\
&+ \left[A_h\left(\frac{\partial^2 v}{\partial x^2} + \frac{\partial^2 v}{\partial y^2}\right) + A_v\left(\frac{\partial^2 v}{\partial z^2}\right)\right] \\
\\
\frac{\partial w}{\partial t} + u\frac{\partial w}{\partial x} + v\frac{\partial w}{\partial y} + w\frac{\partial w}{\partial z} &= -\frac{\rho}{\rho_o}g - \frac{1}{\rho_o}\frac{\partial \hat{p}}{\partial z} + (2\Omega\cos\phi)u \\
&+ \left[A_h\left(\frac{\partial^2 w}{\partial x^2} + \frac{\partial^2 w}{\partial y^2}\right) + A_v\left(\frac{\partial^2 w}{\partial z^2}\right)\right] \\
\\
\frac{\partial u}{\partial x} + \frac{\partial v}{\partial y} + \frac{\partial w}{\partial z} &= 0 \\
\\
\frac{\partial T}{\partial t} + u\frac{\partial T}{\partial x} + v\frac{\partial T}{\partial y} + w\frac{\partial T}{\partial z} &= \left[K_h\left(\frac{\partial^2 T}{\partial x^2} + \frac{\partial^2 T}{\partial y^2}\right) + K_v\left(\frac{\partial^2 T}{\partial z^2}\right)\right] + R^* \\
\frac{\partial S}{\partial t} + u\frac{\partial S}{\partial x} + v\frac{\partial S}{\partial y} + w\frac{\partial S}{\partial z} &= \left[K_h\left(\frac{\partial^2 S}{\partial x^2} + \frac{\partial^2 S}{\partial y^2}\right) + K_v\left(\frac{\partial^2 S}{\partial z^2}\right)\right] + S^*
\end{aligned} \tag{2.9}$$

Most ocean models have at least the laplacian option for tracer and momentum diffusions. The Laplacian term has been derived by virtue of having adopted eddy diffusion closure with a constant, and diagonal eddy viscosity/diffusivity tensor. Far more plausible and realistic turbulence closures are available across the spectrum of fluid mechanics research, and in particular, the assumption that the eddy diffusivity is not a function of position and of the (resolved) state of the ocean is completely unrealistic, although it is widely used. Some models (such as SPOM and NEMO) also

have a biharmonics (∇^4) option. This is another method of dissipating momentum through the use of a fourth order operator that acts more strongly on the small scales than the Laplacian operator, and less strongly on the large scales i.e. it is more "scale selective" than the ∇^2 operator (Hunke et al., 2008). In this study SPOM and NEMO models utilize biharmonics operator for horizontal momentum diffusion and the Gent and McWilliams parameterization (described later) for tracer diffusion. The vertical eddy viscosity (A_v) and diffusivity (K_v) coefficients in both models are calculated using more sophisticated schemes outlined in section 2.5.

2.3 Approximations and Scaling

We have already subjected the primitive equations to Boussinesq approximation and assumed that the ocean is incompressible. In ocean modeling there are further assumptions made before the primitive equations are discretised and modeled. In order to simplify the equations further we utilize scale analysis and eliminate terms that are relatively much smaller than some defined length and time scales.

As an illustration of scale analysis, the scale analysis of the primitive equations for mid-latitude large-scale motions are shown in Tables 2.1-2.3. The following characteristic scales have been utilized: horizontal velocity scale ($U : 10^{-1}\,\mathrm{m/s}$), vertical velocity scale ($W : 10^{-4}\,\mathrm{m/s}$), horizontal length scale ($L : 10^{6}\,\mathrm{m}$), vertical length scale ($H : 10^{3}\,\mathrm{m}$), typical timescale ($T : 10^{6}\,\mathrm{s}$), typical pressure ($P : 10^{7}\,\mathrm{Pa}$), density scale ($\rho : 1000\,\mathrm{kg\,m^{-3}}$), Coriolis parameter ($f : 10^{-4}\,\mathrm{s^{-1}}$), horizontal eddy viscosity ($A_h : 10 - 10^{5}\,\mathrm{m^2/s}$), vertical eddy viscosity ($A_v : 10^{-5} - 10^{-1}\,\mathrm{m^2/s}$), horizontal eddy diffusivity ($K_h : 10 - 10^{5}\,\mathrm{m^2/s}$), vertical eddy diffusivity ($K_v : 10^{-5} - 10^{-1}\,\mathrm{m^2/s}$).

$\frac{\partial u}{\partial t}$	$\frac{U}{T}$	$\frac{10^{-1}}{10^{6}}$	10^{-7}
$u\frac{\partial u}{\partial x}$	$U\frac{U}{L}$	$10^{-1}\frac{10^{-1}}{10^{6}}$	10^{-8}
$v\frac{\partial u}{\partial y}$	$U\frac{U}{L}$	$10^{-1}\frac{10^{-1}}{10^{6}}$	10^{-8}
$w\frac{\partial u}{\partial z}$	$W\frac{U}{H}$	$10^{-4}\frac{10^{-1}}{10^{3}}$	10^{-8}
$\frac{1}{\rho_0}\frac{\partial p}{\partial x}$	$\frac{1}{\rho}\frac{P}{L}$	$\frac{1}{10^{3}}\frac{10^{1}}{10^{3}}$	10^{-5}
fv	fU	$10^{-4}10^{-1}$	10^{-5}
$(2\Omega\cos\phi)w$	ΩW	$10^{-4}10^{-4}$	10^{-8}
$A_h\left(\frac{\partial^2 u}{\partial x^2}+\frac{\partial^2 u}{\partial y^2}\right)$	$A_h\frac{U}{L^2}$	$10^{5}\frac{10^{-1}}{10^{12}}$	10^{-8}
$A_v\left(\frac{\partial^2 u}{\partial z^2}\right)$	$A_v\frac{U}{H^2}$	$10^{-1}\frac{10^{-1}}{10^{6}}$	10^{-8}

Table 2.1: Scale analysis of the zonal momentum equation.

$\frac{\partial v}{\partial t}$	$\frac{U}{T}$	$\frac{10^{-1}}{10^{6}}$	10^{-7}
$u\frac{\partial v}{\partial x}$	$U\frac{U}{L}$	$10^{-1}\frac{10^{-1}}{10^{6}}$	10^{-8}
$v\frac{\partial v}{\partial y}$	$U\frac{U}{L}$	$10^{-1}\frac{10^{-1}}{10^{6}}$	10^{-8}
$w\frac{\partial v}{\partial z}$	$W\frac{U}{H}$	$10^{-4}\frac{10^{-1}}{10^{3}}$	10^{-8}
$\frac{1}{\rho_0}\frac{\partial p}{\partial y}$	$\frac{1}{\rho}\frac{P}{L}$	$\frac{1}{10^{3}}\frac{10^{1}}{10^{3}}$	10^{-5}
fu	fU	$10^{-4}10^{-1}$	10^{-5}
$A_h\left(\frac{\partial^2 v}{\partial x^2}+\frac{\partial^2 v}{\partial y^2}\right)$	$A_h\frac{U}{L^2}$	$10^{5}\frac{10^{-1}}{10^{12}}$	10^{-8}
$A_v\left(\frac{\partial^2 v}{\partial z^2}\right)$	$A_v\frac{U}{H^2}$	$10^{-1}\frac{10^{-1}}{10^{6}}$	10^{-8}

Table 2.2: Scale analysis of the meridional momentum equation.

$\frac{\partial w}{\partial t}$	$\frac{W}{T}$	$\frac{10^{-4}}{10^{6}}$	10^{-10}
$u\frac{\partial w}{\partial x}$	$U\frac{W}{L}$	$10^{-1}\frac{10^{-4}}{10^{6}}$	10^{-11}
$v\frac{\partial w}{\partial y}$	$U\frac{W}{L}$	$10^{-1}\frac{10^{-4}}{10^{6}}$	10^{-11}
$w\frac{\partial w}{\partial z}$	$W\frac{W}{H}$	$10^{-4}\frac{10^{-4}}{10^{3}}$	10^{-11}
$\frac{1}{\rho}\frac{\partial p}{\partial z}$	$\frac{1}{\rho}\frac{P}{H}$	$\frac{1}{10^{3}}\frac{10^{1}}{10^{3}}$	10^{1}
$\frac{1}{\rho_o}\frac{\partial \hat{p}}{\partial z}$	$\frac{\hat{p}}{\rho_o H}$	$\frac{1}{10^{3}}\frac{10^{5}}{10^{3}}$	10^{-1}
g	g	10^{1}	10^{1}
$\frac{\hat{\rho}}{\rho_o}g$	$\frac{0.025\rho_o}{\rho_o}g$	10^{-1}	10^{-1}
$(2\Omega\cos\phi)u$	ΩU	$10^{-4}10^{-1}$	10^{-5}
$A_h\left(\frac{\partial^2 w}{\partial x^2}+\frac{\partial^2 w}{\partial y^2}\right)$	$A_h\frac{W}{L^2}$	$10^{5}\frac{10^{-4}}{10^{12}}$	10^{-11}
$A_v\left(\frac{\partial^2 w}{\partial z^2}\right)$	$A_v\frac{W}{H^2}$	$10^{-1}\frac{10^{-4}}{10^{6}}$	10^{-11}

Table 2.3: Scale analysis of the vertical momentum equation.

From the scale analysis, the zonal and meridional momentum equations show that

the major terms are pressure gradient and zonal and meridional Coriolis accelerations for large scale midlatitude motions. A balance between these two forces is known as geostrophic balance. However, for basin scale ocean modeling since the other terms are only 2-3 orders smaller at large scales (but are significant, for example, at oceanic fronts) we retain all the terms (except the terms with coefficients $2\Omega\cos\phi$) in the zonal and momentum equations for modeling. The Coriolis acceleration terms with the coefficient $2\Omega\cos\phi$ present in the zonal and vertical momentum equations are not utilized in modeling and is a reasonable approximation not only for midlatitude and polar modeling but also for equatorial modeling. Near the equator although the $2\Omega\cos\phi$ term is larger it does not affect non-eddy resolving modeling (Marshall et al., 1997) but does affect high resolution (about $< 10\,\text{km}$ resolution) modeling (Marshall et al., 1997) and needs to be retained in the latter case.

In the vertical momentum equation the major terms are the vertical pressure gradient and gravity. The other terms are 6-12 orders smaller and are normally neglected in non-eddy resolving models. Rewriting the vertical momentum equation yields:

$$\frac{\partial \hat{p}}{\partial z} = -\hat{\rho} g \tag{2.10}$$

The vertical momentum equation has been reduced to a balance between the vertical pressure gradient and a buoyancy force. This is known as the hydrostatic approximation and is widely used in basin and global non-eddy resolving models eg. SPOM and NEMO. This assumption breaks down for a gridlength somewhere between 1-10 km, as the horizontal velocities become comparable with its vertical velocities (Marshall et al., 1997). Hence for eddy resolving modeling the assumption is not valid. Further, even in non-eddy resolving models nonhydrostatic assumption is important in the surface layers of the ocean especially in regions with strong vertical velocity such as the Labrador Sea during open winter time convection, and regions of strong

coastal upwelling. In order to reasonably represent such nonhydrostatic processes, hydrostatic ocean models use sophisticated vertical parameterizations as discussed in section 2.5. Further, since the hydrostatic assumption has eliminated the vertical acceleration term the procedure to calculate the vertical velocity w is discussed in section 2.5.

2.4 Horizontal Tracer Physics

In section 2.2 we have assumed that in the ocean diffusion occurs along horizontal surfaces. Observations, however, show that tracers are more uniformly distributed along surfaces of constant potential density (isopycnals) than along horizontal surfaces (Dutay et al., 2003). This can be illustrated by rewriting the tracer equations in Reynolds averaged isopycnal coordinates (Gent et al., 1995):

$$\begin{aligned} \frac{\partial \overline{T}}{\partial t} + \frac{1}{h_\rho}\frac{\partial}{\partial t}\left(\overline{h'_\rho T'}\right) + \left[\overline{\mathbf{U}}_h + \frac{\overline{h'_\rho \mathbf{U}'_h}}{h_\rho}\right] \cdot \nabla_\rho \overline{T} &= -\nabla_\rho \cdot \left[\overline{(h_\rho \mathbf{U}_h)' T'}\right] / \bar{h}_\rho \\ \frac{\partial \overline{S}}{\partial t} + \frac{1}{h_\rho}\frac{\partial}{\partial t}\left(\overline{h'_\rho S'}\right) + \left[\overline{\mathbf{U}}_h + \frac{\overline{h'_\rho \mathbf{U}'_h}}{h_\rho}\right] \cdot \nabla_\rho \overline{S} &= -\nabla_\rho \cdot \left[\overline{(h_\rho \mathbf{U}_h)' S'}\right] / \bar{h}_\rho \end{aligned} \tag{2.11}$$

where $\mathbf{U}_h = (u, v)$ is the horizontal velocity vector, $h_\rho(x, y, \rho, t) = \bar{h}_\rho + h'_\rho$ is the physical height of a density surface, and ∇_ρ is the horizontal gradient operator applied at constant ρ. Gent et al. (2005) further assume that the second term of Eq. 2.11 is negligible since eddy components of thickness and tracer are uncorrelated, and further assume that the term on RHS follows Fickian diffusion since eddies mix tracers along isopycnals rather than along diapycnals. Hence Eq 2.11 becomes

$$\begin{aligned} \frac{\partial \overline{T}}{\partial t} + \left[\overline{\mathbf{U}}_h + \frac{\overline{h'_\rho \mathbf{U}'_h}}{h_\rho}\right] \cdot \nabla_\rho \overline{T} &= \nabla_\rho \cdot \left[K_h \bar{h}_\rho \nabla_\rho \bar{S}\right] / \bar{h}_\rho \\ \frac{\partial \overline{S}}{\partial t} + \left[\overline{\mathbf{U}}_h + \frac{\overline{h'_\rho \mathbf{U}'_h}}{h_\rho}\right] \cdot \nabla_\rho \overline{S} &= \nabla_\rho \cdot \left[K_h \bar{h}_\rho \nabla_\rho \bar{S}\right] / \bar{h}_\rho \end{aligned} \tag{2.12}$$

In z-coordinate the above equations (without the over bar) are written as

$$\begin{aligned}
\frac{\partial T}{\partial t} + (u+u^*)\frac{\partial T}{\partial x} + (v+v^*)\frac{\partial T}{\partial y} + (w+w^*)\frac{\partial T}{\partial z} &= \mathrm{D}\left(K_h, T\right) \\
\frac{\partial S}{\partial t} + (u+u^*)\frac{\partial S}{\partial x} + (v+v^*)\frac{\partial S}{\partial y} + (w+w^*)\frac{\partial S}{\partial z} &= \mathrm{D}\left(K_h, S\right)
\end{aligned} \tag{2.13}$$

where $\mathrm{D}\left(K_h, T\right)$ is the along isopycnal diffusion term expressed as

$$\mathrm{D}\left(K_h, T\right) = \nabla \cdot \left[K_h B \nabla T\right]$$

$$B = \begin{vmatrix} I & L \\ L & L \cdot L \end{vmatrix}$$

$$L = \frac{\nabla \rho}{\frac{\partial \rho}{\partial z}}$$

where I is a 2×2 identity matrix, and $\nabla = (\frac{\partial}{\partial x}, \frac{\partial}{\partial y}, \frac{\partial}{\partial z})$. Similarly $\mathrm{D}\left(K_h, S\right)$ is obtained by replacing T with S in the above expression.

Gent and McWilliams (1990) proposed the following parameterization (known as Gent and McWilliams parameterization) for the u^*, v^*, w^* terms:

$$\begin{aligned}
u^* &= -\frac{\partial}{\partial z}\left(\kappa L\right) = -\frac{\partial}{\partial z}\left(\kappa \frac{\partial \rho}{\partial x} / \frac{\partial \rho}{\partial z}\right) \\
v^* &= -\frac{\partial}{\partial z}\left(\kappa L\right) = -\frac{\partial}{\partial z}\left(\kappa \frac{\partial \rho}{\partial y} / \frac{\partial \rho}{\partial z}\right) \\
w^* &= \nabla \cdot \left(\kappa L\right)
\end{aligned} \tag{2.14}$$

based on the mechanism of nearly downgradient Fickian diffusion in isopycnal coordinates. The eddy induced diffusivity coefficient κ is normally taken as a constant in most ocean models. Recently, Visbeck et al. (1997) based on the theory of baroclinic instability (Charney, 1947; Eady, 1949; Green, 1970: see Appendix 2.3) showed that it is more appropriate to use a spatially and temporally varying κ :

$$\kappa = \alpha T^{-1} L^2 \tag{2.15}$$

where $\alpha = 0.015$ (obtained from numerical experiment), L is the length scale of baroclinic region, and T^{-1} is the Eady growth rate of unstable baroclinic waves given by:

$$T^{-1} = \frac{f}{\sqrt{Ri}}$$

in which f is the Coriolis parameter and Ri is the Richardson number given as

$$Ri = \frac{(-g/\rho_o)\, d\rho/dz}{\left(\frac{du}{dz}\right)^2 + \left(\frac{dv}{dz}\right)^2}$$

Visbeck et al. (1997) and Deacu and Myers (2005) have implemented the Gent and McWilliams parameterization with variable κ in ocean models, showing improved results. The algorithm for calculating κ is outlined in Appendix 2.4.

2.5 Vertical Physics

The surface mixed layer is an important component of an ocean model due to its role in air-sea exchange processes and mixing. Vertical mixing in the ocean is very inhomogenous and variable: large during convection events, highly variable near the upper and lower boundaries and at steep lateral boundaries, and relatively weak in the interior (Haidvogel and Beckmann, 1999). Hence we require advanced parameterizations of the turbulent fluxes to represent the processes in this layer. The simple idea of constant eddy viscosity (A_v) or diffusivity (K_v) is not the best way to approach the problem of relating the Reynolds stresses/fluxes to the mean motion: we need higher order closure schemes. Some of the widely used schemes for vertical parameterizations in ocean models are: k-profile parameterization (KPP; Large et al., 1994), Kraus-Turner (KT; 1967), Mellor-Yamada (MY; Mellor and Yamada, 1982), and 1.5 turbulent closure scheme (1.5TC Gaspar et al., 1990).

K-profile parameterization (KPP; Large et al., 1994) is a first order parameterization used in a number of ocean models. It provides mixing from surface to bottom, smoothly matching the large surface boundary layer diffusivity/viscosity profiles to

the weak diapycnal diffusivity/viscosity profiles of the interior ocean. The reason why KPP is widely used in ocean models is that it parametrizes the influence of a larger suite of physical processes than other commonly used mixing schemes. In the surface boundary layer, the influence of wind-driven mixing, surface buoyancy fluxes, and convective instability are parameterized. The simple Fickian diffusion with an additional nonlocal term is used to parameterize the surface boundary layer. In the ocean interior, the contribution of background internal wave breaking, shear instability mixing, and double diffusion (both salt fingering and diffusive instability) are parameterized.

The Kraus-Turner mixed layer model is a simpler model that utilizes the turbulent kinetic energy (TKE, described in detail later) equation, converted into a diagnostic equation by setting the time-dependent term to zero i.e. assuming a balance between sources and sinks terms in the water column. The KT model only governs mixing within the surface mixed layer, requiring the user to use other mixing schemes in conjunction for interior diapycnal mixing. The other most widely scheme also based on TKE are the Mellor-Yamada mixed layer model and 1.5TC. They include a TKE prognostic equation and a length scale related parameter which are used to calculate vertical viscosities and diffusivities (Burchard et al., 1998). Since the basis for higher order schemes (MY, KT and 1.5TC) is the turbulent kinetic energy (TKE) equation, the TKE is described next, with emphasis on 1.5TC which is used in NEMO. A discussion on convection parameterizations and vertical velocity calculation are outlined in later sections.

2.5.1 Turbulent kinetic energy (TKE) equation

With the following definition for the average turbulent kinetic energy ($\overline{e}$) :

$$\overline{e} = \left(\overline{u'^2} + \overline{v'^2} + \overline{w'^2}\right)$$

we can obtain a prognostic equation for $\overline{e}$ by first subtracting the mean momentum equations (Eq. 2.9) from the total momentum equations (section 2.1) to yield the fluctuating component of the momentum equations. Then each component of the fluctuating momentum equations are multiplied by u', v', w' respectively and then averaged and added, resulting in (Holton, 1982; Madec, 1998; Pielke, 1984):

$$\frac{\partial \bar{e}}{\partial t} + \bar{u}\frac{\partial \bar{e}}{\partial x} + \bar{v}\frac{\partial \bar{e}}{\partial y} + \bar{w}\frac{\partial \bar{e}}{\partial z} = -\left(\overline{u'w'}\frac{\partial \bar{u}}{\partial z} + \overline{v'w'}\frac{\partial \bar{v}}{\partial z}\right) - g\frac{\overline{\rho' w'}}{\rho_0} - \frac{\partial}{\partial z}\left(\overline{w'e} + \frac{\overline{p'w'}}{\rho_0}\right) - \epsilon \quad (2.16)$$

This equation is usually referred to as the turbulent kinetic energy equation. In the context of a numerical model, Eq. 2.16 is the grid volume averaged, subgridscale kinetic energy equation. The left hand side (LHS) of Eq. 2.16 shows the usual local grid volume change of averaged subgridscale kinetic energy term $\frac{\partial \bar{e}}{\partial t}$ while the other terms are the advection by the "resolved" velocities. On the right hand side (RHS) there are four terms and these terms in order are defined as follows:

(i) Term 1 is known as the mechanical production term or the shear production of TKE arising from the interaction of subgridscale velocity fluxes and average vertical velocity shear. In the NEMO model this term is parameterized as (Madec, 1998):

$$\overline{u'w'}\frac{\partial \bar{u}}{\partial z} + \overline{v'w'}\frac{\partial \bar{v}}{\partial z} = -A_v\left(\left(\frac{\partial \bar{u}}{\partial z}\right)^2 + \left(\frac{\partial \bar{v}}{\partial z}\right)^2\right)$$

where $A_v = C_k l_k \sqrt{\bar{e}}$, and $l_k = \sqrt{2\bar{e}}/N$ is the mixing turbulent length scale obtained in a stable stratified region and is a simplification of the turbulent length scale proposed by Gaspar et al. (1990). Further assumption utilizes that $\mid \frac{\partial l}{\partial z} \mid \leq 1$, such that the vertical variation of the length scale cannot be larger than the variations of depth. The constant $C_k = 0.1$ is designed to deal with vertical mixing at any depth (Gaspar et al., 1990).

(ii) Term 2 is the buoyant production or loss term where there is extraction or

production of $\bar{e}$ by buoyancy. In the NEMO model this is parameterized as (Madec, 1998):

$$\frac{g}{\rho_0}\left(\overline{\rho' w'}\right) = \frac{g}{\rho_0}\left(-K_v \frac{\partial \bar{\rho}}{\partial z}\right) = -K_v N^2 = -\left(\frac{A_v}{P_{rt}}\right) N^2$$

where P_{rt} is the Prandtl number which is function of the local Richardson number: $P_{rt} = 1$ for $Ri \leq 0.2$ and $P_{rt} = 10$ for $Ri \geq 2$, with a linear transition in between. $N^2 = -\frac{g}{\rho_0}\frac{\partial \bar{\rho}}{\partial z}$ is the Brunt Vaisala frequency.

(iii) Term 3 is the redistribution of $\bar{e}$ by turbulent transport and turbulent pressure forces. In the NEMO model this is parameterized as (Madec, 1998):

$$\frac{\partial}{\partial z}\left(\overline{w' e} + \frac{\overline{p' w'}}{\rho_0}\right) = -\frac{\partial}{\partial z}\left(A_v \frac{\partial \bar{e}}{\partial z}\right)$$

(iv) Term 4 is viscous (frictional) dissipation to heat, and is always positive to reflect the action on the smallest scales of turbulence by molecular viscosity (Holton, 1982). In the NEMO model this is parameterized as (Madec, 1998):

$$\epsilon = C_\epsilon \frac{\bar{e}^{1.5}}{l_\epsilon}$$

where $l_e = l_k = \sqrt{2\bar{e}}/N$ is the dissipation turbulent length scale. The constant $C_e = 0.7$ is designed to deal with vertical mixing at any depth (Gaspar et al., 1990).

For boundary conditions in solving TKE equation, at the surface of the sea $\bar{e}$ is prescribed in NEMO from the wind stress field (Madec, 1998): $\bar{e} = 3.75 \mid \tau \mid /\rho_0$, $\mid \tau \mid$ is obtained from the zonal and meridional wind stress vectors. At the bottom of the ocean, $\bar{e}$ is assumed to be equal to the value of the level just above (flux boundary condition: a vanishing vertical gradient in $\bar{e}$ implies a vanishing vertical flux of $\bar{e}$). A cutoff in the minimum value of $\bar{e}$ is set to $\sqrt{2}/2\,10^{-6}\,\mathrm{m^2 s^{-2}}$ (Gaspar et al., 1990; Madec, 1998). In addition the cutoff is applied such that $A_v > 10^{-4}\,\mathrm{m^2 s^{-1}}$ and $K_v > 10^{-5}\,\mathrm{m^2 s^{-1}}$ in order to avoid numerical instabilities associated with too

weak vertical diffusion.

2.5.2 Convection

The hydrostatic assumption made during scaling of the vertical momentum equation (Eq. 2.11) has eliminated convective processes from the surface layer. One feature of convection is static instability occurring especially in high latitudes as a result of heat loss to the atmosphere in the Labrador Sea and the Greenland-Iceland-Norwegian (GIN) Seas (Haidvogel and Beckmann, 2000). Another lesser known cause is brine rejection arising from sea ice growth in polar regions, outside of polar regions instability is evident in upwelling regions along ocean boundaries and in fronts. From a numerical point of view, convection parameterization is one of the most important issues in modeling the surface mixed layer (Haidvogel and Beckmann, 1989).

In the NEMO model the 1.5 turbulent closure scheme described in section 2.5.1 deals with statically unstable profiles. In statically unstable conditions the second term of TKE equation becomes a source term since N^2 is negative ($\frac{\partial \bar{\rho}}{\partial z} < 0$). As a result both vertical mixing coefficients (K_v and A_v) increase, restoring the static stability of the water column through enhanced vertical mixing. In the SPOM model a simple scheme known as convective adjustment (Rahmstorf, 1993) is utilized. In this scheme static instability is removed in the water column at each time step by mixing vertically adjacent grid cells. This simple scheme has proven to be a satisfactory parameterization for many applications.

2.5.3 Vertical velocity

The vertical velocity w in the NEMO and SPOM models is obtained by integrating the continuity equation

$$w = -\int_0^z \left(\frac{\partial u}{\partial x} + \frac{\partial v}{\partial y}\right) dz = -\int_0^z \nabla_h \cdot U_h dz$$

For boundary conditions on w in the NEMO model we have a rigid lid approximation ($w = 0$ at $z = 0$ at the ocean surface) while at the bottom there is also no mass flux ($w = 0$ at $z = b$ where b is ocean depth). If we had not assumed Boussinesq approximation the above calculation would have been a function of density (ρ) too. Further, in nonhydrostatic models w is obtained directly from the vertical momentum equation.

2.6 Boundary and initial conditions

In order to solve the primitive equations, we also need to specify the spatial boundary conditions of all the variables (u, v, w, p, ρ, T, S, A_h, A_v, K_h, K_v, $\bar{e}$), together with their initial conditions. The boundary conditions for w and $\bar{e}$ have been already described while the horizontal momentum, heat and salt fluxes are described next.

2.6.1 Momentum Fluxes

The surface boundary condition on momentum is given by the stress exerted by the surface wind:

$$A_v \frac{\partial}{\partial z}(u, v) \mid_{z=0} = \frac{1}{\rho_0}(\tau_x, \tau_y) \tag{2.17}$$

where (τ_x, τ_y) are the two components of the wind stress vector in the (x, y) coordinate system. SPOM is forced by monthly wind stress derived from the European Centre for Medium Range Weather Forecasts (ECMWF) analysis (Trenberth et al., 1990) averaged over the period 1980-1986, whereas NEMO utilizes the 6 hourly wind forcings of Common Ocean-ice Reference Experiments (CORE) data (Large and Yeager, 2004).

As in the surface momentum flux (wind stress), the bottom momentum flux (bottom friction) also enters the equations as a condition on the vertical diffusive flux:

$$A_v \frac{\partial}{\partial z}(u,v) \mid_{z=b} = (F_x, F_y) \tag{2.18}$$

where (F_x, F_y) in NEMO are given as nonlinear bottom friction parameterization terms:

$$F_x = C_D u_b \sqrt{u_b^2 + v_b^2 + e_b} \tag{2.19}$$

$$F_y = C_D v_b \sqrt{u_b^2 + v_b^2 + e_b} \tag{2.20}$$

in which (u_b, v_b) are the zonal and meridional components of current velocity at the bottom ocean layer, C_D is the drag coefficient ($C_D = 10^{-3}$ in NEMO), e_b is the bottom TKE due to tides, internal waves breaking and other short time scale currents ($e_b = 2.5 \times 10^{-3}$ in NEMO).

Further, in NEMO and SPOM the condition of no normal flow through all solid boundaries (the coasts and the bottom) is applied:

$$(u,v).n = 0$$

where n is a vector of unit length normal to the boundary (Neumann boundary condition).

2.6.2 Heat and Freshwater fluxes

At the surface the heat and freshwater fluxes are prescribed as boundary conditions on the vertical turbulent fluxes on T and S :

$$K_v \frac{\partial T}{\partial z} \mid_{z=0} = \frac{Q}{\rho_0 C_p}$$

$$K_v \frac{\partial S}{\partial z} |_{z=0} = E - P - R$$

where Q is the net surface heat flux, $C_p = 4.10 \times 10^{-3}\,\mathrm{J\,kg^{-1}{}^{\circ}K^{-1}}$ is specific heat capacity of water, E is evaporation, P is precipitation, and R is river runoff. NEMO utilizes the CORE daily heat and freshwater fluxes. However, for simplicity SPOM does not utilize the above flux boundary conditions: it relaxes the surface temperature and salinity to monthly climatological data taken from NODC (1994).

For T and S initial conditions, SPOM utilizes NODC (1994) dataset, whereas NEMO utilizes the Levitus 98-PHC2.1 and Medatlas climatology.

2.6.3 Lateral boundary conditions

Both SPOM and NEMO models are regional models. SPOM extends from 38°N to 70°N, whereas NEMO extends from 20°S to 80°N. In both models the northern and southern limits of the domain are not bounded by solid (land) boundaries. Hence we need to represent the boundary conditions of the variables at these limits so that information could be exchanged with the rest of the ocean. There are normally two types of boundaries that could be used to represent the northern and southern limits: open and closed boundaries.

The southern boundary is open in SPOM while the other boundaries are closed. In NEMO, all the boundaries are closed. For the open boundary condition in SPOM, the tangential velocities are calculated using the momentum equations along the boundary. However, for velocities normal to the domain boundaries, adjustments are made to the tracer equation with a correcting wave speed (Myers, 2002) before calculating the velocities. Myers (2002) shows further that the climatological data used for restoring along the southern boundary do have a significant impact on the model interior solutions such as the Gulf Stream transport, and water masses (eg. Mediterranean

Water and Antarctic Bottom Water). In SPOM, at closed boundaries T and S are restored to NODC (1994) data over the 10 grid boxes nearest the boundary on a 1-day timescale (Myers, 2002). Further, at the northern boundary regions such as Hudson Bay, northern Baffin Bay water properties are restored to observed values in order to accurately represent these important hydrographic regions (Myers, 2002). An examination of the effect of these restoring buffer zones (Myers, 2002) shows improved penetration of West Greenland current (WGC) into Davis Strait, with further effects on temperature and salinity properties being felt all the way down the Labrador coast. The presence of buffer zones in the Nordic Seas also showed improved deep water formations in this region.

2.7 Numerical Methods

Finite differencing method based on centered second order finite difference approximation (for spatial discretization) is used to solve all the equations described in this thesis. Using this scheme, a variable say a at a grid point i is given as:

$$a_i = \frac{1}{2}\left(a_{i+1/2} + a_{i-1/2}\right)$$

The time differencing scheme used is the leapfrog scheme:

$$a^t = \frac{1}{2\triangle t}\left(a^{t+\triangle t} - a^{t-\triangle t}\right)$$

for non-diffusive terms. For diffusive terms the leapfrog scheme is unsuitable and a forward/backward time differencing scheme is used.

In the NEMO model the variables are solved on the C-grid while in the SPOM model the B grid is utilised (Arakawa, 1966; Fig. 2.1).

The approximations of the differential equations for modeling using the finite dif-

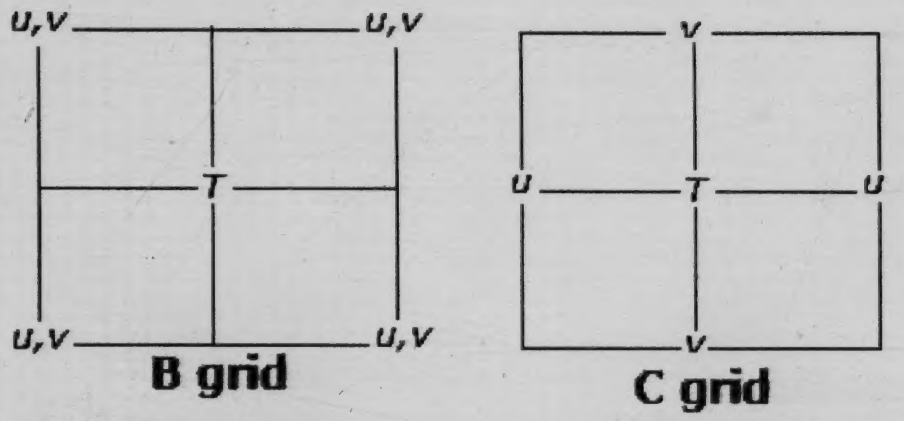

Figure 2.1: The Arakawa B and C grids (Arakawa, 1966) that are used for spatial representation of u, v velocity vectors and T (temperature and salinity) tracers in SPOM and NEMO models respectively.

ference schemes lead to truncation error: error due to the difference between the approximated discretized (difference) form and the full undescretized differential forms arising from approximating an infinite process with a finite numerical process. This error is a potential source of salinity drift. Its effect on basin scale modeling could be tested by running a model with different grid resolutions as described in Haidvogel and Beckmann (1999). The impact of this error on salinity drift is beyond the aim of this thesis.

2.8 Semi Diagnostic Scheme

In order to assimilate observational data, the semi-diagnostic approach (Zhai et al., 2004) is used in this study. This can compensate for erroneous or missing model physics. The method makes adjustments by replacing the density field in the hydrostatic equation by a linear combination of model computed (ρ_m) and climatological density (ρ_c) :

$$\frac{\partial p}{\partial z} = -g\rho_m - g\overline{(\rho_c - \rho_m)} \tag{2.21}$$

The second term on RHS of Eq. 2.21 is a new term in the hydrostatic equation and is filtered spatially. High resolution 3D temperature and salinity climatological data for the Labrador Sea (Kulan and Myers, 2006) merged with the annual Levitus (1982) climatology is used for climatological density (ρ_c) in this study.

Scale analysis of the error term $\overline{(\rho_c - \rho_m)}$ shows it to be of the order of $10^{-1} - 10^{0}$ (further details are given in Chapter 3). Hence it is comparable to the vertical pressure gradient and buoyancy terms which are of the order 10^{1}, and much greater than the rest of the terms in the vertical momentum equation as discussed in section 2.3. Thus the insertion of the second term on RHS does not violate the scale analysis of the vertical momentum equation. Further derivations showing that the hydrostatic assumption holds in the semidiagnostic method are outlined in Sheng et al. (2001).

2.9 North Atlantic ocean models and configurations

In order to model the North Atlantic with the primitive equations described earlier we have a number of models to choose from. A review of the major incompressible, Boussinesq, hydrostatic models in the North Atlantic is presented in this section concluding with a detailed review of the SPOM and NEMO models used in this study. The traditional approach of classifying the ocean models based on their vertical coordinates is also used to categorize ocean models in this section. The choice of vertical coordinate serves as the single most important aspect of an ocean model's design (Griffies et al. 2000). There are three choices for vertical coordinates: geopotential, isopycnal and sigma. Some models have recently started using a combination of all these (hybrid models). Thus it can be said that there are three to four categories of ocean models (not mentioning unstructured grid models).

The differences in the choice of the vertical grid arise through the need to represent processes occurring in the ocean that could be crudely divided into three regimes: in-

terior, bottom boundary layer and surface mixed layer. In the interior of the ocean the tracer transport occurs mainly along isopycnal surfaces, hence the need for isopycnal coordinates for this region. In the bottom boundary layer the topography acts as a strong forcing on the overlying currents. Therefore, topography following sigma coordinates are more convenient in this region. The surface mixed layer where most of the mixing occurs, can be represented by the geopotential, z or height coordinate model which form the basis for today's most widely used numerical ocean models. However, in order to represent all these three different regimes of the ocean accurately, a coordinate system which uses all the three different coordinates (hybrid model) would be the best. Due to computational cost, however, hybrid models are not widely used.

For the North Atlantic the main geopotential models that are in use are MOM (Modular Ocean Model), NEMO (Nucleus for European Modeling of the Ocean) and POP (Parallel Ocean Program). Since MOM, NEMO and POP are based on the same vertical coordinate type they can be also termed as configurations of the geopotential model. However, they are normally known as "models" rather than "configurations" by the scientific community due to their associations with different modeling groups. The main isopycnal, sigma and hybrid models are MICOM (Miami Isopycnal Model), POM (Princeton Ocean Model), and HYCOM (Hybrid Coordinate Ocean Model) respectively. From each of these models a number of configurations at basin scale (North Atlantic, Atlantic) or global scale can be built depending on scientific needs. A configuration can be built basically by differing horizontal and vertical grid resolutions, other numerical details and ocean physics.

2.9.1 Geopotential Models

The first type of ocean model developed was the z-level model (Bryan, 1969; at Geophysical Fluid Dynamics Laboratory in Princeton, USA) in which the vertical discretization was based on constant geopotential surfaces. Further model develop-

ments took place upto 1989 to consider adaptivity with evolving computer architecture (known as the Bryan-Semtner type model). The model was rewritten by Pacanowski et al. (1991) using ideas of modular programming. This development became known as MOM1. MOM2 Version 1 was released in 1995. MOM3 version took place in 1996-1999. Currently MOM4 is under development. A number of configurations of MOM exist eg. SPOM (Sub-polar ocean model; Myers, 2002).

Another geopotential model is NEMO. The NEMO modeling system has built a hierarchy of configurations. Its ocean component is called OPA and is coupled to a multi-layer sea ice code LIM. NEMO's ocean component has the option to switch between geopotential and sigma coordinates. ORCA is the generic name given to global ocean configurations of OPA/NEMO. Standard configurations of OPA/NEMO include ORCA2 LIM which is a coupled ocean/sea ice model at 2^o resolution based on climatological forcing, and GYRE which is an idealized double gyre configuration on a beta plane at 1^o horizontal resolution with analytical forcing. Other configurations include: coarse resolution $1/2^o$ (ORCA05) and $1/4^o$ eddy permitting configuration (ORCA025). $1/4^o$ eddy permitting configuration also exists for Atlantic Basin (ATL4) and North Atlantic/Nordic Seas (NATL4) for regional studies. An eddy resolving configuration (between $1/15^o$ and $1/20^o$) of North Atlantic/Nordic Seas (NATL15) also exists.

POP, another geopotential model, is derived from earlier models of Bryan, Cox, Semtner and Chervin. POP is the ocean component of the Community Climate System Model and has been used extensively at the Los Alamos National Laboratory (in USA) in ocean only mode for eddy-resolving simulations of the global ocean and also for ice-ocean coupled simulations. As in NEMO, POP allows the displacement of meridians converging in the North Pole to adjacent landmass. A 0.1^o global configuration exists for this model in addition to configurations with even higher resolutions of the North Atlantic.

2.9.2 Sigma Models

The terrain following or sigma coordinate offers the advantage of avoiding spurious effects associated with discontinuous representation of bathymetry and sidewall geometry. POM is a sigma coordinate, free surface, ocean model which includes a turbulence sub-model. It was developed by Blumberg and Mellor (1987), with subsequent contributions from other people. The model has been used for modeling of estuaries, coastal regions, basin and global oceans. A number of configurations exist especially for US coast eg. Southeast Atlantic Coastal Forecast System (SEACOOS), and US East Coast Ocean Forecast System. A configuration of POM is also used for ice-ocean forecast by Bedford Institute of Oceanography for the East Coast of Canada.

2.9.3 Isopycnic Models

The isopycnic model has an adaptive vertical grid that is time dependent and thus can adapt to the dynamic situation of the ocean. By suppressing vertical transport terms, and evaluating the horizontal transports along isopycnals, isopycnic coordinate models avoid inconsistencies between vertical and horizontal transport terms that cause false diapycnal mixing.

MICOM (of Rosenstiel School of Marine and Atmospheric Science, University of Miami) is the first isopycnic ocean model used for over 20 years in a number of process studies including the North Atlantic. It has a number of configurations. MICOM near global configuration has horizontal domain 65°N to 69°S, with vertical resolution having 15 sigma-theta layers plus Kraus-Turner (Kraus and Turner, 1967) surface mixed layer. There are 3 additional configurations of resolutions $0.225° \times 0.225°\cos(\text{lat})$, $1.4° \times 1.4°\cos(\text{lat})$, $2.0° \times 0.225°\cos(\text{lat})$. Two additional configurations are 0.9° and 1/3° configurations, and a very high resolution 1/12° (mesh size on the order of 6 km).

2.9.4 Hybrid Models

Traditionally vertical coordinate choices (z-level, sigma, isopycnic) are not by themselves optimal everywhere in the ocean, as pointed out by recent model comparison exercises performed in Europe (DYNAMO) and in the US (DAMEE) (Haidvogel an Beckmann, 1999). Ideally an ocean general circulation model should

(a) retain its water mass characteristics for centuries (isopycnic models),

(b) have high vertical resolution in their vertical mixed layer for proper representation of thermodynamical and biochemical processes (z-level),

(c) maintain sufficient vertical resolution in unstratified and weakly stratified regions of the ocean, and

(d) have high vertical resolution in coastal regions (sigma).

The hybrid coordinate is one that is isopycnal in the open stratified ocean, but smoothly reverts to terrain following coordinate in shallow coastal regions, and to z-level coordinates in the mixed layer and/or unstratified seas. HYCOM (of Rosenstiel school of marine and atmospheric science, University of Miami) is an example of such a model and has the advantage of extending the geographic range of applicability of traditional isopycnal models eg. MICOM. The Office of Naval Research has a $1/12^{o}$ Atlantic HYCOM configuration that includes a nowcast/forecast system.

2.9.5 Model intercomparison

A comparison of all the models mentioned above is summarized in Tables 2.4-2.7.

	Author/Institution	Configurations	Model Equations
MOM	Geophysical Fluid Dynamics Lab (GFDL) Simmons and Griffies (MOM3)	Several versions including MOM 1, MOM2, MOM3 MOM4 (under development)	Primitive, Boussinesq, hydrostatic, free surface, rigid lid
NEMO (NATL4)	(LODYC) Laboratoire d'Oceanographie DYnamique et de Climatologie (Madec, 1998)	ORCA2 LIM, GYRE, ORCA05, ORCA025, ATL4, NATL4, NATL15	Primitive, Boussinesq, hydrostatic, free surface, rigid lid
SPOM	University of Alberta Myers (2002)	1/3° Subpolar ocean model	Primitive, Boussinesq, hydrostatic, free surface
POP	Los Alamos National Laboratory Smith et al. (1992)	0.1° global, high resolution North Atlantic	Primitive, Boussinesq, hydrostatic, free surface
POM	Blumberg and Mellor (1987)	GOM, NYHOPS, COOS Mostly eastern US coast	Primitive free surface
MICOM	Black and Boudra (1982) Miami/Los Alamos	65°S – 65°N domain 0.225°, 1/12°, 1/3°	Primitive
HYCOM	Black and Boudra (1982) Miami/Los Alamos/COAPS	1/12° Atlantic version	Primitive

Table 2.4: Major models in use in the North Atlantic.

	Vertical Grid	Horizontal grid	Sea ice coupling
MOM	z-coordinate 36 levels Partial bottom cell	B grid (Arakawa,1966)	2 ice + 1 snow layer 5 ice categories
NEMO (NATL4)	z-coordinate 46 levels Partial bottom cell	C grid (Arakawa,1966)	2 ice + 1 snow layer 1 ice category
SPOM	z-coordinate 36 levels Partial bottom cell	B grid (Arakawa,1966)	Not Available
POP	z-coordinate	B grid (Arakawa,1966)	POP coupled to CICE and used at NCAR
POM	sigma	C grid (Arakawa,1966)	ocean ice forecast used by BIO
MICOM	isopycnal (diapycnal mixing is suppressed)	C grid (Arakawa,1966)	simple thermodynamic ice model
HYCOM	hybrid	C grid (Arakawa,1966)	simple thermodynamic ice model

Table 2.5: Major models in use in the North Atlantic and their grid specifications.

Tracer Mixing	Horizontal	Vertical	Gent & McWilliams
MOM	Isopycnal diffusion $K_h = 800\,\mathrm{m^2 s^{-1}}$	KPP (Large et al., 1994) ($K_v = 5 \times 10^{-6} - 10^{-4}\mathrm{m^2 s^{-1}}$)	Available
NEMO	Isopycnal diffusion $K_h = 2000\,\mathrm{m^2 s^{-1}}$	1.5 TKE scheme	Available
SPOM	Biharmonic diffusion $K_h = 7.5 \times 10^{14}\mathrm{m^2 s^{-1}}$	Constant vertical diffusivity coefficient $K_v = 3 \times 10^{-5}\mathrm{m^2 s^{-1}}$	Available
POP	Biharmonic diffusion	KPP (Large et al., 1994), Constant vertical diffusivity coefficient $K_v = 3 \times 10^{-5}\mathrm{m^2 s^{-1}}$	Available
POM	Biharmonic diffusion	Mellor and Yamada (1982)	Available
MICOM	Biharmonic diffusion	KPP (Large et al., 1994), 1.5 turbulent closure	Available
HYCOM	Biharmonic diffusion	KPP, 1.5 turbulent closure, Mellor and Yamada (1982)	Available

Table 2.6: Tracer mixing schemes of major models in use in the North Atlantic.

Momentum Mixing	Horizontal	Vertical	Convection
MOM	Laplacian, Biharmonic diffusion	KPP (Large et al., 1994),	KPP (Large et al., 1994),
NEMO	Laplacian, Biharmonic diffusion $A_h = 4 \times 10^5 \mathrm{m}^2\mathrm{s}^{-1}$	1.5 TKE scheme	1.5 TKE scheme, convective adjustment
SPOM	Laplacian, Biharmonic diffusion $A_h = 7.5 \times 10^{14} \mathrm{m}^2\mathrm{s}^{-1}$	Constant vertical viscosity coefficient $A_v = 1.5 \times 10^{-4} m^2 s^{-1}$	convective adjustment of Rahmstorf (1991)
POP	Laplacian, Biharmonic diffusion	KPP (Large et al., 1994), Constant vertical viscosity coefficient $A_v = 2.5 \times 10^{-4} m^2 s^{-1}$	KPP (Large et al., 1994)
POM	Laplacian, Biharmonic diffusion	Mellor and Yamada (1982)	Mellor and Yamada (1982)
MICOM	Laplacian, Biharmonic diffusion	KPP (Large et al., 1994), 1.5 TKE scheme	KPP (Large et al., 1994), 1.5 TKE scheme
HYCOM	Laplacian, Biharmonic diffusion	KPP, 1.5 TKE scheme, Mellor and Yamada (1982)	KPP, 1.5 TKE scheme, Mellor and Yamada (1982)

Table 2.7: Momentum mixing schemes of major models in use in the North Atlantic.

All the ocean models described above have been used in a variety of applications ranging from regional to global ocean modeling and ocean forecasting. Although these models use different vertical coordinates, model intercomparison projects (Haidvogel and Beckmann, 1999) show that all the models are able to realistically simulate the North Atlantic circulation with a considerable degree of realism. The different parameterizations used in the ocean models make it quite difficult to attribute model differences to the vertical coordinate.

As far as choice of a model is concerned, there are a number of reasons why SPOM and NEMO models were chosen for this study. The SPOM model is designed for process studies of the subpolar North Atlantic (Myers, 2002). Although it is possible to create configurations from other models having the domain size of SPOM, such a task is scientifically challenging since the creation of a regional configuration depends

on setting up open boundary conditions and model-specific datasets for topography and coastline, initialization, and forcing (ocean surface heat and freshwater fluxes, wind stress). Hence the development of a regional ocean configuration is a separate study on its own as shown in Myers (2002) and was not the aim of this study. Further, although there do exist regional North Atlantic ocean model configurations (eg. Penduff et al., 2000; Penduff et al., 2001; Treguier et al., 2001), these configurations do not fully address the domain of interest in this study. Finally, SPOM has the Gent and McWilliams parameterization with variable eddy diffusivity coefficient (Deacu and Myers, 2005) which we wished to further investigate. Hence, in order to study the combined effect of a semidiagnostic approach with variable eddy diffusivity coefficient, SPOM is an appropriate choice.

The boundary currents in the subpolar gyre (East and West Greenland Currents, and Labrador Current) carry freshwater originating from sea ice in the Arctic. Hence the representation of sea ice is crucial in modeling (Cuny et al., 2005; Ingram and Prinsenberg, 1998; Kwok and Rothrock, 1999). In order to better represent the subpolar processes the SPOM model could be coupled with a sea ice model, or a different model with an ocean-sea ice coupled system could be used. The latter option was chosen due to the complexity of coupling SPOM to an ice model (which is a separate study of its own). Hence the NEMO model was chosen for further studies of the subpolar gyre. In comparison to SPOM, NEMO has better resolution, has a larger domain, has C grid instead of B grid, and has several parameterizations not included in SPOM. Another advantage of utilizing the NEMO model is that the results of this study would be directly transferable for operational use in Canada since NEMO has been recently chosen as the model to be coupled to the atmospheric model of Meteorological Service of Canada for weather forecasting. Further, ocean modelers in Canada and Europe are now switching to NEMO as their primary model for research and operational use.

2.10 Assessment and validation of results

Validation of a model is an important step in modeling and data assimilation studies in order to assess the closeness of the modelled field to observations. Model evaluation through model-data comparison studies is an important prerequisite of any simulation. Two types of validation techniques: qualitative and quantitative (Pielke,1984) can be used to validate ocean models. As far as ocean modeling is concerned, a major difficulty in validation has been a lack of global oceanic data sets of sufficient quality and duration to characterize the error statistics because observational data are relatively more sparse in the global ocean than in the atmosphere (Kara et al., 2005). Due to this, qualitative validation of ocean models is more prevalent than quantitative analysis. The two models used in this study (SPOM and NEMO) have been validated using these approaches.

Validation of the SPOM model shows that it establishes the basic circulation patterns and hydrography (Myers, 2002) after 40 years of integration, with the eddy kinetic energy of the model also achieving a seasonal steady state during this period. A qualitative comparison of model computed annually averaged salinity fields and the Levitus climatology shows that the large scale structure is well represented. Detailed and systematic qualitative comparisons with observations of model computed Labrador Current velocity, volume transports at various regions in the subpolar gyre, water masses and other features such as convection depths are outlined in Myers (2002). The problem of salinity drift is a feature of SPOM model, as in other high resolution subpolar models, leading to a large overall error in multi-year simulations that needs to be corrected: forming one of the main scientific issues of this study.

The validation of the NEMO model is outlined in detail in Barnier et al. (2006). A qualitative description is outlined of the model circulations in terms of its ability to reproduce the sea surface height fields and eddy kinetic energy. A quantitative analysis of the meridional heat transport is also outlined. The NEMO model is used by a num-

ber of research groups. Since 1998 through to the end of 2007 there were 426 journal publications based on the output of this model. A summary of the associated journal publications is outlined at http://www.locean-ipsl.upmc.fr/NEMO/general/biblio_new/en/one/bibnemomain.php

In validation of ocean models (and also in ocean data assimilation) there are basically two types of errors that are of concern. These are data error and model error (Fukumori, 2006). Data error arises from measurement errors such as instrument errors. The model errors arise from "external model" errors such as external forcings, boundary conditions, and model parameters used by the model; and "internal model" errors arise from finite differencing, truncation, scaling, approximations, and interactions with scales and processes (subgridscale) ignored by the model. This thesis discusses issues that arise from errors due to "internal model" errors, specifically those arising from "interaction with scales and processes ignored by the model" leading to the large salinity drift. The model errors are larger than data errors and as a result "observational error bars" are not presented in most of the figures in this thesis. Nevertheless, the relative importance of the two errors is illustrated in a few instances in this thesis (eg. discussion of the freshwater content graph in Chapter 3).

Bibliography

[1] Arakawa, A., 1966. Computational design for long-term numerical integration of the equations of fluid motion: two dimensional incomplete flow: Part 1. Journal of Computational Physics. 1, 119-143.

[2] Barnier, B., Madec, G., Penduff, T., Molines, J.M., Treguier, A.M., Sommer, J.L., Beckmann, A., Biastoch, A., Böning, C., Dengg, J., Derval, C., Durand, E., Gulev, S., Remy, E., Talandier, C., Theetten, S., Maltrud, M., McClean, J., Cuevas, B.D., 2006. Impact of partial steps and momentum advection schemes in a global ocean circulation model at eddy-permitting resolution. Ocean Dynamics, doi 10.1007/s10236-006-0082-1.

[3] Black, R. and Boudra, D.B., 1981. Initial testing of a numerical ocean circulation model using a hybrid (quasi-isopycnic) vertical coordinate. Journal of Physical Oceanography. 23, 1363-1388.

[4] Blanke, B. and Delecluse, P., 1993. Variability of tropical Atlantic ocean simulated by a general circulation model with two different mixed-layer physics. Journal of Physical Oceanography. 11, 755-770.

[5] Blumberg, A.F. and Mellor, G.L., 1987. A description of a three dimensional coastal ocean circulation model, three dimensional coastal ocean models, edited by N. Heaps, 208 pp, American Geophysical Union.

[6] Bougeault, P., and Lacarrere, P., 1989. Parameterization of orography-induced turbulence in a mesobeta-scale model. Mon. Wea. Rev., 117, 1872-1890.

[7] Bryan, K. 1969. A numerical method for the study of the circulation of the world ocean. Jour. Computational Physics, 4 no. 3 , 347–376.

[8] Charney, J.G., 1947. The dynamics of long waves in a baroclinic westerly current. Journal of Meteorology, 4: 135-163.

[9] Detlef, S., 1997. On eddy characteristics, eddy transports, and mean flow properties, Journal of Physical Oceanography. 28, 727-739.

[10] Dutay, J.C., Jean-Baptise, P., Campin, J.M., Ishida, A., Maier-Reiner, E., Matear, R.J., Mouchet, A., Totterdell, I.J., Yamanaka, Y., Rodgers, K., Madec, G., Orr, J.C., 2004. Evaluation of OCMIP-2 ocean models' deep circulation with mantle helium-3. Journal of Marine Systems, 48, 15-36.

[11] Eady, E.T. 1949. Long waves and cyclone waves. Tellus 1 (3), 33-52.

[12] Fukumori, I., 2006. What is data assimilation really solving, and how is the calculation actually done? edited by Chassignet and Verron.

[13] Gaspar P., Gregoris, Y., and Lefevre, J.M., 1990. A simple eddy-kinetic-energy model for simulations of the ocean vertical mixing: tests at station Papa and Long-term Upper Ocean Study Site. J. Geophysical Research, 95, 16179-16193.

[14] Gent, P.R., McWilliams, J.C., 1990. Isopycnal mixing in ocean circulation models. Journal of Physical Oceanography 20, 150-155.

[15] Gent, P.R., Willebrand, J., McDougall, T., McWilliams, J.C., 1995. Parameterizing eddy-induced tracer transports in ocean circulation models. Journal of Physical Oceanography 25, 463-474.

[16] Greatbatch, R.J., 1994. A note on the representation of steric sea level in models that conserve volume rather than mass. Journal of geophysical research, 99: 12767-12771.

[17] Green, J. S. A., 1970. Transfer properties of the large scale eddies and the general circulation of the atmosphere. Quarterly Journal of the Royal Meteorological Society: 96, 157-185.

[18] Griffies, S.M., Boning, C., Bryan, F.O., Chassignet, E.P., Gerdes, R., Hasumi, H., Hirst, A., Treguier, A., Webb, D., 2000. Developments in ocean climate modelling. Ocean Modelling, 2, 123-192.

[19] Haidvogel, D.B., Beckmann, A., 1999. Numerical ocean circulation modeling, Series on environmental science and management: vol 2.

[20] Holton, J.R., 1992. An introduction to dynamic meteorology, third edition, International geophysics series vol 48, Academic Press, California, USA.

[21] Hunke, E., Mathew, M., and Matthew, H., 2008. On the grid dependence of lateral mixing parameterizations for global ocean simulations. Ocean Modelling, 20/2, 115-133.

[22] Iskandarani, M., Haidvogel, D.B., and Boyd, J.P., 1995. A staggered spectral element model with applications to the oceanic shallow water equations. Int. J. Num. Meth. Fl., 20:393-414.

[23] Jackett, D.R., and McDougall, T.J., 1995. Minimal adjustment of hydrographic data to achieve static stability. J. Atmos. Ocean Tech., 12, 381-389.

[24] Kantha, L. H., Clayson, C.A., 2000a. Numerical models of oceans and oceanic processes. International geophysics series vol 66, Academic Press, California, USA.

[25] Kantha, L. H., Clayson, C.A., 2000b. Small scale processes in geophysical fluid flows. International geophysics series vol 67, Academic Press, California, USA.

[26] Kara, A.B., Barron, C.N., Martin, P.J., Smedstad, L.F., Rhodes, R.C., 2005. Validation of interannual simulations from the 1/8° global Navy Coastal Ocean Model (NCOM), Ocean Modeling, 11, 376-398.

[27] Kraus, E.B., Turner, J.S., 1967. A one dimensional model of the seasonal thermocline. II. The general theory and its consequences. Tellus, 19, 98-106.

[28] Large, W.G., McWilliams, J.C, Doney S.C., 1994. Oceanic vertical mixing: a review and a model with a nonlocal boundary layer parameterization. Review of Geophysics, 32, 363-403.

[29] Large, W., Yeager, S., 2004. Diurnal to decadal global forcing for ocean and sea-ice models: the data sets and flux climatologies. NCAR technical note: NCAR/TN-460+STR. CGD division of the National Center of Atmospheric Research.

[30] Madec, G., Delecluse, P., Imbard, M., Levy, C.,1998. General circulation model reference manual. Notes de l'IPSL, Universite P. et M. Curie, B102 T15-ES, 4 place Jussie, Paris cedex 5, N°11, 91p.

[31] Marshall, J., Hill C., Perelman, L., Adcroft, A., 1997. Hydrostatic, quasi-hydrostatic, and nonhydrostatic ocean modeling. Journal of geophysical research, 102: 5733-5752.

[32] Mellor, G.L., and Yamada, T., 1982. Development of a turbulent closure model for geophysical fluid problems. Review of Geophysics, 20, 851-875.

[33] Mellor, G.L., Ezer, T., 1995. Sea level variations induced by heating and cooling: an evaluation of the Boussinesq approximation in ocean models. Journal of Geophysical research, 100: 20, 565-20, 577.

[34] Niiler, P.P. and Kraus, E.B., 1977. One-dimensional models. In Modelling and Prediction of the Upper Layers of the Ocean, E.B. Kraus, Editor. Perggamon, New York, 143-172.

[35] NODC, 1994. World ocean atlas 1994 cd-rom data set documentation, Tech. Rep. NOAA, US Department of Commerce.

[36] Pacanowski, Dixon, K., and Rosati. A, 1991. The GFDL modular ocean model user guide. GFDL Ocean Group Tech. Rep. 2, Geophys. Fluid Dyn. Lab, Princeton, NJ.

[37] Penduff, T., Barnier, B., De Verdiere, A.C., 2000. Self adapting open boundaries for a sigma coordinate model of the eastern North Atlantic. J. Geophys. Res. 106: 22313-22329

[38] Penduff, T., De Verdiere, A.C., Barnier, B., 2001. General circulation and intergyre dynamics in the eastern North Atlantic from a regional primitive equation model. J. Geophys. Res. 106: 22313-22329.

[39] Pielke, R.A., 1984. Mesoscale meteorological modeling. Academic Press.

[40] Rahmstorf, S. 1993. A fast and complete convection scheme for ocean models. Ocean Modeling. 101: 9-11.

[41] Smith, R.D., Dukowicz, J.K., Malone, R.C., 1992. Parallel ocean general circualtion modeling. Physica D, 60, 38-61.

[42] Song, Y. and Haidvogel, D.B., 1984. A semi-implicit ocean circulation model using a generalised topography-following coordinate system. J. Comp. Phys., 115(1): 228-244.

[43] Treguier, A.M., Barnier, B., De Miranda, A.P., Molines, J.M., Grima, N., Imbard, M., Madec, G., Messager, C., Reynaud, T., Michel, S., 2001. An eddy permitting model of the Atlantic circulation: Evaluating open boundary conditions. J. Geophys. Res. : 106, 22115-22129.

[44] Trenberth, K.E., Large, W.G., Olson, J.G., 1990. The mean annual cycle in global ocean wind stress. Journal of Physical Oceanography 20, 1742-1760.

[45] UNESCO, 1983. Algorithms for computation of fundamental property of sea water. UNESCO Tech. Paper in Mar. Sci., 44, Unesco, 53pp.

Appendix 2.1 Reynolds decomposition

Let's substitute the decomposed Reynolds terms into the left hand side of the u momentum equation:

$$\frac{\partial(\bar{u}+u')}{\partial t} + (\bar{u}+u')\frac{\partial(\bar{u}+u')}{\partial x} + (\bar{v}+v')\frac{\partial(\bar{u}+u')}{\partial y} + (\bar{w}+w')\frac{\partial(\bar{u}+u')}{\partial z}$$

$$= \frac{\partial\bar{u}}{\partial t}+\frac{\partial u'}{\partial t}+\bar{u}\frac{\partial\bar{u}}{\partial x}+\bar{u}\frac{\partial u'}{\partial x}+u'\frac{\partial\bar{u}}{\partial x}+u'\frac{\partial u'}{\partial x}+\bar{v}\frac{\partial\bar{u}}{\partial y}+\bar{v}\frac{\partial u'}{\partial y}+v'\frac{\partial\bar{u}}{\partial y}+v'\frac{\partial u'}{\partial y}+\bar{w}\frac{\partial\bar{u}}{\partial z}+\bar{w}\frac{\partial u'}{\partial z}+w'\frac{\partial\bar{u}}{\partial z}+w'\frac{\partial u'}{\partial z}$$

A time average of the above equation is:

$$\overline{\frac{\partial\bar{u}}{\partial t}}+\overline{\frac{\partial u'}{\partial t}}+\overline{\bar{u}\frac{\partial\bar{u}}{\partial x}}+\overline{\bar{u}\frac{\partial u'}{\partial x}}+\overline{u'\frac{\partial\bar{u}}{\partial x}}+\overline{u'\frac{\partial u'}{\partial x}}+\overline{\bar{v}\frac{\partial\bar{u}}{\partial y}}+\overline{\bar{v}\frac{\partial u'}{\partial y}}+\overline{v'\frac{\partial\bar{u}}{\partial y}}+\overline{v'\frac{\partial u'}{\partial y}}+\overline{\bar{w}\frac{\partial\bar{u}}{\partial z}}+\overline{\bar{w}\frac{\partial u'}{\partial z}}+\overline{w'\frac{\partial\bar{u}}{\partial z}}+\overline{w'\frac{\partial u'}{\partial z}}$$

Applying the rules given in section 2.2 the above equation reduces to:

$$\frac{\partial\bar{u}}{\partial t}+\bar{u}\frac{\partial\bar{u}}{\partial x}+\bar{v}\frac{\partial\bar{u}}{\partial y}+\bar{w}\frac{\partial\bar{u}}{\partial z}+\overline{u'\frac{\partial u'}{\partial x}}+\overline{v'\frac{\partial u'}{\partial y}}+\overline{w'\frac{\partial u'}{\partial z}}$$

This can be also written in flux form as:

$$\frac{\partial\bar{u}}{\partial t}+\bar{u}\frac{\partial\bar{u}}{\partial x}+\bar{v}\frac{\partial\bar{u}}{\partial y}+\bar{w}\frac{\partial\bar{u}}{\partial z}+\frac{\partial}{\partial x}\overline{u'u'}+\frac{\partial}{\partial y}\overline{v'u'}+\frac{\partial}{\partial z}\overline{w'u'}$$

The terms such as $\overline{u'\frac{\partial u'}{\partial x}}$ has been converted into $\frac{\partial\overline{u'u'}}{\partial x}$ by taking advantage of the continuity equation. Let's subtract the mean continuity equation $(\frac{\partial\bar{u}}{\partial x}+\frac{\partial\bar{v}}{\partial y}+\frac{\partial\bar{w}}{\partial z}=0)$ from its total $(\frac{\partial u}{\partial x}+\frac{\partial v}{\partial y}+\frac{\partial w}{\partial z}=0)$ resulting in $(\frac{\partial u'}{\partial x}+\frac{\partial v'}{\partial y}+\frac{\partial w'}{\partial z}=0)$. Since $u'(\frac{\partial u'}{\partial x}+\frac{\partial v'}{\partial y}+\frac{\partial w'}{\partial z})=0$, it can be added to:

$$u'\frac{\partial u'}{\partial x}+v'\frac{\partial u'}{\partial y}+w'\frac{\partial u'}{\partial z}+u'(\frac{\partial u'}{\partial x}+\frac{\partial v'}{\partial y}+\frac{\partial w'}{\partial z})$$

which can be rewritten using the product rule as

$\frac{\partial}{\partial x}u'u' + \frac{\partial}{\partial y}v'u' + \frac{\partial}{\partial z}w'u'.$

Hence taking time averages of the terms in

$$\overline{u'\frac{\partial u'}{\partial x}} + +\overline{v'\frac{\partial u'}{\partial y}} + \overline{w'\frac{\partial u'}{\partial z}}$$

would yield

$$\frac{\partial}{\partial x}\overline{u'u'} + \frac{\partial}{\partial y}\overline{v'u'} + \frac{\partial}{\partial z}\overline{w'u'}.$$

Similarly, Reynolds averaging can be applied to the rest of the equations in the primitive equation set. Holton (1982), follows a much simpler method of Reynolds averaging of the primitive equations. First, the total derivatives are written in flux form:

$$\frac{Du}{Dt} = \frac{\partial u}{\partial t} + u\frac{\partial u}{\partial x} + v\frac{\partial u}{\partial y} + w\frac{\partial u}{\partial z} + u\left(\frac{\partial u}{\partial x} + \frac{\partial v}{\partial y} + \frac{\partial w}{\partial z}\right) = \frac{\partial u}{\partial t} + \frac{\partial u^2}{\partial x} + \frac{\partial uv}{\partial y} + \frac{\partial uw}{\partial z}$$

and then the terms on the right hand side are expanded using Reynolds averaging to yield:

$$\overline{\frac{Du}{Dt}} = \overline{\frac{\partial u}{\partial t}} + \overline{\frac{\partial u'}{\partial t}} + \overline{\frac{\partial}{\partial x}(\bar{u}+u')(\bar{u}+u')} + \overline{\frac{\partial}{\partial y}(\bar{u}+u')(\bar{v}+v')} + \overline{\frac{\partial}{\partial z}(\bar{u}+u')(\bar{w}+w')}.$$

Taking advantage of the postulates in section 2.2 we can elimate some of the terms with the resulting equation as:

$$\overline{\frac{Du}{Dt}} = \frac{\partial \bar{u}}{\partial t} + \frac{\partial}{\partial x}\left(\bar{u}\bar{u} + \overline{u'u'}\right) + \frac{\partial}{\partial y}\left(\bar{u}v + \overline{u'v'}\right) + \frac{\partial}{\partial z}\left(\bar{u}\bar{w} + \overline{u'w'}\right)$$

Rearranging the terms we get:

$$\overline{\frac{Du}{Dt}} = \left[\frac{\partial \bar{u}}{\partial t} + \frac{\partial}{\partial x}(\bar{u}\bar{u}) + \frac{\partial}{\partial y}(\bar{u}v) + \frac{\partial}{\partial z}(\bar{u}\bar{w})\right] + \left[\frac{\partial}{\partial x}\left(\overline{u'u'}\right) + \frac{\partial}{\partial y}\left(\overline{u'v'}\right) + \frac{\partial}{\partial z}\left(\overline{u'w'}\right)\right]$$

The set of terms in the first bracket could be said as the terms arising from the mean or "resolved" motion $\left(\frac{\bar{D}\bar{u}}{Dt}\right)$ whereas the second set of terms arise from the "unresolved" component. This expression is used to obtain the Reynolds averaged primitive equations:

$$\begin{aligned}\overline{\frac{Du}{Dt}} &= \frac{\bar{D}\bar{u}}{Dt} + \left[\frac{\partial}{\partial x}\left(\overline{u'u'}\right) + \frac{\partial}{\partial y}\left(\overline{u'v'}\right) + \frac{\partial}{\partial z}\left(\overline{u'w'}\right)\right] \\ &= -\frac{1}{\rho_0}\frac{\partial \bar{p}}{\partial x} + f\bar{v}\end{aligned}$$

$$\begin{aligned}\overline{\frac{Dv}{Dt}} &= \frac{\bar{D}\bar{v}}{Dt} + \left[\frac{\partial}{\partial x}\left(\overline{u'v'}\right) + \frac{\partial}{\partial y}\left(\overline{v'v'}\right) + \frac{\partial}{\partial z}\left(\overline{w'v'}\right)\right] \\ &= -\frac{1}{\rho_0}\frac{\partial \bar{p}}{\partial y} - f\ \bar{u}\end{aligned}$$

$$\begin{aligned}\overline{\frac{Dw}{Dt}} &= \frac{\bar{D}\bar{w}}{Dt} + \left[\frac{\partial}{\partial x}\left(\overline{u'w'}\right) + \frac{\partial}{\partial y}\left(\overline{v'w'}\right) + \frac{\partial}{\partial z}\left(\overline{w'w'}\right)\right] \\ &= -\frac{\bar{\rho}}{\rho_o}g - \frac{1}{\rho_o}\frac{\partial \bar{p}}{\partial z}\end{aligned}$$

$$\frac{\partial \bar{u}}{\partial x} + \frac{\partial \bar{v}}{\partial y} + \frac{\partial \bar{w}}{\partial z} = 0$$

$$\overline{\frac{DT}{Dt}} = \frac{\bar{D}\bar{T}}{Dt} + \left[\frac{\partial}{\partial x}\left(\overline{u'T'}\right) + \frac{\partial}{\partial y}\left(\overline{v'T'}\right) + \frac{\partial}{\partial z}\left(\overline{w'T'}\right)\right] = \overline{R^*}$$

$$\overline{\frac{DS}{Dt}} = \frac{\bar{D}\bar{S}}{Dt} + \left[\frac{\partial}{\partial x}\left(\overline{u'S'}\right) + \frac{\partial}{\partial y}\left(\overline{v'S'}\right) + \frac{\partial}{\partial z}\left(\overline{w'S'}\right)\right] = \overline{S^*}$$

It is customary to write the primed terms on the RHS (right hand side). Rewriting the above equations yield:

$$\frac{\bar{D}\bar{u}}{Dt} = -\frac{1}{\rho_0}\frac{\partial \bar{p}}{\partial x} + f\bar{v} - \left[\frac{\partial}{\partial x}\left(\overline{u'u'}\right) + \frac{\partial}{\partial y}\left(\overline{u'v'}\right) + \frac{\partial}{\partial z}\left(\overline{u'w'}\right)\right]$$

$$\frac{\bar{D}\bar{v}}{Dt} = -\frac{1}{\rho_0}\frac{\partial \bar{p}}{\partial y} - f\bar{u} - \left[\frac{\partial}{\partial x}\left(\overline{u'v'}\right) + \frac{\partial}{\partial y}\left(\overline{v'v'}\right) + \frac{\partial}{\partial z}\left(\overline{w'v'}\right)\right]$$

$$\frac{\bar{D}\bar{w}}{Dt} = -\frac{\bar{\rho}}{\rho_o}g - \frac{1}{\rho_o}\frac{\partial \bar{p}}{\partial z} - \left[\frac{\partial}{\partial x}\left(\overline{u'w'}\right) + \frac{\partial}{\partial y}\left(\overline{v'w'}\right) + \frac{\partial}{\partial z}\left(\overline{w'w'}\right)\right]$$

$$\frac{\partial \bar{u}}{\partial x} + \frac{\partial \bar{v}}{\partial y} + \frac{\partial \bar{w}}{\partial z} = 0$$

$$\frac{\bar{D}\bar{T}}{Dt} = -\left[\frac{\partial}{\partial x}\left(\overline{u'T'}\right) + \frac{\partial}{\partial y}\left(\overline{v'T'}\right) + \frac{\partial}{\partial z}\left(\overline{w'T'}\right)\right] + \overline{R^*}$$

$$\frac{\bar{D}\bar{S}}{Dt} = -\left[\frac{\partial}{\partial x}\left(\overline{u'S'}\right) + \frac{\partial}{\partial y}\left(\overline{v'S'}\right) + \frac{\partial}{\partial z}\left(\overline{w'S'}\right)\right] + \overline{S^*}$$

Appendix 2.2 Laws of Diffusion

Fick's First Law of Diffusion is:

$$\vec{J} = -A\left(\frac{\partial\phi}{\partial x}, \frac{\partial\phi}{\partial y}, \frac{\partial\phi}{\partial z}\right) = -A\left[\frac{\partial\phi}{\partial x}\hat{i} + \frac{\partial\phi}{\partial y}\hat{j} + \frac{\partial\phi}{\partial z}\hat{k}\right] = -A\nabla\phi$$

where $\vec{J}$ is diffusion flux, A is diffusion coefficient or diffusivity, ϕ is concentration, for fluid motion in (x, y, z) direction. This is analogous to Fourier's Law of heat conduction

$$\vec{H} = -k\nabla T$$

where $\vec{H}$ is heat flux, k is the thermal conductivity and T is temperature. For a nonsteady state $\frac{\partial\phi}{\partial t} \neq 0$ we use Fick's Second Law of Diffusion:

$$\frac{\partial\phi}{\partial t} = -\left(\frac{\partial}{\partial x}, \frac{\partial}{\partial y}, \frac{\partial}{\partial z}\right) \cdot \left[A\left(\frac{\partial\phi}{\partial x}, \frac{\partial\phi}{\partial y}, \frac{\partial\phi}{\partial z}\right)\right]$$

For constant A :

$$\frac{\partial\phi}{\partial t} = -A\left(\frac{\partial^2\phi}{\partial x^2} + \frac{\partial^2\phi}{\partial y^2} + \frac{\partial^2\phi}{\partial z^2}\right) = -A\nabla^2\phi$$

which is analogous to the heat equation:

$$\frac{\partial T}{\partial t} = -k\nabla^2 T$$

Appendix 2.3 Models of baroclinic instability

(i) **Eady model** (Eady, 1949): is bounded below and above by rigid horizontal lids, without taking account of the β effect (i.e. $\beta = 0$). The growth rate is dependent upon wavenumber and wavespeed (which depends on vertical wind shear, Coriolis parameter and buoyancy frequency). Eady growth rate is given as

$$T^{-1} = \frac{f}{\sqrt{Ri}}$$

where

$$Ri = \frac{N^2}{\left(\frac{\partial u}{\partial z}\right)^2 + \left(\frac{\partial v}{\partial z}\right)^2}$$

The maximum value of growth rate is given as

$T^{-1} = 0.3098 \frac{f}{N} \frac{dU}{dZ}$.

Since $\kappa = \alpha T^{-1} L^2$, the maximum growth rate of an Eady wave is given by

$\kappa = \alpha 0.3098 \frac{f}{N} \frac{dU}{dZ} L^2$.

(ii) **Charney model** (Charney, 1947): includes the β effect (i.e. β is positive). There is no lid: the horizontal and vertical scales are set by the value of β and not, say, by the tropopause height. Qualitatively the Charney solution looks like the Eady solution, but quantitatively there are differences. The maximum growth rate of the Charney wave is similar Eady wave (and is also independent of β) except that the maximum value of growth rate is given as

$T^{-1} = 0.286 \frac{f}{N} \frac{dU}{dZ}$.

Hence the maximum value of κ obtained by the Charney model is about 8% smaller.

(iii) **Green model** (Green, 1970): has both β effect (i.e. β is positive) and lid, hence combines the Eady and Charney models. The maximum growth rates vary little and are similar to Eady and Charney maximum growth rates.

Appendix 2.4 Variable eddy diffusivity (κ) computation

The formulation for κ, derived from baroclinic instability theory (Appendix 2.3) is:

$$\kappa = \alpha T^{-1} L^2 = \alpha \frac{f}{\sqrt{Ri}} L^2$$

where $\alpha = 0.015$ is derived from a comparison of eddy resolving numerical experiments and parameterizations in three different oceanic scenarios producing baroclinic eddies (Visbeck et al., 1997). T^{-1} is the growth rate of an Eady wave (Eady, 1949), and L is the width of the baroclinic zone. κ can be also stated as the product of an eddy velocity scale v and a length scale L :

$$\kappa = \alpha T^{-1} L^2 = \alpha \left(\frac{L}{T}\right) L = \alpha v L$$

The description of the calculation of the variable eddy diffusivity coefficient is outlined below (Deacu and Myers, 2005). The algorithm first calculates the Ri number for each point in the model using:

$$Ri = \frac{(-g/\rho_o)\, d\rho/dz}{\left(\frac{du}{dz}\right)^2 + \left(\frac{dv}{dz}\right)^2}$$

Then the growth rate is calculated at each model grid point between 100-2000 m (in NEMO) using

$$T^{-1} = \frac{f}{\sqrt{Ri}}.$$

A 2D matrix of growth rates is then obtained by averaging the growth rates between the layers 100-2000 m (1900 m). The maximum value of T^{-1} is set to $2.3 \times 10^{-5}\,\mathrm{s}^{-1}$ while the minimum value is set to $1.4 \times 10^{-6}\,\mathrm{s}^{-1}$.

The next step is to calculate the length scale L from the growth rate values. It is calculated in the model by starting with a value set to $L = \max(\Delta x, \Delta y)$. If the growth rate at a grid point is less than $1.4 \times 10^{-6}\,\mathrm{s}^{-1}$ (the growth rate for baroclinic eddies in the subpolar gyre; and is equivalent to a timescale of 8.25 days which is a typical timescale for baroclinic eddies in this region) then the lengthscale remains unchanged. Detlef (1997) shows that the baroclinic time scale changes from about 45 days near the equator to about 1 day in the northern subpolar gyre. Hence the time for baroclinic eddies to grow decreases polewards since their size also decreases polewards. If the time scale in the subpolar gyre is larger than 8.25 days then there is no need to re-calculate the length scale since baroclinic eddies of this size would be resolvable by the grid resolution. However, if the time scale is smaller than 8.25 days then we need to re-calculate the baroclinic lengthscale L. In such a case L would be larger and as a result the value of κ would be large too.

The values of T^{-1} and L thus calculated are inserted in the formula for κ. The maximum allowable value of κ in our model is $1000\,\mathrm{m}^2\mathrm{s}^{-1}$ while the minimum value is $50\,\mathrm{m}^2\mathrm{s}^{-1}$ for model depths of 100-2000 m. For shallow water (depths < 100 m) L is set to $\max(\Delta x, \Delta y)$ and κ is set to $40\,\mathrm{m}^2\mathrm{s}^{-1}$ while over land $L = 0$ and $\kappa = 0$.

Chapter 3

Role of eddies in heat and freshwater transport in the Labrador Sea

3.1 Introduction

The subpolar gyre of the North Atlantic ocean comprises the Labrador Sea which is the site for the formation of Labrador Sea Water that plays a significant role in the upper limb of the global thermohaline circulation (Cuny et al., 2002). Numerous modelling studies have been performed to analyze the circulation in the sub-polar North Atlantic and the Labrador Sea (eg. Eden and Boning, 2002). Some of the modelling studies, however, have not led to simultaneous improvements in circulation and hydrography. For example, improvements in sub-polar circulations were obtained when the ocean bottom topography was improved through partial cell representation (Kase et al., 2001; Myers, 2002) where the bottom-most finite cell in each column was partially filled with topography (Adcroft et al., 1997). However, Myers (2002) found significant increase in the salinity of the Labrador Sea using this approach. A recent comparison of the North Atlantic sub-polar gyre in four high resolution models (Treguier et al., 2005) also showed serious drift in water mass properties, with

a spurious salinization of the Labrador Sea Water.

An analysis of the freshwater budget of the Labrador Sea (Myers and Deacu, 2004) suggested that the reason for the increase in salinity of the Labrador Sea in their model was through an excessive import of high salinity water by the North Atlantic current, and an enhanced export of Labrador Sea Water to the Irminger Sea. This exchange of salt was facilitated by the presence of an overly strong counter-current in the Labrador Sea in the partial cell experiment of Myers and Deacu (2004). An energy analysis showed increased eddy activity led to the enhancing of the counter current. Hence it was suggested that an improved parameterization of the eddy processes could weaken the counter-current and lead to a reduction in the entrainment of saline water into the Labrador Sea.

To achieve this, Deacu and Myers (2005) applied a variable eddy transfer coefficient (Visbeck et at., 1997) for the Gent-McWilliams (GM) parameterization (Gent and McWilliams, 1990). In this scheme (discussed in detail later) the constant eddy transfer coefficient used to simulate eddy-induced tracer transport (Gent and McWilliams, 1990) was replaced by a spatially and temporally varying eddy transfer coefficient. A number of improvements in circulation were noted, and the freshwater content drift (or the entrainment of high salinity by the North Atlantic Current) in their simulations was reduced to some extent. Yet the reduction in the freshwater content drift achieved by Deacu and Myers (2005) is not sufficient and further improvements are still required.

Another potential approach to correct an ocean model is through ocean data assimilation. The use of observed data could alleviate the limitations on the processes that could be represented by the model physics. One scheme that is simple to implement is the semi-diagnostic method (Zhai et al., 2004), which is a variant of the semi-prognostic method of Sheng et al. (2001). This method utilizes the climatological temperature and salinity fields to adjust the momentum balance of the model,

while leaving the tracer equations fully prognostic and unconstrained.

The semi-diagnostic approach is also an eddy diagnosing tool (Greatbatch and Zhai, 2006; Zhai et al., 2004). In model calculations, the eddy heat fluxes are quite significant because locally such fluxes can be of magnitude equal to that provided by the mean circulation (Drifhout and Walsteijn, 1997). Drifhout and Walsteijn (1997) have also found that eddies induce a change in total heat transport comparable to the eddy heat transport itself. Hence another goal of this study is to quantify the role of eddies in heat transport in the sub-polar North Atlantic. These transports have been under-predicted in some studies, for example, Jayne and Marotzke (2002) shows poleward eddy heat transport of 0.1 PW at 40°N which is about half that reported by observational studies such as Stammer (1998). For a detailed description of oceanic heat transport see Bryden and Imawaki (2001).

The total freshwater transport in the North Atlantic has been documented in Wijffels (2001). Historically, most estimates of oceanic freshwater transport are derived indirectly from measurements of atmospheric vapour transport or from surface observations of rainfall rates and the variables required to estimate evaporation (Wijffels, 2001). Some direct estimates of freshwater transport also exist (eg. Large et al., 1997). Nevertheless, large uncertainties still exist in the observed climatology of freshwater transport and it remains hard to validate models. On the other hand, direct or indirect results of eddy freshwater transport do not exist. This study will quantify eddy freshwater transport in our model.

In this paper, section 3.2 discusses how the combination of the semi-diagnostic approach (Zhai et al., 2004) and the spatially varying eddy transfer coefficient of Visbeck et al. (1997) interact in the model. The ocean general circulation model used in this study is discussed in section 3.3 while the model results are discussed in section 3.4. A brief summary and discussion are presented in section 3.5.

3.2 Methods

An equation of the large-scale tracer ($\overline{\tau}$) evolution in isopycnal coordinates is (Gent et al., 1995):

$$\frac{\partial \overline{\tau}}{\partial t} + \left(\overline{\mathbf{v}} + \left(\overline{h'_\rho \mathbf{v}'}\right)/\overline{h_\rho}\right) \cdot \nabla_\rho \overline{\tau} = \nabla_\rho \cdot \left(\mu h_\rho \nabla_\rho \overline{\tau}\right)/h_\rho \tag{3.1}$$

where t is time, h_ρ is thickness, ρ is density, $\overline{\mathbf{v}}$ is the large scale horizontal velocity, $\mathbf{v}'$ is an eddy induced velocity, ∇_ρ is the gradient operator in the constant ρ plane, and μ is a turbulent diffusion coefficient. In height coordinates Eq. 3.1 becomes (Gent et al., 1995):

$$\frac{\partial \overline{\tau}}{\partial t} + (\mathbf{v}+\mathbf{v}^*) \cdot \nabla_z \overline{\tau} + (w+w^*) \frac{\partial \overline{\tau}}{\partial z} = R(\mu, \overline{\tau}) \tag{3.2}$$

where $(\mathbf{v}, w)$ is the large scale velocity in which $\mathbf{v}$ is the horizontal and w is the vertical velocity, $(\mathbf{v}^*, w^*)$ is an eddy induced velocity, and $R(\mu, \overline{\tau})$ is the transformation of the right-hand side of Eq. 3.1.

Gent and McWilliams (1990) proposed the following subgridscale parameterization for the eddy-induced velocity:

$$\begin{aligned} \mathbf{v}^* &= \frac{\partial}{\partial z}\left(k \mathbf{s}_{rho}\right) \\ w^* &= -\nabla_h \cdot \left(k \mathbf{s}_{rho}\right) \end{aligned} \tag{3.3}$$

where $\mathbf{s}_{rho}$ is the isopycnal slope. The variable k (units $\mathrm{m^2 s^{-1}}$) is an eddy transfer coefficient or eddy diffusivity which may be treated either a constant in space and time or as variable. When k is variable, it can be represented as (Visbeck et al., 1997):

$$k = \alpha T^{-1} L^2 \tag{3.4}$$

where $\alpha = 0.015$, L is the length scale of baroclinic region, and T^{-1} is the Eady growth rate of unstable baroclinic waves and is given by:

$$T^{-1} = \frac{f}{\sqrt{Ri}} \tag{3.5}$$

in which f is the Coriolis parameter and Ri is the Richardson number given as

$$Ri = \frac{(-g/\rho_o)\, d\rho/dz}{\left(\frac{du}{dz}\right)^2 + \left(\frac{dv}{dz}\right)^2} \tag{3.6}$$

An implementation of the Visbeck et al. (1997) scheme is outlined in Deacu and Myers (2005).

In order to assimilate observational data, the semi-diagnostic approach (Zhai et al., 2004) can be used. This can compensate for erroneous or missing model physics. The method makes adjustments by replacing the density field in the hydrostatic equation by a linear combination of model computed (ρ_m) and climatological density (ρ_c) :

$$\begin{matrix} & (I) & (II) \\ \frac{\partial p}{\partial z} = & -g\rho_m & - \overline{g(\rho_c - \rho_m)} \end{matrix} \tag{3.7}$$

Term (II) in Eq. 3.7 is a new term in the hydrostatic equation and is filtered spatially. A scale of 300 km (sufficient to release the eddy field) is used based on the analysis of Zhai et al. (2004) for filtering represented by the overbar in Eq. 3.7. High resolution 3D temperature and salinity climatological data for the Labrador Sea (Kulan and Myers, 2006) merged with the annual Levitus (1982) climatology is used for climatological density (ρ_c) in this study. An instantaneous correction velocity ($\tilde{\mathbf{v}}$) is associated with the new term in the hydrostatic Eq. 3.7 that affects the velocity terms in the momentum equation (Sheng et al., 2001).

In the original semi-prognostic method (Sheng et al., 2001) the second term in the hydrostatic equation is modified by a constant from 0 to 1. In this study a constant

of value 0.5 is used for the semi-prognostic case as originally utilized by Sheng et al. (2001). When the constant is equal to 1, Eq. 3.7 becomes the semi-diagnostic method of Zhai et al. (2004). An advantage of the semi-diagnostic method (Zhai et al., 2004) over the semi-prognostic method (Sheng et al., 2001) and the corrected semi-prognostic method (Eden et al., 2004) is that it allows the large-scale mean flow of the model field to be fully constrained by climatology. In Eden et al. (2004) and Sheng et al. (2001) where a constant of 0.5 is used, only 50% of the mean flow field of the model is constrained by climatology (Zhai et al., 2004). In this study, the original semi-prognostic scheme (Sheng et al., 2001) is also shown for comparison.

3.3 Model

The numerical experiments performed in this study were made with a primitive equation model called the Sub-Polar Ocean Model (SPOM) (Myers, 2002) which is a regional configuration of the Modular Ocean Model Array (MOMA) set up specifically for process and sensitivity studies of ocean variability questions in the sub-polar North Atlantic. Some aspects of the model are described in this section while detailed information is found in Myers (2002). This model is based on the Bryan-Cox-Semtner type ocean general circulation model using the inviscid version of the Killworth et al. (1991) free surface scheme.

The model covers the subtropical North Atlantic between 68°W and Greenwich 0° and 38°N and 70°N with a resolution of 1/3° in latitude by 1/3° in longitude. The southern boundary is open while restoring buffer zones are included along the model's closed northern boundaries. In the vertical there are 36 layers, with a spacing of 10 m in the uppermost layer and smoothly increasing to 250 m at 2500 m depth. Below 2500 m the vertical grid box thickness is a constant 250 m up to a maximum depth of 5500 m. The topographic data is from 1/12° Earth TOPOgraphy-5 minute (ETOPO5)

(NOAA, 1988) dataset, linearly interpolated to the model's $1/3^o$ resolution. The bottommost cell in each column is partially filled (Adcroft et al., 1997) while ensuring that no partially filled layer has less than 10 m of water in it.

The initial conditions are taken from the NODC (1994) dataset, linearly interpolated to the model grid and depth levels. The themohaline boundary conditions at the sea surface are taken from the NODC, with a timescale of 2 hours. As discussed in Myers (2002) this choice is made to fix the potential water formation regions while leaving the basin interior free to evolve. The wind stress is also derived from the European Centre for Medium Range Weather Forecasts (ECMWF) analysis (Trenberth et al., 1990) averaged over the period 1980-1986.

The coefficients used in the SPOM model are: biharmonic horizontal viscosity coefficient ($A_h = 7.5 \times 10^{18}\,\mathrm{cm^2 s^{-1}}$), biharmonic diffusion coefficient ($K_h = 7.5 \times 10^{14}$ $\mathrm{cm^2 s^{-1}}$) vertical diffusion coefficient ($K_v = 0.3\ \mathrm{cm^2 s^{-1}}$), and vertical viscosity coefficient ($A_v = 1.5\,\mathrm{cm^2 s^{-1}}$). Convective adjustment is performed using the complete convection scheme of Rahmstorf (1993). To resolve the fast external gravity waves, the barotropic velocity fields and the free surface height are calculated using a small timestep (30 seconds) while a larger timestep (1800 seconds) is used for the baroclinic part of the model. The constant value of the eddy transfer coefficient used in experiments where the variable eddy transfer scheme is not used is $2.74 \times 10^6\,\mathrm{cm^2 s^{-1}}$. This value is the spatial and temporal average of the eddy transfer coefficient calculated in Deacu and Myers (2005).

3.4 Results and discussion

The hybrid schemes arising from the use of constant k (SDC) and variable k (SDV) are the focus of most discussions. For comparison, results from prognostic experiments employing a constant k (PC) and a variable k (PV) are also shown. Two

further experiments with semi-prognostic methods having a constant k (SPC) and a variable k (SPV) are also analyzed. A summary of the experiments is shown in Table 3.1. The constant value of $k = 2.74 \times 10^6\,\mathrm{cm^2 s^{-1}}$ shown in Table 3.1 is the spatial and temporal average of the transfer coefficient calculated over the last 4 years of the integration of Deacu and Myers (2005) in their SHEAR experiment. Further details of the implementation of the Visbeck et al. (1997) scheme can be found in Deacu and Myers (2005).

Method		Eddy transfer coefficient (k)
Prognostic	PC	$2.74 \times 10^6\,\mathrm{cm^2 s^{-1}}$
	PV	variable ($(0.5 - 10) \times 10^6\,\mathrm{cm^2 s^{-1}}$)
Semi-diagnostic	SDC	$2.74 \times 10^6\,\mathrm{cm^2 s^{-1}}$
	SDV	variable ($(0.5 - 10) \times 10^6\,\mathrm{cm^2 s^{-1}}$)
Semi-prognostic	SPC	$2.74 \times 10^6\,\mathrm{cm^2 s^{-1}}$
	SPV	variable ($(0.5 - 10) \times 10^6\,\mathrm{cm^2 s^{-1}}$)

Table 3.1: Summary of the experiments performed using the prognostic, semi-prognostic and semi-diagnostic methods. The letters C and V in PC, PV, SDC, SDV, SPC, SPV represent constant eddy transfer coefficient k or a variable eddy transfer coefficient k respectively.

3.4.1 Annual mean fields

Observations (OBS; from the high resolution climatology of Kulan and Myers (2006)) is shown in Fig. 3.1. The annual means of the salinity field obtained from the averages of years 10 to 14 for model level 3 (52 m) is shown in Figs. 3.1-3.3 for all the simulations, together with their difference plots for each of the simulations. Most of the well known features are reproduced by the model in all experiments except for some fine details which are better in some than in others. Two important features that show distinctive differences are the representation of the Gulf Stream (as in Sheng et al., 2001) and the broad region of high salinity extending from the east and filling most of the Labrador Sea.

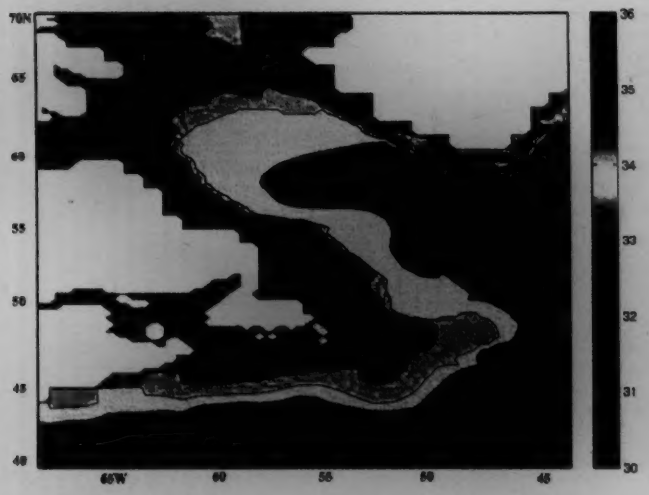

Figure 3.1: The annual mean climatology salinity field (OBS; Kulan and Myers, 2006) at model level = 3 (52m). The contour interval is 0.5.

Consistent with the results reported by Sheng et al. (2001) and Zhai et al. (2004), there are differences in the representation of the tight gradient of the Gulf Stream. The PC and PV fields show weak gradients with no obvious difference between PC and PV cases. In SDC case the region of the tight gradient has slightly shifted southwards. The rest of the simulations maintain the tightness and position of the Gulf Stream as contained in the assimilated fields. Most of the simulations also have a broad region of high salinity filling most of the Labrador Sea. In the PC, SPC and SDC experiments, high salinity is found everywhere in the interior of the Labrador Sea. Only in the PV and SDV experiments is the high salinity water correctly represented as a warm (as seen in the temperature field) tongue entering from the Irminger Sea and cyclonically circulating around the basin. The sea surface height fields (SSH, not shown) show a strong similarity between the SDC and SDV cases. In the other experiments the area that is poorly modelled is the central Labrador Sea, with the SSH fields slightly lower than observed.

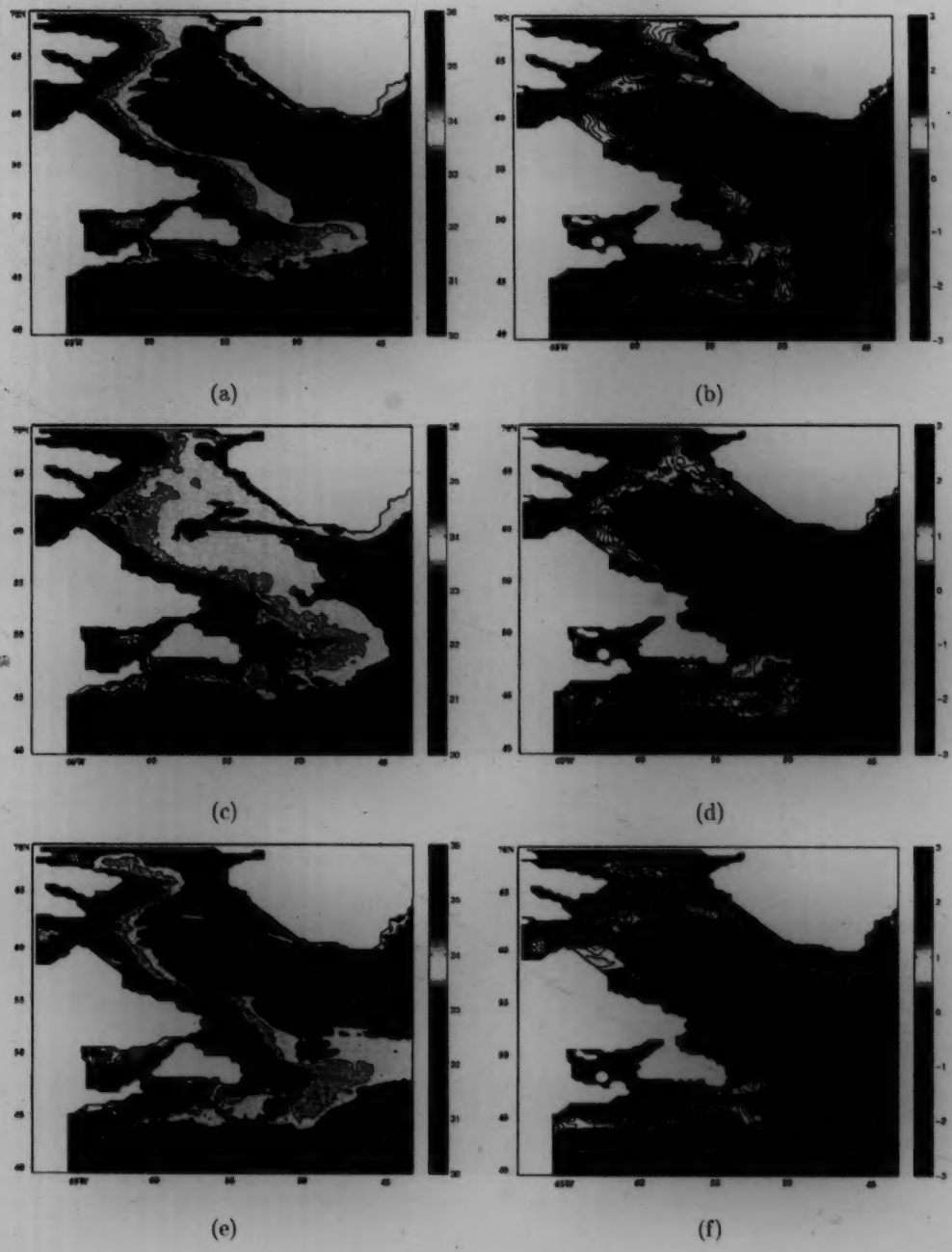

Figure 3.2: The annual mean salinity field at model level = 3 (52m) showing computations using (a) PC, (b) PC-OBS (c) PV, (d) PV-OBS, (e) SDC, and (f) SDC-OBS. The contour interval is 0.5. OBS fields are given in Fig. 3.1.

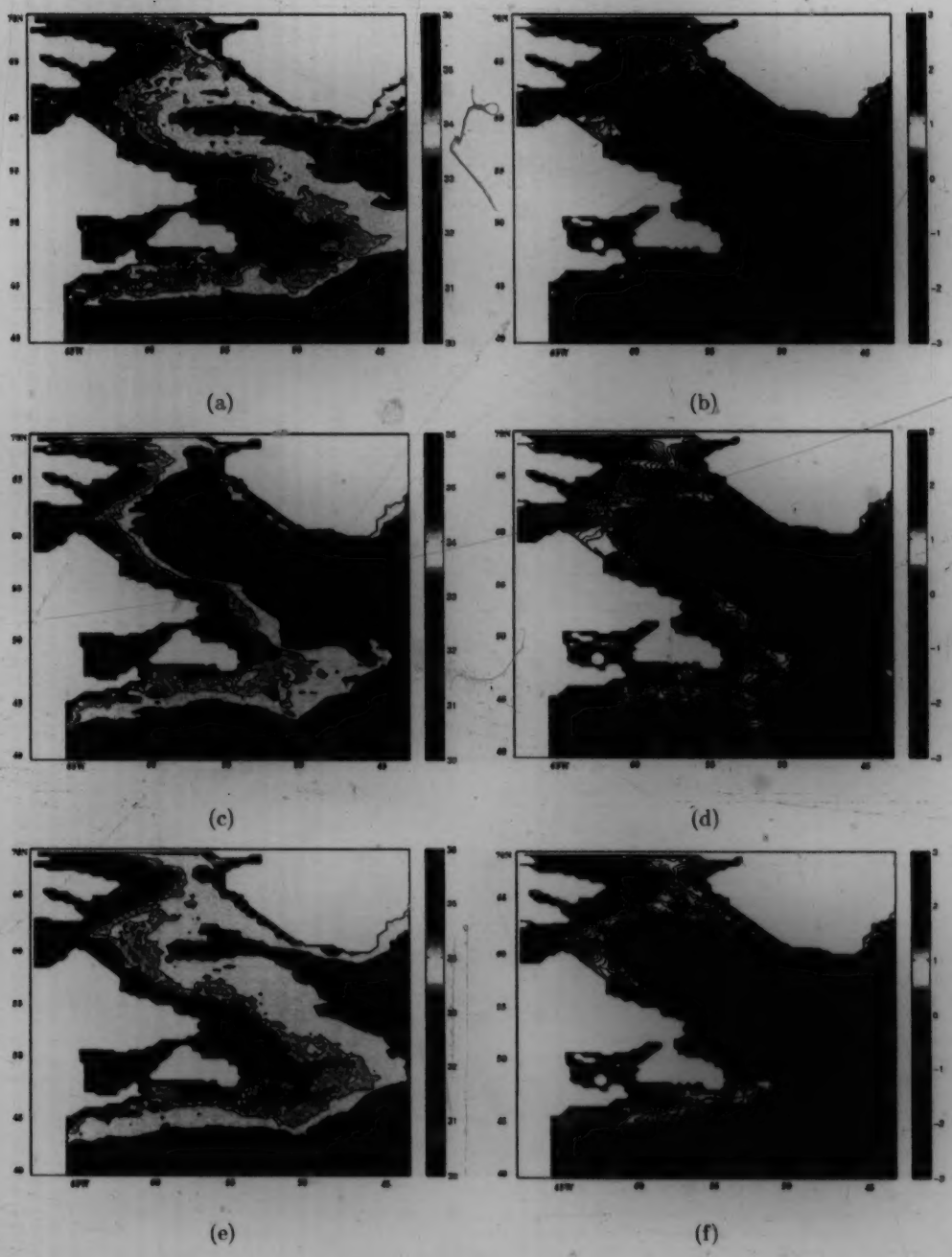

Figure 3.3: The annual mean salinity field at model level = 3 (52m) showing computations using (a) SDV, (b) SDV-OBS (c) SPC, (d) SPC-OBS, (e) SPV, and (f) SPV-OBS. The contour interval is 0.5. OBS fields are given in Fig. 3.1.

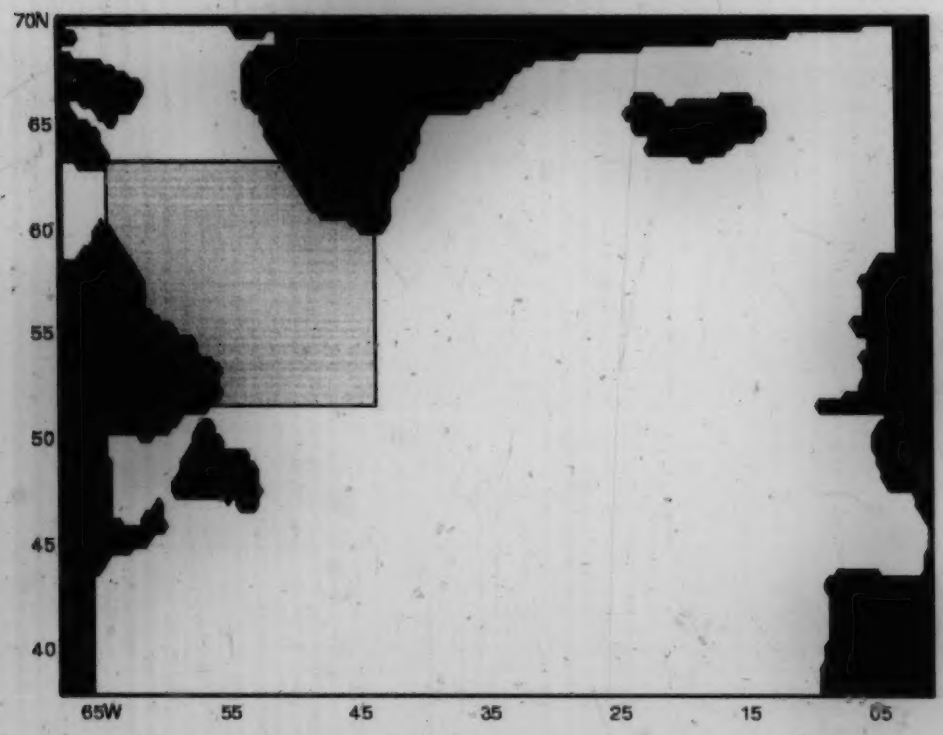

Figure 3.4: The shaded region shows the Labrador Sea box used in this study.

3.4.2 Freshwater content

The freshwater content is defined as:

$$\mathrm{FW} = \int_V \frac{S_r - S}{S_r} \mathrm{d}V \tag{3.8}$$

where V is the volume of Labrador Sea, S is the model calculated salinity and S_r is a reference salinity (with a value of 35.0 - chosen to be consistent with the model salinity at the offshore edge of the Labrador Current, see Myers (2002) for more details). For the purpose of this analysis, the Labrador Sea is the area defined in Fig. 3.4.

Fig. 3.3 shows the seasonal freshwater content time series for each of the 6 experiments. There is a large decrease in freshwater content (of about $6.4 \times 10^{12}\,\mathrm{m}^3$) in the Labrador Sea upto year 2, after which such a large decrease is not evident. If

we take the volume flux of Irminger Current to be 175 mSv (Chapter 4; this is equal to $175 \times 10^3\,m^3/s \times 31536000\,s = 5.5 \times 10^{12}\,m^3/yr$). In two years Irminger current would supply $11 \times 10^{12}\,m^3$ of salty water to Labrador Sea, about twice as large as the amount lost from Labrador Sea. It should be noted that rest of the water mass from the Irminger Current circulates along the boundary of the Labrador Sea. Hence this analysis does show that freshwater content loss in the Labrador Sea could be due to inadequate representation of Irminger Current that unltimately leads to a large supply of salty water into the Labrador Sea.

In Fig. 3.3 all the experiments start at the same initial condition (based on the NODC climatology) but they quickly diverge. There are 3 clear groupings evident from Fig. 3.3: The PC, SPC and SDC are in one group, PV and SPV in the second group while SDV stands out from the rest of the methods. In all the methods (except SDV) there is an initial sharp decrease during the first 2 years, followed by reduced drift. The final year 14 shows SDC having the lowest of the freshwater content. In SDC the freshwater content has decreased by 59% in year 14. The next two methods which show closer resemblance but show better freshwater content are the PC and SPC methods, each having 46% and 56% freshwater content decrease respectively by year 14. There is no improvement in SDC and SPC methods over the PC method, suggesting the assimilation on its own is not removing the model drifts. This point will be discussed in greater detail in section 3.5.

The PV and SPV are slightly better with just 30% and 32% decrease in year 14, implying some improvements in reducing drift through better eddy representation. The method that best represents the freshwater content is the SDV method. In year 14 there is only a 14% decrease in freshwater content, the lowest of all the methods. Although the freshwater content has not stabilized in the SDV method, the drift has reduced by year 14. Hence, the SDV approach shows that assimilation (as in SDC) or improved eddy representation (as in PV) on their own do not prevent model drift but

a combination of both approaches yields a dramatic improvement. One additional effect of the assimilation is to reduce the annual cycles in the freshwater content.

The root mean square error (rmse) between the observed and the model computed freshwater content for Figs. 3.5, 3.6 are shown in Table 3.2. Since the SDV method deviates the least from the observation, it has the lowest rmse for both the total (all levels) and the top levels (levels 1-17). As far as the error in Eq. 3.8 is concerned, which contributes to Fig. 3.5, it basically arises from salinities that have errors in the range ± 0.11 (Chapter 1.1) which is a 0.3% error. Hence for Fig. 3.5 putting error bars of $\pm 0.01 \times 10^{12}\,\mathrm{m}^3$ is not of importance when all the experiments have reduced FW content by as much as $5 - 11 \times 10^{12}\,\mathrm{m}^3$. These observational errors are much smaller than the systematic error due to model drift. This applies to all the figures in this chapter.

Method		Freshwater Content($\times 10^{12}\,\mathrm{m}^3$)	
		total	top
Prognostic	PC	5.7	4.1
	PV	3.6	2.3
Semi-diagnostic	SDC	6.0	3.5
	SDV	1.2	1.1
Semi-prognostic	SPC	6.1	4.4
	SPV	3.6	1.9

Table 3.2: Root mean square errors shown of the freshwater content for the Limited Labrador Sea regions (calculated for all model layers (total) and levels 1-17 (top)).

3.4.3 Role of eddies

The semi-diagnostic approach can be also used to determine the role of eddies based on the model results in the semi-diagnostic and pure diagnostic experiments. A diagnostic run:

$$\frac{\partial p}{\partial z} = -g\overline{\rho_c} \tag{3.9}$$

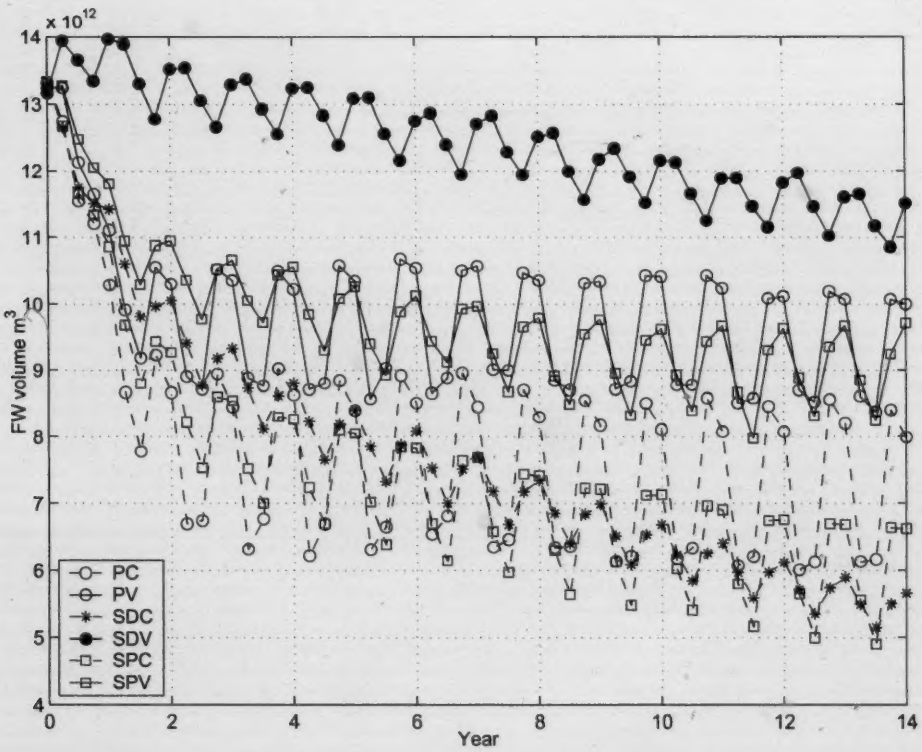

Figure 3.5: The total freshwater (FW) content in the Labrador Sea for the PC, PV, SDC, SDV, SPC and SPV methods.

when subtracted from a semi-diagnostic run leaves the eddy field as the residual (Zhai et al., 2004). This is used to calculate the freshwater content due to eddies, eddy heat transport and eddy freshwater transport.

3.4.3.1 Freshwater Content

If the eddies are assisting in the restoration of the freshwater content then their role should be more prevalent in the upper layers (e.g. Qiu and Chen, 2003). Qiu and Chen (2003) calculated heat transport by eddies from a combination of satellite-derived sea surface height and temperature data with Argo float temperature-salinity data and found that for the North Pacific gyre the eddy-induced heat transport occurs largely in the surface seasonal thermocline (0-200 m). Jayne and Marotzke (2002)

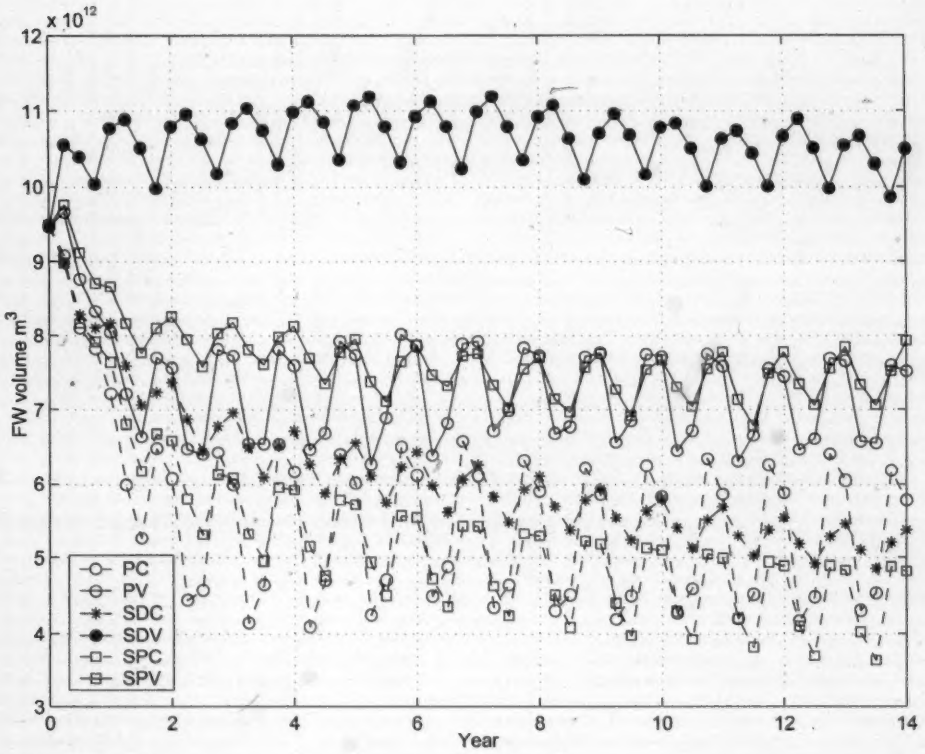

Figure 3.6: The total freshwater (FW) content in the upper layer (model levels 1-17) in the Labrador Sea for the PC, PV, SDC, SDV, SPC and SPV methods.

also found the eddy heat transport to be confined to the upper 1000 m of the ocean. As such the total freshwater content in the Labrador Sea is calculated for model levels 1-17 (0-1068 m). The results are shown in Fig. 3.6. The upper layer drift in Labrador Sea salinity and freshwater content seen in most modelling studies of the region (eg. Treguier et al., 2005) now no longer occurs in the SDV method (earlier presented in Fig. 3.3). The drift, however, remains significant in all other simulations. The drift in the deeper layers of the SDV case is probably related to processes occurring at the overflows of the Nordic Seas.

3.4.3.2 Heat transport

The meridional heat transport $H(\phi)$ as a function of latitude (ϕ) and time is computed by calculating the vertical integral of the temperature flux ($\overline{v}\overline{T}$) across zonal cross-sections (A) bounded by the continents:

$$H(\phi) = \rho_0 c_p \int_A \overline{v}\,\overline{T}\,\mathrm{d}A \tag{3.10}$$

in which ρ_0 is density of water and c_p is specific heat capacity of water.

The total meridional heat transport in the PC, PV, SDC and SDV cases are given in Fig. 3.7. Also shown for comparison is an estimate from observation (MacDonald and Wunsch, 1996). Bryden and Imawaki (2001) have summarized a number of direct and indirect estimates of heat transport but mostly of the South Atlantic. The total heat transports in both the PC and PV methods are much larger than observations due to poor representation of the North Atlantic Current in these experiments. The application of the SDC and SDV methods significantly improve the transports. The total heat transport for the SDV method is, however, closer to the observed value than the SDC at the latitude shown although both fall within the error bar. In both approaches the general feature of the graph remains the same. However, there is a significant difference in the magnitudes. The maximum SDV magnitude (0.8 PW) is about twice as much as in SDC (0.45 PW).

The SDV eddy heat transport curve also shown in Fig. 3.7 remains close to maximum upto 53°N, consistent with its corresponding total heat transport curve. At all latitudes the eddy heat transport curve is positive indicating a net poleward eddy heat transport. The SDC eddy heat transport, on the other hand, is not only weak but it also shows a net equatorward eddy heat transport. An observational estimate (Stammer, 1998) shows poleward eddy heat transport of about 0.2 PW at 40°N. The SDV eddy heat transport curve's shape and sign are similar to a previous

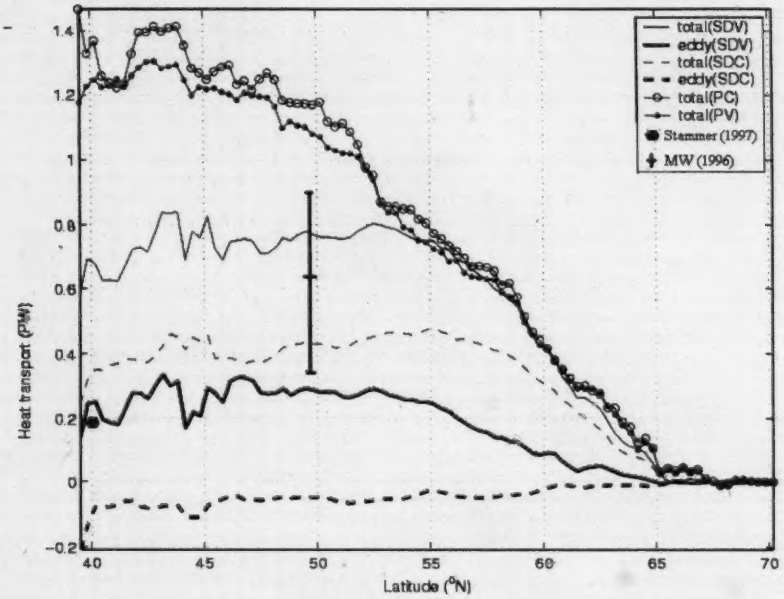

Figure 3.7: Zonally integrated total time-mean heat transport in PW for SDV (thin line) and SDC (thin dashed line) together with their eddy components with corresponding thick lines. PC and PV curves are also shown for comparison. The annual averages were obtained from the monthly averages for the 4 years between 10 to 14. Observational total heat transport of MacDonald and Wunsch (1996) and eddy heat transport of Stammer (1998) are also shown.

modelling study (Jayne and Marotzke, 2002). However, the magnitude reported in Jayne and Marotzke (2002) is smaller by a factor of 2, largely due to the eddy kinetic energy being too weak in their model.

The total zonal heat transport curve for the North Atlantic is shown in Fig. 3.8. It is plotted as a function of longitude and obtained using an equation similar to Eq. 3.10 with meridional velocity v being replaced by the horizontal velocity u and A being meridional cross-sections:

$$H(\phi) = \rho_0 c_p \int_A \overline{u}\,\overline{T}\,\mathrm{d}A \tag{3.11}$$

In both of the approaches the total heat transport is eastwards. Again, the SDV

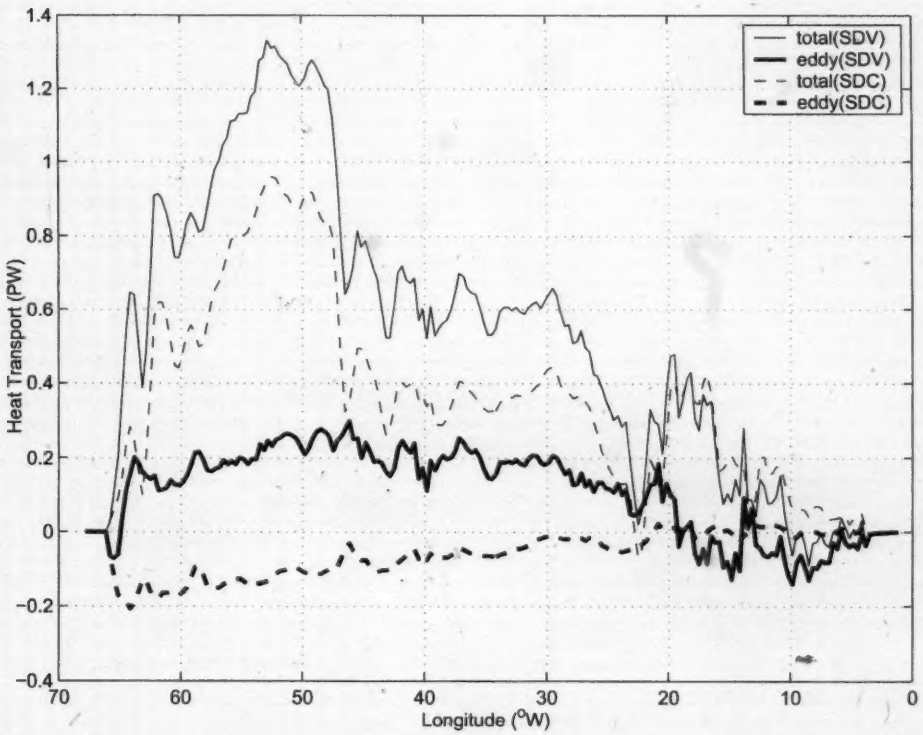

Figure 3.8: Meridionally integrated total time-mean heat transport in PW for SDV (thin line) and SDC (thin dashed line) together with their eddy components with corresponding thick lines. The annual averages were obtained from the monthly averages for the 4 years between 10 to 14.

method shows a higher total heat transport than the SDC method although the difference is not that large as that in the meridional transport. The maximum is also quite distinct and occurs near 55°W – 45°W, associated with the North Atlantic Current. The eddy heat transport in the SDV method is also positive upto 20°W and its sign appears to be again modulated by the North Atlantic Current. Beyond 20°W the westward eddy heat transport appears to be largely influenced by the northeastern Atlantic currents. Again the SDC results show opposite eddy heat transport to the SDV results.

3.4.3.3 Freshwater transport

The meridional fresh water transport $F(\phi)$ as a function of latitude (ϕ) is computed by calculating the vertical integral of the freshwater flux $v(S_r - S)/S_r$ across zonal cross-sections (A) bounded by the continents:

$$F(\phi) = \int_A \bar{v} \frac{S_r - \bar{S}}{S_r} \mathrm{d}A \tag{3.12}$$

The total meridional freshwater transport in SDC and SDV is given in Fig. 3.9. Three estimations from observations (Wijffel et al., 1992) show the minimum freshwater transport occurring between 30°N – 50°N with minima of about -0.3Sv to -0.5Sv. Large et al. (1997) also show a total freshwater transport curve that is similar to the one given in this study except that it has a minimum occurring near 45°N. Large et al. (1997) also mention large uncertainties in their climatology and model results that could explain this difference. Nevertheless, the estimations are in closer agreement with the values shown for SDV than SDC. The total freshwater transport using the SDC case is again weaker. The difference is almost entirely due to the eddy component of the freshwater transport. The SDC, on the other hand, shows a weak poleward freshwater transport.

The total zonal freshwater transport curve for the North Atlantic is also shown in Fig. 3.10. It is plotted as a function of longitude and obtained using the horizontal velocity u and the meridional crossections A :

$$F(\phi) = \int_A \bar{u} \frac{S_r - \bar{S}}{S_r} \mathrm{d}A \tag{3.13}$$

In both the SDC and SDV methods the total freshwater transport is westwards. The sign of the meridional average is dominated by the North Atlantic Current (this is clearly shown in the depth integrated freshwater transport in Fig. 3.9a,b) which transports salt eastwards (hence freshwater transport westwards). The eddy freshwa-

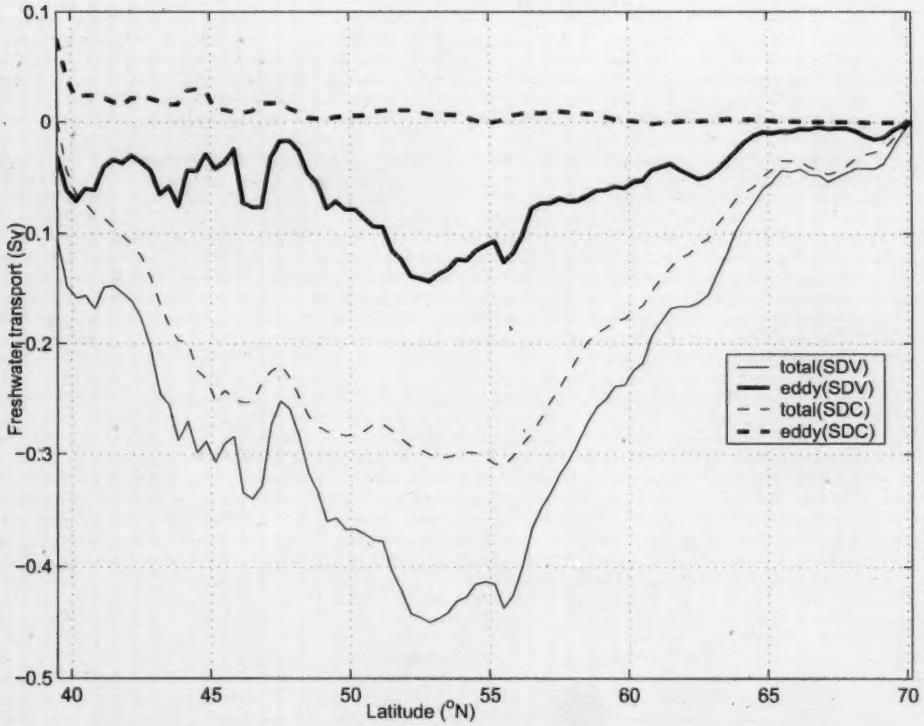

Figure 3.9: Zonally integrated total time-mean freshwater (FW) transport in Sv for SDV (thin line) and SDC (thin dashed line) together with their eddy components with corresponding thick lines. The annual averages were obtained from the monthly averages for the 4 years between 10 to 14.

ter transport curves for both the SDC and SDV cases, however, show mostly positive or eastward eddy transport (and representing about 1/3 of the total transport). This is associated with the eastward transport by eddies in the Labrador Current.

The depth integrated annual freshwater transport (Figs. 3.11a,b) suggest enhanced freshwater transport in the Labrador Current and the West Greenland Current in the SDV case compared to the SDC case. There are no significant differences in the Gulf Stream in either methods. In SDV, the eddies have strengthened the freshwater transport in the Labrador Current and the West Greenland Current. There is also a greater freshwater transport out of Baffin Bay in the Buffin Island Current.

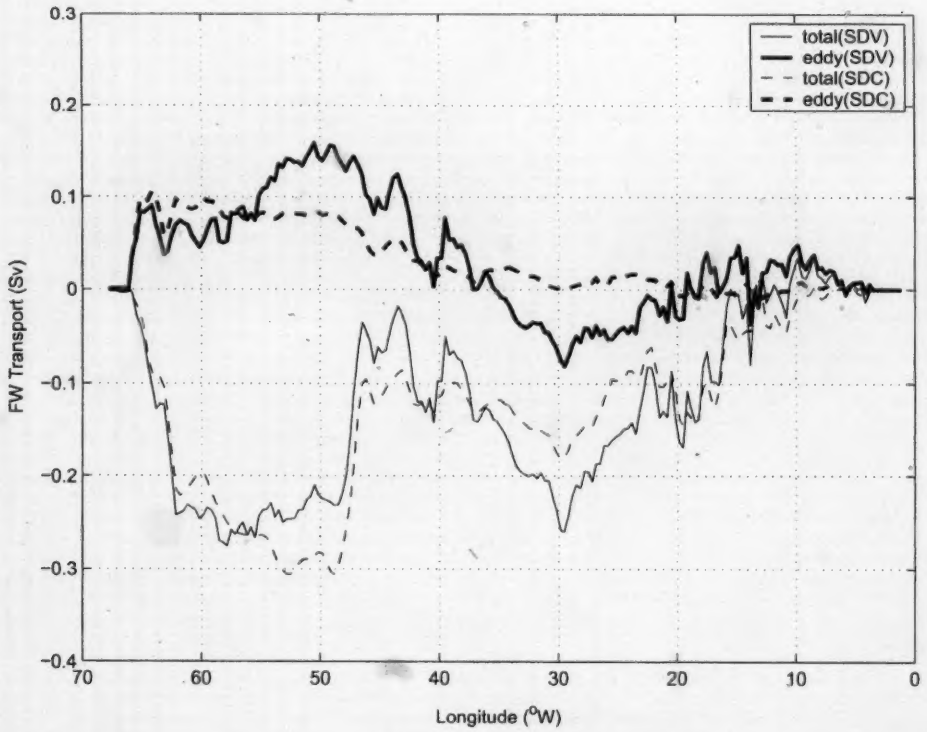

Figure 3.10: Meridionally integrated total time-mean freshwater (FW) transport for SDV (thin line) and SDC (thin dashed line) together with their eddy components with corresponding thick lines. The annual averages were obtained from the monthly averages for the 4 years between 10 to 14.

3.5 Summary

The Labrador Sea plays a significant role in the thermohaline circulation as the formation site of the Labrador Sea Water. Hence better representation in models is needed of circulation and hydrography of the Labrador Sea together with the sub-polar North Atlantic. A number of studies in this region have adequately represented the circulations while the hydrography has been observed to have deteriorated (Myers and Deacu, 2004). Modelling studies (eg. Myers and Deacu, 2004) and a recent comparison of the North Atlantic sub-polar gyre in four high resolution models (Treguier et al., 2005) have shown a large drift in water mass properties with a salinization of the

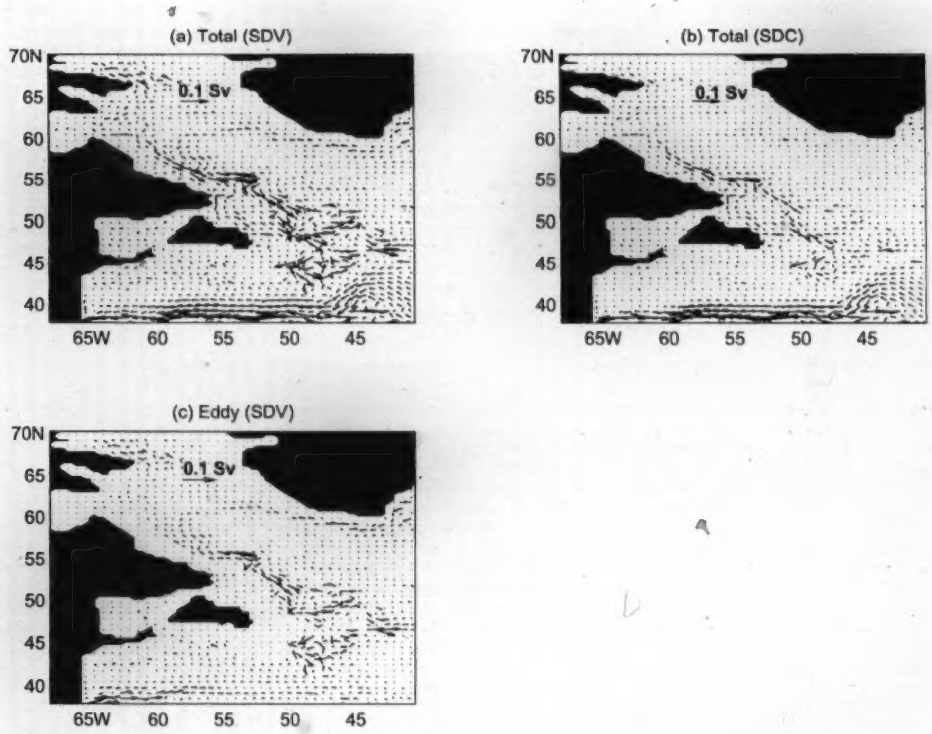

Figure 3.11: Total depth integrated time-mean freshwater (FW) transport showing (a) total SDV, (b) total SDC and (c) eddy component of SDV. The annual averages were obtained from the monthly averages for the 4 years between 10 to 14.

Labrador Sea Water. To reduce this drift in water mass properties is the main issue that is investigated in this study. Two potential approaches previously explored are improvements in subgridscale parameterization by better eddy representation (Deacu and Myers, 2005) and restraining the model's evolution by using data assimilation (Greatbatch and Zhai (2006), Zhai et al. (2004)). It is anticipated that with improved subgridscale parameterization, the ocean circulation and hydrography would be simultaneously improved in an ocean model during data assimilation. Six experiments are performed using the prognostic, semi-diagnostic and a semi-prognostic schemes, utilizing constant and variable eddy transfer coefficients.

The differences in the six experiments highlight the ability of semi-prognostic or semi-diagnostic schemes to constrain large scale climatology while improved eddy pa-

rameterization plays a role in reducing drift in localised regions. The improvements in constraining large scale climatology through the semi-prognostic and semi-diagnostic approach are as shown previously in detail by Sheng et al. (2001), Eden et al. (2004) and Zhai et al. (2004). The prognostic schemes are found not to represent the tight gradients of the Gulf Stream while the freshwater content drift continues in the interior of Labrador Sea. The semi-prognostic methods do provide a tight Gulf Stream but there is no significant improvement in the freshwater content drift. In both these methods, the experiments having variable eddy transfer coefficient also show slight improvements over their counterparts with constant eddy transfer coefficient. The semi-diagnostic scheme without the variable eddy transfer coefficient (SDC) does not do equally well as the rest of the methods; it still contains a large localized regional model drift in freshwater content. The circulation in the interior of the Labrador Sea is also found not to be well represented: high salinity and warm water are present. However, the deficiencies in the model are dramatically reduced when the semi-diagnostic variable approach (SDV) that utilizes variable eddy transfer coefficient and the semi-diagnostic approach is added. An improved representation of the circulations, including the tight gradients in the Gulf Stream and the interior Labrador Sea together with a reduced freshwater content drift, is observed using the SDV approach. Hence this shows that independent improvements in subgridscale parameterization and data assimilation do not resolve the problem of hydrographic drift in eddy-permitting models of the North Atlantic sub-polar gyre. A hybrid approach containing both the subgridscale parameterization and data assimilation best addresses the problem of simultaneously representing the large scale circulation and localised hydrography.

Zhai et al. (2004) pointed out that one of the advantages of the semi-diagnostic method is that it eliminates model drift. Nevertheless, we find a significant drift in freshwater content in the Labrador Sea in our SDC experiment. What might explain

this discrepancy? The right hand side of the semi-diagnostic hydrostatic equation averaged over some domain is $\overline{-g\rho_m - g(\rho_c - \rho_m)}$. If we carry out the averaging over the entire domain, we do indeed find that this term is equal to $\overline{\rho_c}$ $(= 1027.4)$, consistent with the statement of Zhai et al. (2004) that the solution is constrained by the large-scale climatology. However, if we average over a smaller domain (though still larger than the 300 km filtering scale), such as the Labrador Sea, then we find that the two terms above do not balance, with $\overline{\rho_m} = 1027.0$ not equal to $\overline{\overline{\rho_m}} = 1027.3$ due mainly to small drift in model temperature and salinity fields. Thus the filtered ρ_m is weighted by data outside a limited domain, which allows drift. Hence, although the semi-diagnostic method will prevent drift of basin averaged quantities, as shown by Zhai et al. (2004), it will not necessarily prevent model drift in limited domains.

The semi-diagnostic scheme used in this study is also a method that can be utilized for eddy diagnostics. Eddy diagnostic results show that eddies are playing a significant role in maintaining the circulation and the freshwater content of the Labrador Sea. Since eddies are dominant in the upper layer, freshwater content in the upper layer (0-1000 m) shows almost no drift (in SDV) as freshwater is advected into the interior of the Labrador Sea. The depth integrated freshwater transport field in the Labrador Sea further shows that the restoration of the upper layer and total freshwater contents (in SDV) could be attributed to the presence of enhanced eddy transport in the Labrador Current and the West Greenland Current. The inability of the SDC method to restore the freshwater content could be explained by the under-representation of eddies in these two currents. Yet this is not because of an unrealistic damping of eddies in the SDC approach (Zhai et al., 2004). In Figs. 3.7,3.8 the magnitude of the SDC eddy heat component is on average 0.1PW which is about half that of SDV (0.2PW). In Fig 3.9, the SDV eddy freshwater curve is on average -0.1 Sv while the SDC is again not zero, but around 0.02Sv. Fig. 3.10 shows that the SDC zonal eddy freshwater transport is almost comparable in magnitude to the SDV curve. Hence this study also

shows that eddy processes in the Labrador Current and the West Greenland Current play an important role in maintaining the freshwater content of the Labrador Sea and controlling the salinity drift in the Labrador Sea. Further, the absence of an overly strong counter-current as was suggested by Myers and Deacu (2004) transported excess salty North Atlantic Current water to the Labrador Sea also must play a role.

The importance of the eddies in the Labrador Sea and the sub-polar North Atlantic are studied further. Their quantitative and qualitative roles in zonal and meridional heat and freshwater transports are also determined. The total meridional (zonal) heat transport shows poleward (eastward) heat transport in both the SDV and SDC methods. The meridional (zonal) eddy heat transports are poleward (eastward) in SDV and in agreement with observations. However, in the SDC case the eddy heat transports are not only reduced by almost half, there is a reverse in transport sign. Hence, without good eddy representation there is an underestimation of poleward transports even in eddy permitting models. The freshwater transport curves obtained for the SDC and SDV methods again show similar results, and imply the superior performance of the SDV method over SDC when examining localised regions.

Finally, we note that this study has been carried out with a limited domain regional model. This implies issues with buffer zones in the north and an open boundary to the south. Without a doubt these affect the results presented here-in. However, previous studies with this model (eg. Myers, 2002 and Deacu and Myers, 2005) have shown that the model provides a good representation of the sub-polar gyre, away from the boundary regions. Furthermore, our focus in this paper is on comparing a number of different approaches in one model, all of which should be equally affected by the boundaries. A summary of the results obtained in this study is shown in Table 3.3.

Method	SDV	SDC
Mean Circulation	Labrador Sea mean circulations well represented. Tightness of the Gulf Stream gradient well represented in all fields examined.	High salinity and warm water present in interior of Labrador Sea.
Freshwater Content	Drift almost completely alleviated for both total and upper layers.	Drift still present in total and upper layers. Not much improvement over prognostic method.
Total Heat Transport	Poleward Magnitudes about twice as large as SDC. Magnitudes in closer agreement with observations.	Poleward
Eddy Heat Transport	Poleward	Transport signs reversed Magnitudes almost half
Total Freshwater Transport	Equatorward Magnitudes in closer agreement with observations.	Equatorward
Eddy Freshwater Transport	Equatorward Depth integrated transport shows enhanced eddy transport by the Labrador Current and West Greenland Current.	Transport signs reversed. Magnitudes relatively small.

Table 3.3: Summary of the results.

3.6 Acknowledgment

This research was funded by NSERC and CFCAS through the Canadian CLIVAR Network grants. The authors would like to thank Daniel G. Wright and two anonymous reviewers for useful comments.

Bibliography

[1] Adcroft, A., Hill, C., Marshall, J., 1997. Representation of topography by shaved cells in a height coordinate ocean model. Monthly Weather Review 125, 2293-2315.

[2] Bryden, H.L., and Imawaki, S., 2001. Ocean heat transport, in Ocean Circulation and Climate, edited by by G. Siedler, J. Church, and J. Gould, 455-474, Elsevier, New York.

[3] Cuny, J., Rhines, P.B., Niiler, P.P., Bacon, S., 2002. Labrador Sea boundary currents and the fate of the Irminger Sea Water. Journal of Physical Oceanography 32, 627-647.

[4] Deacu, D., and Myers, P.G., 2005. Effect of a variable eddy transfer coefficient in an eddy-permitting model of the Sub-Polar North Atlantic. Journal of Physical Oceanography 35, 289-307.

[5] Drijfhout, S.S., Walsteijn, F.H., 1997. Eddy-induced heat transport in a coupled ocean-atmospheric anomaly model. Journal of Physical Oceanography 28, 250-265.

[6] Eden, C., Boning, C. W., 2002. Sources of eddy kinetic energy in the Labrador Sea. Journal of Physical Oceanography 32, 3346-3363.

[7] Eden, C., Greatbatch, R.J., Boning, C. W., 2004. Adiabatically correcting an eddy-permitting model using large-scale hydrographic data: application to the gulf stream and the North Atlantic current. Journal of Physical Oceanography 34, 701-719.

[8] Gent, P.R., McWilliams, J.C., 1990. Isopycnal mixing in ocean circulation models. Jounal of Physical Oceanography 20, 150-155.

[9] Gent, P.R., Willebrand, J., McDougall, T., McWilliams, J.C., 1995. Parameterizing eddy-induced tracer transports in ocean circulation models. Journal of Physical Oceanography 25, 463-474.

[10] Greatbatch, R.J., Zhai, X., 2006. Influence of assimilated eddies on the large-scale circulation in a model of the northwest Atlantic ocean. Geophysical Research Letters 33, L02614, doi:10.1029/2005GL025139.

[11] Jayne, S. R., Marotzke, J., 2002. The oceanic eddy heat transport. Journal of Physical Oceanography 32, 3328-3345.

[12] Kase, R.H., Biastoch, A., Stammer, D.B., 2001. On the mid-depth circulation in the Labrador and Irminger Seas. Geophysical Research Letters 28, 3433-3436.

[13] Killworth, P.D., Stainforth, D., Webb, D.J., Paterson, S.M., 1991. The development of a free-surface Bryan-Cox-Semtner ocean model. Journal of Physical Oceanography 21, 1333-1348.

[14] Kulan, N., Myers, P.G., 2006. Comparing two climatologies of the Labrador Sea: geopotential vs isopycnal. Submitted to Atmosphere-Ocean.

[15] Large, W.G., Danabasoglu, G., Doney, S.C., 1997. Sensitivity to the surface forcing and boundary layer mixing in a global ocean model: annual-mean climatology. Journal of Physical Oceanography 27, 2418-2447.

[16] Levitus, S., 1982. Climatological atlas of the world ocean. NOAA Prof. Paper 13, U.S. Department of Commerce, 173 pp.

[17] MacDonald, A.M., Wunsch, C., 1996. An estimate of global ocean circulation and heat fluxes. Nature 382, 436-439.

[18] Myers, P.G., 2002. SPOM: A regional model of the sub-polar North Atlantic. Atmosphere-Ocean 40, 445-463.

[19] Myers, P.G., and Deacu, D., 2004. Labrador sea freshwater content in a model with a partial cell topographic representation. Ocean modelling 6, pp. 359-377.

[20] NOAA, 1988. Digital relief of the surface of the earth, Tech. Rep. Data Announcement 88-MGG-02, National Geophysical Data Center, Boulder, Colorado.

[21] NODC, 1994. World ocean atlas 1994 cd-rom data set documentation, Tech. Rep. NOAA, US Department of Commerce.

[22] Qiu, B., Chen, S., 2003. Seasonal modulations in the eddy field of the South Pacific ocean. Journal of Physical Oceanography 34, 1515-1527.

[23] Rahmstorf, S., 1993. A fast and complete correction for ocean models. Ocean Modelling 101, 9-11.

[24] Sheng, J., Greatbatch, R. J., Wright, D.G., 2001. Improving the utility of ocean circulation models through adjustment of the momentum balance. Journal of Geophysical Research 106, 16711-16728.

[25] Stammer, D., 1998. On eddy characteristics, eddy transports, and mean flow properties. Journal of Physical Oceanography 28, 727-739.

[26] Treguier, A.M., Theetten, S., Chassignet, E.P., Penduff, T., Smith, R., Talley, L., Beismann, J.O., Boning, C., 2005. The North Atlantic subpolar gyre in four high resolution models. Journal of Physical Oceanography 35, 757-774.

[27] Trenberth, K.E., Large, W.G., Olson, J.G., 1990. The mean annual cycle in global ocean wind stress. Journal of Physical Oceanography 20, 1742-1760.

[28] Visbeck, M., Marshall, J., Haine, T., Spall, M., 1997. Specifications of eddy transfer coefficients in coarse-resolution ocean models. Journal of Physical Oceanography 27, 567-580.

[29] Wijffels, S.E., 2001. Ocean transport of freshwater, in Ocean Circulation and Climate, edited by by G. Siedler, J. Church, and J. Gould, 475-488, Elsevier, New York.

[30] Wijffels, S.E., Schmitt, R.W., Bryden, H. L., Stigebrandt, A., 1992. Transport of freshwater by the oceans. Journal of Physical Oceanography 22, 155-162.

[31] Zhai, X., Greatbatch, R.J., Sheng, J., 2004. Diagnosing the role of eddies in driving the circulation of the northwest Atlantic ocean. Geophysical Research Letters 31, L233304, doi: 10.1029/2004GL021146.

Chapter 4

Impact of Subpolar Mode Water on Labrador Sea Water Formation

4.1 Introduction

The sub-polar North Atlantic is the northern part of the North Atlantic comprising the sub-polar gyre, the basic structure of which is set up by the large-scale atmospheric forcing and the underlying topography. The Labrador Sea is the westernmost arm of the gyre and is the formation site for the Labrador Sea Water (LSW) which plays a significant role in the lower limb of the global thermohaline circulation (Dickson and Brown, 1994). When strong winter northwesterly winds from the Canadian Arctic reach the Labrador Sea ice edge, they generate high air-sea heat fluxes that erode the surface stratification and allow deep convection (Cuny et al., 2002), leading to formation of LSW.

LSW is a special case of the water mass formed in the subpolar gyre called the subpolar mode water (SPMW) (McCartney and Talley, 1982). SPMW formation is associated with wintertime convective mixing in the subpolar gyre and can be identified by its distinctive pycnostads (Hanawa and Talley, 2001). In the far eastern

subpolar gyre, a branch of the North Atlantic Current (NAC) brings in warm and less dense pycnostads into the subpolar gyre, that circulates along the Reykjanes Ridge to form the Irminger Current (IC) which eventually circulates the eastern SPMW cyclonically around the boundary of the Labrador Sea (Cuny et al., 2002). During the course of the cyclonic circulation around the subpolar gyre, the pycnostads become denser and cooler through air-sea exchange to such an extent that the SPMW in the Labrador Sea is named Labrador Sea Water (Talley and McCartney, 1982). For the purpose of simplicity, the rest of the SPMW (in the eastern subpolar gyre ie. excluding LSW) in this study will be simply mentioned as SPMW.

The representation of LSW or SPMW is challenging even in high resolution modeling studies (eg. Eden and Boning, 2002). An examination of four high resolution models in the North Atlantic subpolar gyre (Treguier et al., 2005) found that although these models adequately represent the subpolar gyre circulation, there has been considerable degradation of water mass characteristics. These high resolution North Atlantic basin models were found to have a positive bias in the Labrador Sea salinity (Treguier et al., 2005), with strong implications for the LSW properties. Similar problems are also found to exist in lower-resolution eddy-permitting models of the subpolar North Atlantic (Boning et al, 1996; Willebrandt et al., 2001; Myers and Deacu, 2004).

To reduce the problem of salinification of the Labrador Sea, Deacu and Myers (2005) found that the Gent and McWilliams parameterization (Gent and McWilliams, 1990) with a spatially and temporally varying eddy diffusivity coefficient (Visbeck at al., 1997) is a partial remedy, implying that adequate representation of eddy processes improved the representation of salinity in the Labrador Sea. Relating the issue of salinity drift to other aspects of ocean modeling, Treguier et al. (2005) point out that it could be due to excessive salt transports since despite relaxation to surface climatology their study shows salinization of intermediate and upper layers of the

Labrador Sea. From the outline of subpolar gyre circulation mentioned earlier, the excessive salt transport in the Labrador Sea could be tracked to the eastern subpolar gyre by the IC through the NAC in the eastern subpolar gyre since it is the main source of salt transport in this region. Treguier et al. (2005) also suggested the eastern subpolar gyre as a possible source of salinization since in their study all the high resolution models showed a tongue of salty water coming from the eastern part of the basin being advected all around the subpolar gyre as far as the Labrador Current.

A number of other studies also show evidence that the Labrador Sea (hence LSW) is influenced to a large extent by changes in the eastern subpolar gyre (Reynaud et al.,1995; Hatun et al., 2005; Myers et al., 2007; Yashayaev et al., 2007). Reynaud et al. (1995) while determining the summer mean transport and circulation of the northwestern Atlantic found that most of the transport in the Northwestern Atlantic is influenced by the eastern Atlantic. Yashayaev et al. (2007) found that the recent warming and salinification of the mid-depths in the Labrador Sea could be explained by the Irminger basin. A pathway for the warm and salty waters entering the Labrador-Irminger gyre from the east and southeast (eg. SPMW arriving from the Reykjanes Ridge) has been mapped by Yashayaev et al. (2007), indicating that the Irminger-Labrador gyre receives waters from multiple sources and pass their anomalous features not only in eastward direction (LSW) but also westward direction (SPMW).

In this study we want to look at the origin in the salinification of Labrador Sea in an eddy permitting model of the North Atlantic, leading us to investigate the impact of SPMW on LSW properties. To address this question we run two experiments, with significantly different LSW and SPMW formations. This is done using the Gent and McWilliams (1990) parameterization with different formulations for eddy transfer coefficient described in detail in section 4.2. In the results section 4.3 we examine the dispersal of SPMW, its characteristics at Cape Farewell and finally its effect on LSW

in the experiments, and compare the model output with observations. Discussion and conclusions are presented in section 4.4.

4.2 Model Description and Experiments

The model that is used for this study is NEMO (Nucleus for European Models of the Ocean). The NEMO modeling system includes the latest version of the primitive equation, free surface ocean circulation code OPA9 (Madec et al., 1998) coupled to the multilayered sea-ice code LIM (Fichefet and Morales Maqueda, 1997). The configuration of NEMO which is used in this study is NATL4, an eddy-permitting regional configuration with a resolution of 1/4° at the equator having a Mercator horizontal grid, covering the north Atlantic ocean and the Nordic Seas from 20°S to 80°N at Fram Strait (Theetten and Treguier, 2004). The vertical grid has 46 levels with a grid spacing varying from 12 m at the surface to 200 m at the bottom. The bottom topography utilizes the partial cell formulation of Adcroft et al. (1997).

The basic setting of the model is as follows. First, the sea-ice model is driven by atmospheric forcing consisting of surface winds, surface air temperature, humidity, and parameterized longwave and shortwave fluxes. The ice model then supplies surface heat, salt, and momentum fluxes into the ocean surface boundary conditions. The ocean model, in turn, supplies current and heat exchange information to the ice model. The model uses CORE daily heat fluxes and 6-hourly wind forcings (Large and Yeager, 2004). The model is initialised using the Levitus 98-PHC2.1 and Medatlas climatology. Buffer zones are defined at the southern, northern and eastern boundary. The vertical mixing of momentum and tracers is calculated using a second order closure model. The global configuration of NATL4 is called ORCA025 and is described in detail in Barnier et al. (2006). NATL4 is in fact a sub-domain of the global configuration ORCA025, using the same bathymetry, grid and forcing (Barnier

et al., 2005; Theetten and Treguier, 2004).

In this study two NATL4 experiments are chosen, each with significantly different SPMW and LSW formation. Each run was integrated for 14 years. The difference is only in the oceanic lateral subgridscale parameterization based on the Gent and McWilliams (1990) term. Recently Deacu and Myers (2005) found a number of improvements in the hydrography, circulation and pathways of water masses (especially LSW) and eddy activity affecting the Labrador Sea when the Gent and McWilliams (GM, 1990) parameterization was used with the Visbeck et al. (1997) formulation, although models typically have a positive bias in the Labrador Sea salinity (Treguier et al., 2005). GM parameterizes the impact of the unresolved oceanic eddies in the tracer equation by a bolus or an eddy induced velocity. In the original GM (1990) formulation the eddy diffusivity coefficient used to derive the bolus velocities is a constant, whereas when used with the Visbeck et al (1997) method, it becomes spatially and temporally variable. The coefficient is determined based on the length scale of baroclinic region and the Eady growth rate of unstable baroclinic waves (Deacu and Myers, 2005). A summary of the two experiments, one with a constant eddy diffusivity coefficient (PCon) and the other with a variable eddy diffusivity coefficient (PVar) performed in this study is shown in Table 4.1. In PCon the constant value of the eddy transfer coefficient used is $2.74 \times 10^6 \mathrm{cm}^2\mathrm{s}^{-1}$, obtained from the spatial and temporal average of the eddy transfer coefficients calculated in Deacu and Myers (2005).

Methods	Eddy diffusivity coefficient
PCon	$2.74 \times 10^6 \mathrm{cm}^2\mathrm{s}^{-1}$
PVar	variable $((0.5 - 10) \times 10^6 \mathrm{cm}^2\mathrm{s}^{-1})$

Table 4.1: Summary of the experiments performed using the prognostic methods PCon and PVar having constant eddy diffusivity coefficient or a variable eddy diffusivity coefficient respectively.

4.3 Results

4.3.1 NATL4

As mentioned in section 4.1 a major problem with models of the subpolar gyre is salinization and drift (Treguier et al., 2005; Myers and Deacu, 2004). Let's first re-look at this issue in this section with respect to two experiments PCon and PVar. Fig. 4.1 shows the annual mean salinity field of year 14 at 735 m (level 22) in the two experiments and in the Levitus (1982) climatology for comparison. The waters in the Labrador Sea and the eastern subpolar gyre have become saltier. In the Labrador Sea the climatology shows presence of water of salinity lower than 34.90 but PCon has a 34.96 contour encircling the interior of the subpolar gyre. This certainly shows that although NATL4 was initialized with the Levitus (1982) climatology, after 14 years the model has undergone a large drift. For comparison of PVar and PCon a difference plot is shown in Fig. 4.1d. The difference plot in the Labrador Sea shows an anomaly of 0.02 originating in the eastern subpolar gyre and extending westwards into the Labrador Sea, encircling the boundary of the Labrador Sea. The signature of this anomaly is well correlated with the position of the IC discussed in section 4.1 (Cuny et al., 2002) and is further evidence of the impact of eastern subpolar gyre on Labrador Sea. The position of the anomalies further indicate that the salinity differences in PVar and PCon are not being driven by changes in the fresher boundary currents.

To determine if the salinity anomaly is indeed associated with the IC, we look at annual mean salinity averaged in a small box (Fig. 1d) near Cape Farewell (near 60°N). At a depth of 100-700 m, which is associated with SPMW in this region (Myers et al., 2007), PVar is less saltier than PCon by as much as 0.05. Comparing with Levitus (1982) climatology, both experiments show a drift. Nevertheless, the significant difference between PCon and PVar has highlighted an important point whereby we can compare these two experiments to diagnose what is causing Labrador

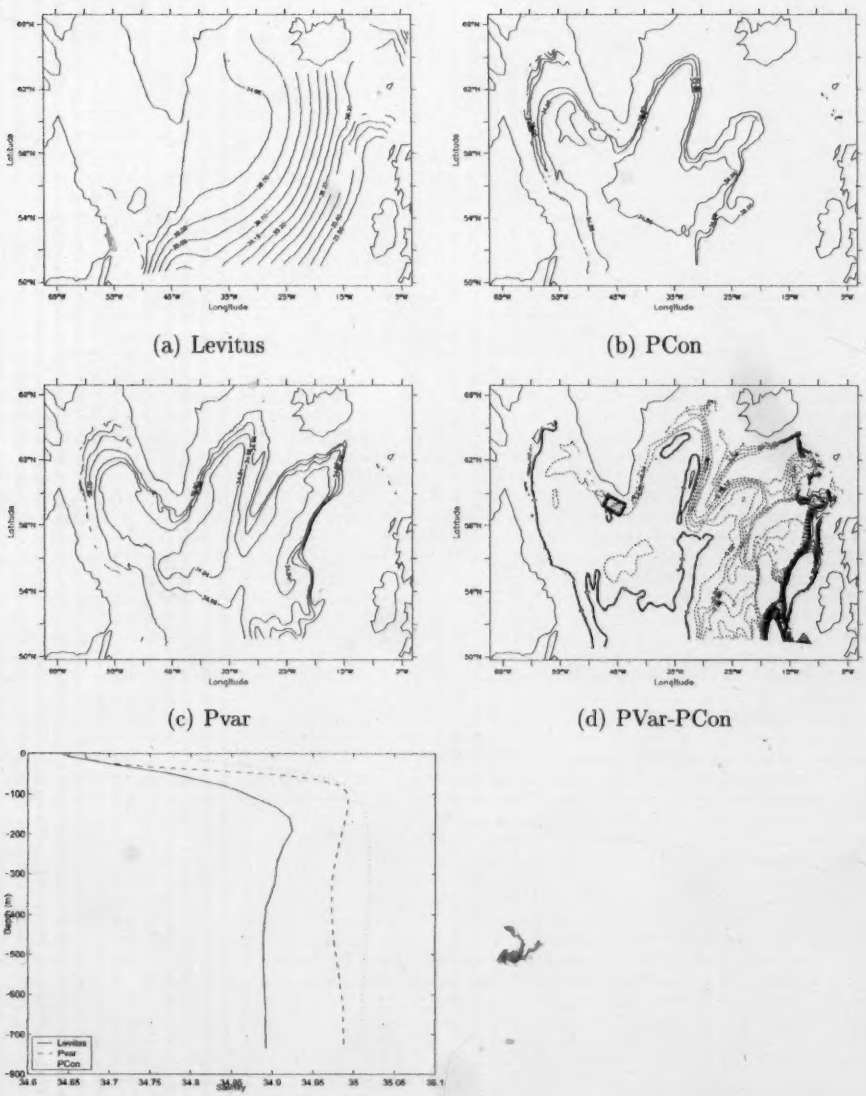

(a) Levitus

(b) PCon

(c) Pvar

(d) PVar-PCon

(e) Salinity Profiles

Figure 4.1: Shown is (a) salinity at 735 m from Levitus (1982) with contour interval 0.05. Also shown is salinity at 735 m (level 22) in (b) PCon (at 0.02 contour interval), (c) PVar (at 0.02 contour interval) and (d) PVar-PCon (at 0.01 contour interval). Panel (e) shows Levitus (1982) climatology, PCon, and PVar salinity profiles averaged over the box outlined in panel (d).

Sea salinification. To examine this question in depth we begin with further analysis of the Labrador Sea: examining the LSW formation (density, volume, salinity, and mixed layer depth) in the two experiments in the next section. It should be noted that as a result of model drift, the properties of LSW and SPMW mentioned in the following sections are different than the traditional definitions of these water masses (eg. Talley and McCartney, 1982; Cuny et al., 2002).

4.3.2 Labrador Sea Water (LSW)

Firstly we calculated the volume of LSW formed during winter by calculating the transformation rates in model year 14. The transformation rates are based on the local volume change over 5 days (since the data in the model are saved as averages every 5 days). The thickness of the isopycnals $\sigma = 27.60 - 27.90$ (which is a representative range of the SPMW (LSW or eastern SPMW) in our simulations) are divided into bins of $\triangle\sigma = 0.01$. The isopycnal thicknesses for each of the bins are then converted into volume by multiplying the thickness with the area of each cell column and then summed over box C (region shown in Fig. 4.2a). The transformation rate for each bin is then simply the difference of the volume between two 5 day intervals divided by the time (which is 5 days). A positive transformation rate then means formation of water in that density bin whereas a negative transformation rate means conversion of water to either higher or lower densities. For each density bin, a winter-time (January-April) average transformation rate was calculated and plotted in Fig. 4.2d for the region defined as box C in Fig. 4.2a.

The positive formation rate in PVar occurs over $\sigma = 27.815 - 27.860$ whereas for PCon it is $\sigma = 27.835 - 27.870$, a shift of density by $\sigma = 0.01 - 0.02$. In this range the total formation rate in PCon is 18.4 Sv while in PVar is 13.3 Sv, a 28% reduction. The maximum transformation rates in PCon is 12 Sv ($\sigma = 27.85$) while in PVar it is 9.5 Sv ($\sigma = 27.84$). The salinity fields averaged over the isopycnals

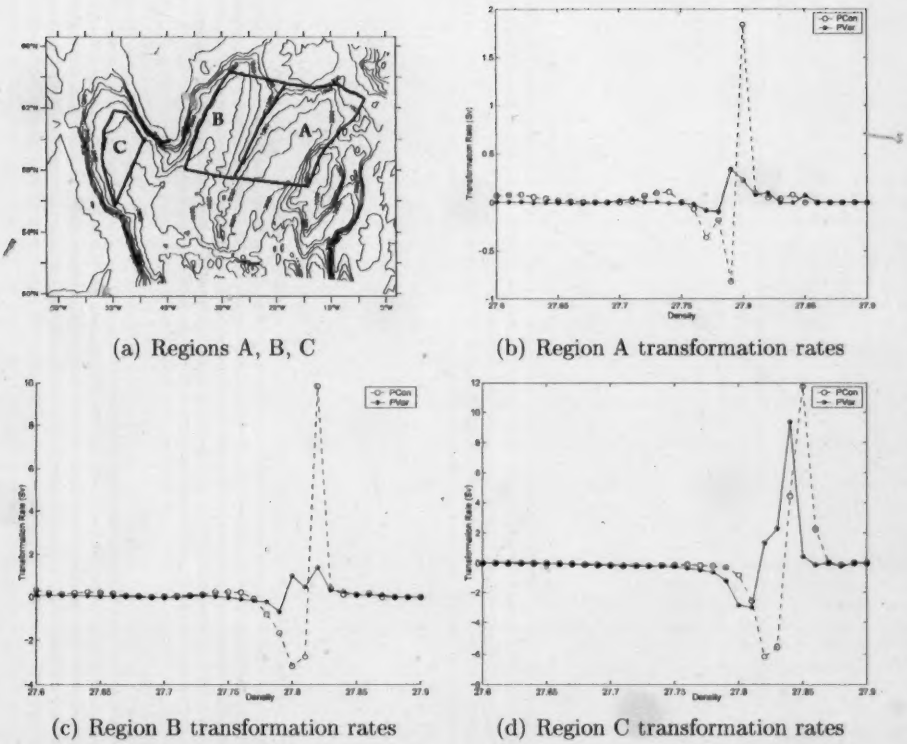

(a) Regions A, B, C

(b) Region A transformation rates

(c) Region B transformation rates

(d) Region C transformation rates

Figure 4.2: Panel (a) shows three boxes A, B and C representing Iceland Basin, Irminger Basin and Labrador Sea respectively which are regions for calculation of transformation rates shown in panels (b), (c) and (d). Panel (a) also shows bathymetry contours plotted at 500 m intervals together with a thick line (near Cape Farewell at the southern tip of Greenland) where vertical crossections are plotted in Figs. 4.4 and 4.5. The winter transformation rate (Sv) plots of PVar (solid line) and PCon (dashed line) obtained from boxes A, B, C are shown in plots (b), (c), and (d) respectively.

at which LSW formation occurs in PVar and PCon are plotted in Fig. 4.3. The salinities of LSW have reduced from 34.94 to 34.93 in the interior Labrador Sea (Fig. 4.3a,b). The difference plot (Fig. 4.3c) clearly shows a general reduction in salinity in the Labrador Sea and along the Labrador Current. The annual mean temperature fields (Figs. 4.3d,e,f) plotted on the same isopycnal range as the salinity field show that the temperatures have reduced by upto 0.3°C in the Labrador Sea. Hence the LSW has become less salty and cooler, yet changes in temperature and salinity are not compensated as seen in the reduction of density in PVar.

The amount of LSW formed is proportional to the depth of convection (Marshall and Schott, 1999), hence we can certainly say that reduced LSW formation should affect the maximum depths of convection. Examining the peak winter mixed layer depths (averages of the last 5 days of end of March) in the Labrador Sea in Fig. 4.4 shows that in PVar maximum mixed layer depths greater than 1750 m, for example, are less widespread than PCon. Further a maxima in the range 2250-2500 m is present only in PCon. Calculations show maximum mixed layer depth in PCon is 2495 m and 2111 m in PVar. Hence this implies that with reduced LSW formation the mixed layer depths have decreased.

LSW is also an important aspect of the global thermohaline circulation (Dickson and Brown, 1994) and hence the meridional overturning circulation (MOC). Changes to LSW would have an impact on the MOC. A portion of the MOC in the subpolar gyre latitudes (about 45°N to 65°N) is shown in Fig. 4.4c for PVar. There is some difference in PVar and PCon (Fig. 4.4d), near 55°N between 1000-2000 m depth the MOC has decreased by upto 1 Sv in PVar compared to PCon, implying the possible impact of decreased LSW formation on the MOC.

As mentioned in section 4.3.1 that there is a link between the Labrador Sea and the eastern subpolar gyre, we next examine water mass properties (salt, heat and volume transports and their corresponding salinity, temperature and velocity profiles in IC)

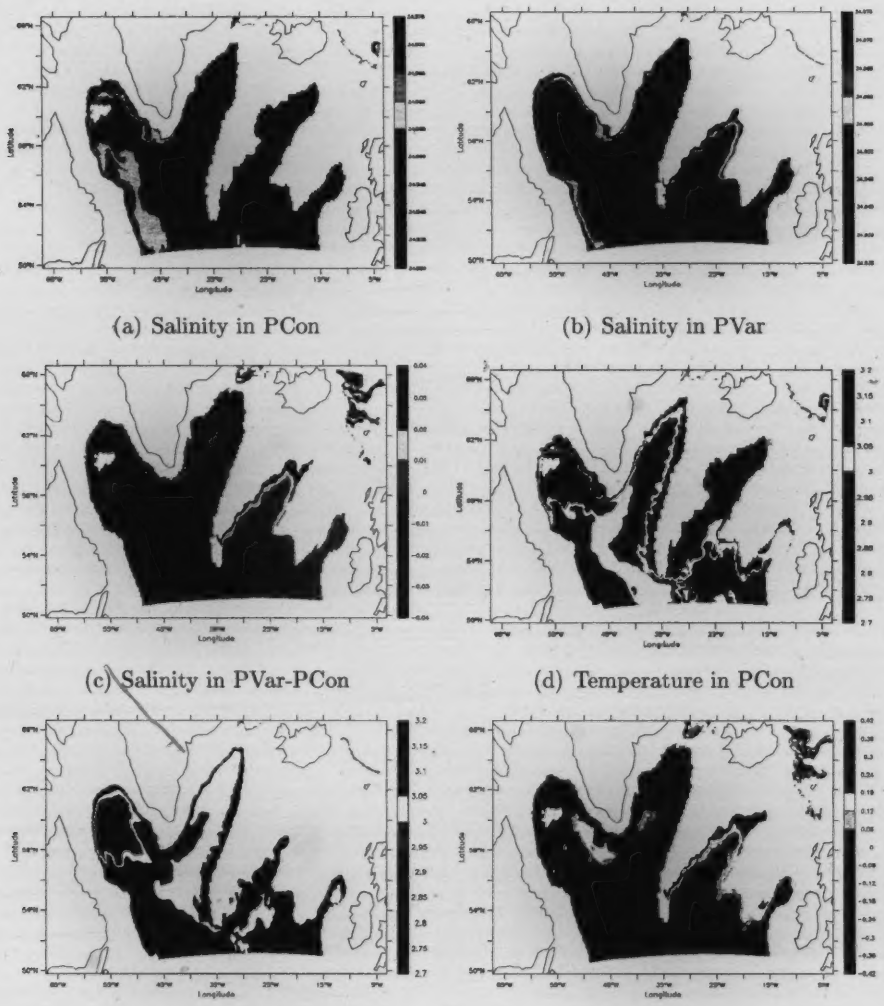

(a) Salinity in PCon

(b) Salinity in PVar

(c) Salinity in PVar-PCon

(d) Temperature in PCon

(e) Temperature in PVar

(f) Temperature in PVar-PCon

Figure 4.3: Labrador Sea Water (LSW) salinity fields at the end of March in (a) PCon averaged over isopycnals $\sigma = 27.835 - 27.870$ (b) PVar averaged over isopycnals $\sigma = 27.815 - 27.860$ and (c) PVar-PCon. Also shown are temperature fields at the end of March in (d) PCon averaged over isopycnals $\sigma = 27.835 - 27.870$ (e) PVar averaged over isopycnals $\sigma = 27.815 - 27.860$ and (f) PVar-PCon.

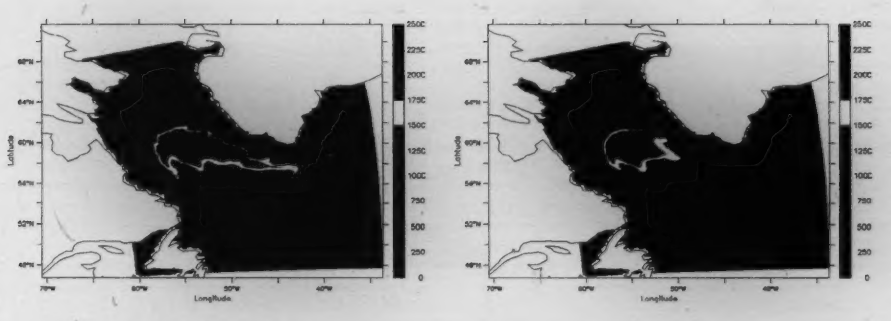

(a) MLD in PCon

(b) MLD in PVar

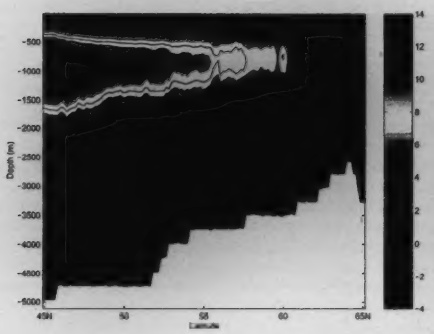

(c) MOC in PVar

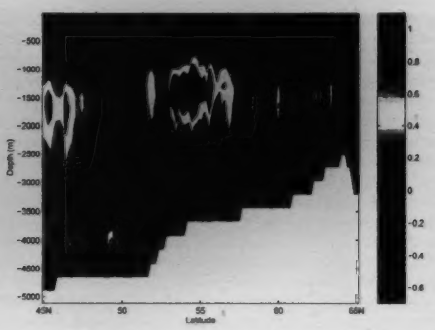

(d) MOC in PVar-PCon

Figure 4.4: Mixed layer depth (MLD; m) at the end of March in (a) PCon and (b) PVar. Also shown is meridional overturning circulation (Sv) over the subpolar gyre in (c) PVar and (d) PVar-PCon.

near Cape Farewell (at 60°N, Fig. 4.2a) which provides an entry point of SPMW into the Labrador Sea and also has a collection of historical data for comparison. Is it the rate of water formation or the shift in density in the eastern subpolar gyre which is playing a greater role? This can be answered by examining the changes in volume and salt transport magnitudes at Cape Farewell.

4.3.3 Irminger Current (IC)

As in the Labrador Sea, there is a reduction in salinity at Cape Farewell (Figs. 4.5a,b,c). Salinity of the IC core in PVar (34.99, Fig. 4.5b) is lower than in PCon (35.06, Fig. 4.5a). The difference plot (Fig. 4.5c) further shows that the IC has become fresher (by about 0.07) at about 500 m depth near 46.6°W. The velocity magnitudes at this location have also reduced by about 0.10 m/s (Fig. 4.5c). The annual mean salt transport, presented pointwise (i.e. given as the transport in each individual grid cell) referenced to 34.8 (Figs. 4.5d,e,f) shows that the salt transports have decreased with the decrease in salinity, especially the difference plot (Fig. 4.5e) which shows that in the IC core (near 500 m depth and 46.4°W) the salt transport is locally less by about 2 mSv. The mean annual volume transports (Figs. 4.5d,e,f) also show a general reduction. The difference plot (Fig. 4.5f) shows that the volume transport in PVar is locally less by about 150 mSv (30 % reduction) in the IC core. Integrating the volume transport over SPMW levels (200-700 m; Myers et al., 2007) yields 29.39 Sv in PCon and 29.36 Sv in Pvar (difference of 30 mSv) whereas the salt transports yield 175 mSv (PCon) and 160 mSv (PVar, difference of 15 mSv). The annual mean temperature and heat transport fields (Fig. 4.6) also confirm the propagation of Cape Farewell properties to Labrador Sea: temperatures are cooler (by 0.2°C) and heat transports have reduced (by about 0.4×10^{13} W in the IC core). The annual mean values of IC properties at Cape Farewell from our PVar simulation (while taking into consideration the drift in our model) are in agreement with observations:

IC generally has temperatures and salinities within the range 3.5 – 6°C and 34.88-35.10 respectively (Cuny et al., 2002; Clarke, 1984; Reynaud et al., 1995; Ribergaard, 2006). Since the IC has its origin in the eastern subpolar gyre, we next examine the SPMW in the eastern subpolar gyre.

4.3.4 Subpolar Mode Water (SPMW)

Transformation rates are calculated for the eastern subpolar gyre in two regions, one east of Reykjanes Ridge (Iceland Basin: shown as box A in Fig. 4.2a) and the other west of Reykjanes Ridge (Irminger Basin: shown as box B in Fig. 4.2a). For the Iceland Basin in both experiments, peak positive transformation rate occurs over a small density range in both PVar and PCon: in PVar (Fig. 4.2b) at $\sigma = 27.79$ (0.3 Sv) whereas in PCon at $\sigma = 27.80$ (1.8 Sv), a difference in isopycnal of $\sigma = 0.01$. The total positive formation rate in PCon is 2.1 Sv and is higher than 0.7 Sv produced in PVar (67% reduction). Thus PVar has less mode water formation, and at a lower density. A plot of the peak winter (average of the last 5 days of end of March) salinity fields (Fig. 4.7) on the isopycnal range $\sigma = 27.67 - 27.75$ (which is a typical range for SPMW formation in both experiments as depicted in Fig. 4.2b) shows PCon salinities (35.00-35.25; Fig. 4.7a) being slightly higher than PVar (34.90-35.20; Fig. 4.7b). Fig 4.7c shows that the salinity differences are as large as -0.15. The peak winter temperature fields plotted on the same isopycnal range indicates that temperatures have reduced from $4.4 - 6^{o}$C (Fig. 4.7d) to $4.0 - 5.6^{o}$C (Fig. 4.7e) with differences of upto -1^{o}C (Fig. 4.7f).

In order to examine the water formation properties propagated towards the west of the Reykjanes Ridge by the IC, the formation rates were calculated in the Irminger Basin in box B (shown in Fig. 4.2a). The peak positive transformation rate in PVar (Fig. 4.2c) is 1.5 Sv whereas in PCon is 9.9 Sv. In relation to their peak transformation rate counterparts eastwards of the Reykjanes Ridge, we can see that

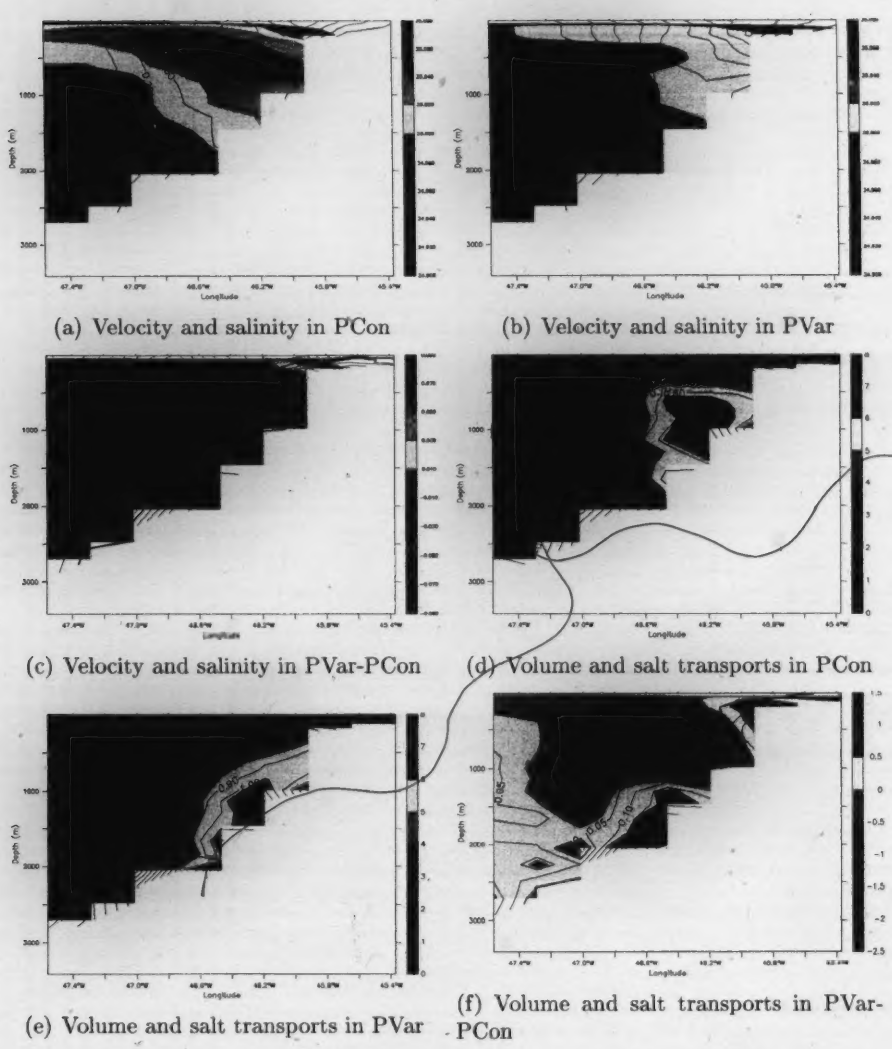

(a) Velocity and salinity in PCon

(b) Velocity and salinity in PVar

(c) Velocity and salinity in PVar-PCon

(d) Volume and salt transports in PCon

(e) Volume and salt transports in PVar

(f) Volume and salt transports in PVar-PCon

Figure 4.5: Annual mean 60°N section (Cape Farewell) of velocity magnitude (contours; m/s) superimposed on salinity (shading) in (a) PCon, (b) PVar, (c) PVar-PCon. Dashed contours denote negative values (reduced velocity magnitude in panel (c)) and solid contours positive values (increased velocity magnitude in panel (c)), labelled from 0.1 m/s to 0.9 m/s in PVar and PCon at intervals of 0.1 m/s and PVar-PCon at contour intervals of 0.01 m/s. At the salinity core, in PCon a salinity maxima of over 35.057 is shown in contrast to PVar maxima of over 34.988. Also shown are annual mean volume transport magnitude (contours; Sv) superimposed on salt transport referenced to 34.8 (shading; mSv) in (d) PCon (e) PVar (f) PVar-PCon (contour intervals of 0.01 Sv). PCon and PVar are at contour intervals of 0.1 Sv. Dashed contours denote negative values (reduced volume transport magnitude in panel (e)) and solid contours positive values (increased volume transport magnitude in panel (e)).

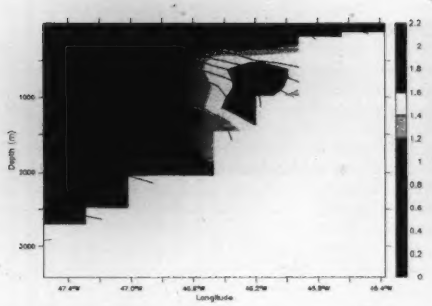

(a) Heat transport and temperature in PCon

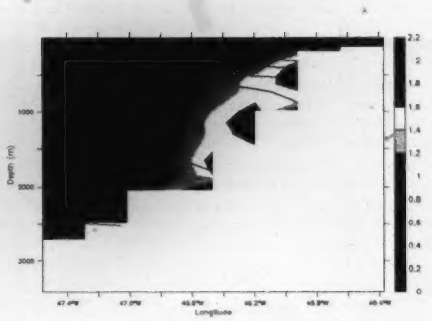

(b) Heat transport and temperature in PVar

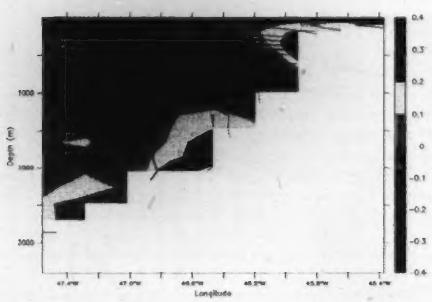

(c) Heat transport and temperature in PVar-PCon

Figure 4.6: Annual mean 60°N section (Cape Farewell) of heat transport magnitude ($\times 10^{13}$W, shading) superimposed on temperature (contours; °C) in (a) PCon (contour intervals of 0.2°C) (b) PVar (contour intervals of 0.2°C) (c) PVar-PCon (contour intervals of 0.1°C). Dashed contours denote negative values (reduced temperature in panel (c)) and solid contours positive values (increased temperature in panel (c)).

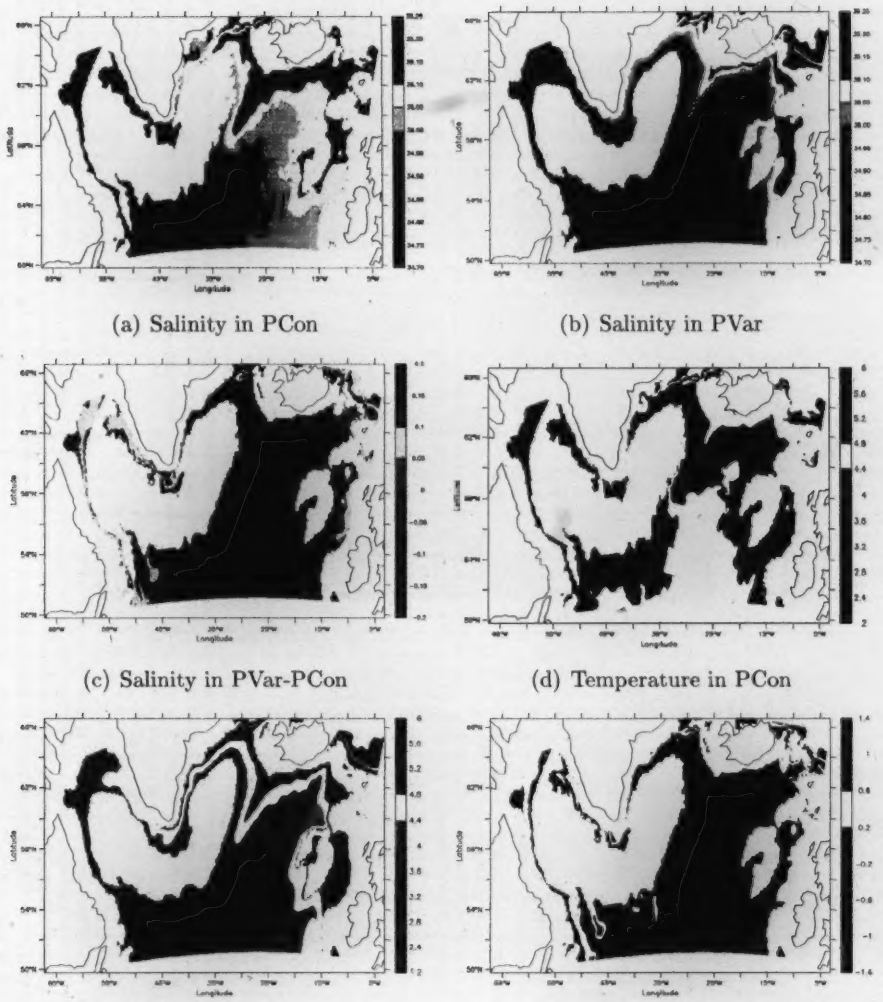

(a) Salinity in PCon

(b) Salinity in PVar

(c) Salinity in PVar-PCon

(d) Temperature in PCon

(e) Temperature in PVar

(f) Temperature in PVar-PCon

Figure 4.7: Salinity fields at the end of March averaged over isopycnals $\sigma = 27.67 - 27.75$ in (a) PCon (b) PVar (c) PVar-PCon. Also shown are temperature fields at the end of March averaged over isopycnals $\sigma = 27.67 - 27.75$ in (d) PCon (e) PVar (f) PVar-PCon.

the density at which Irminger Basin peak water transformation occurs has shifted up by about $\sigma = 0.02$ consistent with the fact that SPMW density increases westwards in the subpolar gyre (Read, 2001). The total positive formation rate in PCon is 10.2 Sv on isopycnal $\sigma = 27.815 - 27.85$ and is slightly higher than 9.2 Sv produced in PVar on isopycnal $\sigma = 27.80 - 27.85$ (10% reduction).

4.3.5 Validation of results

A summary of the comparison of observations with PVar and PCon is given in Table 4.2. The table depicts that PVar-PCon differences in Labrador Sea winter maximum mixed layer depths, LSW maximum formation rates and Irminger Current salinity are significant at 48%, 69% and 40% respectively. This suggests that there is a significant change between the two simulations (PVar and PCon) in the eastern subpolar gyre that eventually lead to a significant change in properties at Cape Farewell and Labrador Sea.

	Observation	**PVar**	**PCon**	**PVar-PCon**
Winter maximum mixed layer depth (M) in m	Lazier at al. (2002) (years: 1987-1999) range: 700-2300 m $\overline{M}$ = 1691m, 1σ = 506m $\overline{\triangle M}$ = 402m, $1\sigma\left(\overline{\triangle M}\right)$ = 282m	2111 m	2495 m	384 m PVar-PCon error (384 m) is significant at 48% significant level. PVar (2111 m) is closer to the observational mean (1691 m) and within observational limits.
LSW Maximum Formation Rate (T) **in Sv**	Haine et al. (2006) 1.3-12.7 Sv $\overline{T}$ = 4.8Sv, 1σ = 2.7Sv $\overline{\triangle T}$ = 2.2Sv, $1\sigma\left(\overline{\triangle T}\right)$ = 1.6Sv	9 Sv	12 Sv	3 Sv PVar-PCon error (3Sv) is significant at 69% confidence level. PVar (9 Sv) is closer to the observational mean (4.8 Sv).
Cape Farewell salinity (S)	Cuny et al. (2002) (years: 1990-1999) range: 34.88-34.98 $\overline{\triangle S}$ = 0.08, $1\sigma\left(\overline{\triangle S}\right)$ = 0.04	34.99	35.06	0.07 PVar-PCon error (0.07) is significant at 40% significant level. Inspite of model drift, PVar (34.99) is closer to the observational range than PCon.

Table 4.2: Summary of the validation of results.

4.4 Discussion and Conclusion

Two experiments with significantly different formations of Labrador Sea Water (LSW: density, volume, salinity and mixed layer depth) are examined in the NEMO coupled ocean-sea ice model to determine the role of Subpolar Mode Water (SPMW) on LSW, which subsequently suggests an explanation for the origin of salinization in eddy permitting models of the subpolar North Atlantic. The only difference between these experiments is that one (PCon) uses a constant eddy diffusivity in the Gent and McWilliams formulation (Gent and McWilliams, 1990) while the other (PVar) utilises a spatially and temporally varying eddy diffusivity coefficient (Visbeck et al., 1997). In PVar there is reduced SPMW formation in the eastern subpolar gyre due to a lower eddy diffusivity coefficient in this region compared to PCon. The aim of this study is to find the impact of these changes on SPMW dispersal, and its subsequent effect on the Labrador Sea Water (LSW) formation and its dispersal. Hence the results of this study are important because apart from showing a cause for salinization of Labrador Sea, we show another way to improve LSW in an eddy-resolving ocean general circulation model.

In summary, in our study we observed that the SPMW density, formation rate, and salinity decreased respectively by 0.01, 67%, and 0.15 between our PVar and PCon experiments. This led to a subsequent decrease in SPMW salt and volume transports respectively by about 2 mSv and 150 mSv at Cape Farewell. With reduced amounts of less saline SPMW available for LSW formation, the LSW density, formation rate, salinity, and maximum mixed layers depths were respectively reduced by 0.01-0.02, 28%, 0.04 and 384 m. Hence we conclude that changes in SPMW are propagated into LSW and affect its formation.

Our modeling study has demonstrated the importance of SPMW on LSW formation. A shift towards lighter and reduced SPMW formation in the eastern subpolar gyre leads to reduced salt and volume transports of SPMW at Cape Farewell and sub-

sequently the LSW became less saline with a reduced formation rate. This scenario has important implications for LSW and the rest of the subpolar gyre. A number of recent observational studies indicate large variabilities in Irminger Water (IW; Myers et al., 2007) and Reykjanes Ridge Mode Water (RRMW; Thierry and Mercier, 2007) which are part of the SPMW. At Cape Farewell using data from International Council for the Exploration of the Sea (ICES) Myers et al. (2007) found that for the period 1984-2005 the IW transports are 3.8± 0.9 Sv of liquid water, 7.5± 1.7 $\times 10^{13}$ J/s of heat, and 8.5± 1.8 mSv of freshwater referenced to 35, implying a large variability in transports. A significant variability in the salinity, size and position of the IW core over time were also found to exist (Myers et al., 2007) and being driven to a large extent by the North Atlantic Oscillation (NAO). The RRMW observations by Thierry and Mercier (2007) using CTD data from 1990-2006 have also observed a large variability in temperature and salinity fields in this form of SPMW. The temperature and salinity increased by 1.41°C and 0.11 respectively in 1996, with a simultaneous drop to a large negative NAO index in the same year which never returned to positive again (Theirry and Mercier; 2007). Hence the NAO driven variabilities in RRMW (Theirry and Mercier; 2007) and IW (Myers et al., 2007) imply that the SPMW is in large forced by the NAO. Since in this study we have shown that SPMW affects LSW formation, we have another way that NAO helps drives changes in LSW, besides its well known direct input through varying heat fluxes (Hurrell et al., 2003; Myers et al., 2007; Thierry and Mercier, 2007).

4.5 Acknowledgment

This work is supported by the Natural Sciences and Engineering Research Council of Canada, & CFCAS grants awarded to PGM (CLIVAR & GOAPP).

Bibliography

[1] Adcroft, A., Hill, C., Marshall, J., 1997. Representation of topography by shaved cells in a height coordinate ocean model, Monthly Weather Review, 125, 2293-2315.

[2] Barnier, B., Penduff, T., Molines, J.M., Treguier, A.M., Theetten, S., Madec, S. (2005) The ocean circulation in the North Atlantic and the Nordic Seas: variability, processes and interactions with the global ocean, Report of activity 2003-2004.

[3] Böning CW, Scheinert M, Dengg J, Biastoch A, Funk A (2006) Decadal variability of subpolar gyre transport and its reverberation in the North Atlantic overturning, Geophysical Research Letters, 33, doi:10.1029/2006GL026906.

[4] Böning CW, Bryan FO, Holland WR and Doschler R (1996) Deep water formation and meridional overturning in a high resolution model of the North Atlantic, Journal of Physical Oceanography, 26, 1141-1164.

[5] Cuny, J., P.B. Rhines, P.P. Niiler, and S. Bacon (2002), Labrador Sea boundary currents and the fate of Irminger Sea Water, Journal of Physical Oceanography, 32, 627-647.

[6] Deacu, D., and Myers, P.G., 2005. Effect of a variable eddy transfer coefficient in an eddy-permitting model of the Sub-Polar North Atlantic. Journal of Physical Oceanography 35, 289-307.

[7] Dickson RR, and Brown J, (1994) The production of North Atlantic Deep Water: sources, rates, pathways. Journal of Geophysical Research, 99 (C6), 12319-12341.

[8] Eden C, Böning CW (2002) Sources of eddy kinetic energy in the Labrador Sea, Journal of Physical Oceanography 32, 3346-3363.

[9] Fichefet T, Morales Maqueda MA (1997) Sensitivity of a global sea ice model to the treatment of ice thermodynamics and dynamics, Journal of Geophysical Research, 102, 12609-12646.

[10] Gent, P.R., McWilliams, J.C., 1990. Isopycnal mixing in ocean circulation models. Jounal of Physical Oceanography 20, 150-155.

[11] Haine TWN, Richards KJ, and Jia Y (2003) Chlorofluorocarbon constraints on North Atlantic ocean ventilation, Journal of Physical Oceanography, 33, 1798-1814.

[12] Hatun, H., A.B. Sando, H. Drange, B. Hansen, and H. Valdimarsson (2005), Influence of the Atlantic subpolar gyre on the thermohaline circulation, Science, 309, 1841-1844.

[13] Hurrell, JW, Kushnir Y, Ottersen G, Visbeck M (Eds) (2003), The North Atlantic Oscillation: Climatic Significance and Environmental Impact, Geophysical Monogr. Ser., vol 134, 279 pp., AGU, Washington, D.C.

[14] Large W, and Yeager S, (2004) Diurnal to decadal global forcing for ocean and sea-ice models: the data sets and flux climatologies. NCAR technical note: NCAR/TN-460+STR. CGD division of the National Center of Atmospheric Research.

[15] Levitus, S (1982) Climatological atlas of the world ocean. Tech Rep 13, US Department of Commerce, National Oceanographic and Atmospheric Administration.

[16] Madec, G., Delecluse, P., Imbard, M., Levy, C. (1998) General circulation model reference manual, Notes de l'IPSL, Universite P. et M. Curie, B102 T15-ES, 4 place Jussie, Paris cedex 5, N°11, 91p.

[17] Marshall J, Schott F (1999) Open-ocean convection: observations, theory and models, Review of Geophysics, 37, 1-64.

[18] McCartney MS, and Talley LD, (1982) The Subpolar Mode Water of the North Atlantic Ocean, Journal of physical oceanography, 12, 1169-1188.

[19] Myers, P.G., and Deacu, D., 2004. Labrador sea freshwater content in a model with a partial cell topographic representation. Ocean modelling 6, pp. 359-377.

[20] Myers PG, Kulan N, Ribergaard MH, (2007) Irminger Water variability in the West Greenland Current, Geophysical Research Letters, 34, doi:10.1029/2007GL030419.

[21] Reynaud, T.H., A.J. Weaver, and R.J. Greatbatch (1995), Summer mean circulation of the northwestern Atlantic Ocean, Journal of Geophysical Research, 100, 779-816.

[22] Talley, L.D. and M.S. McCartney (1982) Distribution and circulation of Labrador Sea Water, Journal of Physical Oceanography, 12, 1189-1205.

[23] Theetten, S. and A.M. Treguier, A.M., Validation and analysis of the first NATL4 run of the DRAKKAR project. Laboratoire de Physique des Oceans, CNRS-Ifremer-UBO, Brest, France, Internal report DOPS/LPO 05-01, 2004.

[24] Theirry V, and Mercier H (2007) Rapid changes in the properties of the Reykjanes Ridge Mode Water over 1990-2006, submitted to Journal of Geophysical Research.

[25] Treguier, A.M., Theetten, S., Chassignet, E.P., Penduff, T., Smith, R., Talley, L., Beismann, J.O., Boning, C., 2005. The North Atlantic subpolar gyre in four high resolution models. Journal of Physical Oceanography 35, 757-774.

[26] Visbeck, M., Marshall, J., Haine, T., Spall, M., 1997. Specifications of eddy transfer coefficients in coarse-resolution ocean models, Journal of Physical Oceanography, 16, 680-693.

[27] Willebrandt J, Barnier B, Böning C, Dieterich C, Killworth PD, Le Provost C, Jia Y, Molines JM, New AL (2001) Circulation characteristics in three eddy permitting models of the North Atlantic, Progress in oceanography, 48, Pergamon, 123-161.

[28] Yashayaev IM, Bersch M, van Aken HM (2007) Spreading of the Labrador Sea Water to the Irminger Sea and Iceland Basin, Geophysical Research Letters, 34, doi:10.1029/2006GL028999.

Chapter 5

Sea Ice representation in the NATL4 configuration of NEMO

5.1 Introduction

Sea ice is an important component of the coupled ocean-ice-atmosphere system that acts as an insulating layer between the ocean and the atmosphere and in the process creates a large difference in the surface heat fluxes between ice-covered and non-ice covered areas of the ocean (Melia, 2002). In the North Atlantic, during winter, sea ice is found along the eastern coasts of Canada, northwestern parts of the Labrador Sea, and the eastern and western coasts of Greenland, Baffin Bay, and the Greenland-Iceland-Norwegian (GIN) seas. Having a strong seasonal variability, maximum sea ice extent in the North Atlantic is found during March whereas a minima is present during September (Comiso et al., 2005).

Sea ice can be characterised by a number of important parameters three of which are: thickness, concentration and extent. Sea ice thickness is an important parameter that determines the volume of fresh water stored in a given ice pack area (Timmermann et al., 2004). Through its impact on heat exchange at the bottom and top

surfaces of sea ice, it eventually has an impact on the ice-ocean-atmosphere heat exchange (Fichefet and Morales Maqueda, 1997). Though a very important parameter, observations of sea ice thickness data are limited in the North Atlantic (especially along eastern Canadian coasts) to sparse land based Canadian Ice Service Stations (CIS; http://ice-glaces.ec.gc.ca), although in the Arctic and along the Eastern Greenland coast limited upward looking sonar data also exist (Gerdes and Kobe, 2007). Sea ice concentration is another important parameter. Lower sea ice concentration leads to more shortwave absorption, which leads to enhanced ice melt and further decrease in concentration (Ogura, 2004). In sea ice models (Fichefet and Morales Maqueda, 1997) concentration is a parameter used to determine the lateral growth and decay of sea ice unlike thickness which is used to determine vertical growth and decay. Another important parameter to characterise sea ice is its extent. It is defined as the sum of sea ice areas with concentration greater than 15% (Comiso 2006; Melia, 2002; Timmermann et al., 2005). It provides information about available ocean surface area that is thermodynamically conditioned for ice formation during the growth season.

A few modelling studies have been performed to analyze the climatological representation of sea ice in the sub-polar North Atlantic in coupled ocean-sea ice models (eg. Melia, 2002; Timmermann et al., 2005). Melia (2002) devised a new sea ice model and coupled it with the ocean model OPA 8.0 (Océan Parallélisé; Madec et al., 1998) that was used to study the sea ice concentration and thickness of the North Atlantic. Reasonable agreements between model and observation thickness and concentration are seen. However, sea ice is underestimated during March in the Labrador Sea and Denmark Strait and during September in GIN seas (Melia, 2002). In another study, Timmermann et al. (2005) used a 2^o global configuration of OPA 8.2 coupled with Louvain-la-Neuve (LIM) sea ice model (Fichefet and Morales Maqueda, 1997). This study realistically captured the annual cycle of sea ice growth and decay with ice extent, thickness and drift in close agreement with observations. However, in sum-

mer the model overestimated sea ice concentration in the Baffin Bay. In winter the model also overestimated ice concentration in the GIN Seas and along the northeastern Greenland coast. As a result sea ice was completely missing in this study along the southeastern Greenland coast in winter (Timmermann et al., 2005).

The general spatial characteristics of sea ice has been reasonably captured in coupled ocean-sea ice models (Melia, 2002; Timmermann et al., 2005) but fine details are still missing as mentioned above. Hence we decided to re-examine the representation of sea ice in the North Atlantic using the OPA 9.0 ocean model (resolution of $1/4^{o}$) coupled to the LIM sea ice model. In order to better resolve the North Atlantic hydrography we have also implemented an improved ocean subgridscale parameterization and an ocean data assimilation scheme in this model. Sensitivity studies are also performed with these new additions to the model. Further, previous studies have not done regional studies and references were made to hemispheric comparisons or the Arctic as a whole. We thus want to re-examine the North Atlantic sea ice covered areas more closely in terms of regionally dividing it into the Eastern Greenland coast, Labrador coast, Western Greenland (Northwestern Labrador Sea including Baffin Bay and Hudson Bay) and Newfoundland Basin.

In this paper, section 5.2 discusses the model and the methods that will be used for sensitivity analysis. The seasonal cycles of sea ice concentration, sea ice thickness, and sea ice extent are discussed in section 5.3. Section 5.4 presents results from the sensitivity analysis. A brief summary and discussion are presented in section 5.5.

5.2 Model and Method

The model that is used for this study is NEMO version 1.6 (Nucleus for European Models of the Ocean). The NEMO modelling system includes the latest version of the primitive equation, free surface ocean circulation code OPA 9.0 (Madec et al., 1998)

coupled to the multilayered sea-ice code LIM (Fichefet and Morales Maqueda, 1997; Goosse and Fichefet, 1999). The configuration of NEMO which is used in this study is NATL4, an eddy-permitting regional configuration with a resolution of 1/4° at the equator having a Mercator horizontal grid, covering the North Atlantic ocean and sea ice from 20°S to 80°N at Fram Strait (Theetten and Treguier, 2004). The global configuration of NATL4 is called ORCA025 and is described in detail in Barnier et al. (2006). NATL4 is in fact a sub-domain of the global configuration ORCA025, using the same bathymetry, grid and forcing (Barnier et al., 2005; Theetten and Treguier, 2004). The basic setting of the model is as follows. First, the sea-ice model is driven by atmospheric forcing consisting of surface winds, surface air temperature, humidity, and parameterized longwave and shortwave fluxes. The ice model then supplies surface heat, salt, and momentum fluxes into the ocean surface boundary conditions. The ocean model, in turn, supplies current and heat exchange information to the ice model.

The ocean component of NATL4 (Madec et al., 1998) has 46 vertical grid levels with a grid spacing varying from 12 m at the surface to 200 m at the bottom. The bottom topography utilizes the partial cell formulation of Adcroft et al. (1997). It uses CORE daily heat fluxes and 6-hourly wind forcings (Large and Yeager, 2004). It is initialised using the Levitus 98-PHC2.1 and Medatlas climatology. Buffer zones are defined at the southern, northern and eastern boundary.

The sea ice model LIM is a dynamic-thermodynamic model. The thermodynamic part of LIM has a layer for snow and two layers for sea ice with their internal temperatures being determined by a one dimensional heat diffusion equation. For vertical growth and decay of sea ice, the top and bottom surfaces of the ice-snow system heat flux budgets are taken into account. For lateral growth and decay of leads and polynyas, a concentration variable defined as the fraction of the grid cell area covered by ice is utilized. Ice dynamics is treated basically as in Hibler (1979), where the ice

is assumed to follow a viscous-plastic constitutive law in a two-dimensional continuun in dynamical interaction with the atmosphere and the ocean.

A subgridscale eddy parameterization used is the Gent and McWilliams parameterization (GM, 1990), together with the Visbeck et al. (1997) variable eddy difusivity coefficient. Recently Deacu and Myers (2005) found a number of improvements in the hydrography, circulation and pathways of water masses and eddy activity affecting the Labrador Sea when the GM parameterization was used with the Visbeck et al. (1997) formulation. The GM parameterizes the impact of the unresolved oceanic eddies in the tracer equation by a bolus or an eddy induced velocity. In the original GM formulation the eddy diffusivity coefficient used to derive the bolus velocities is a constant, whereas when used with the Visbeck et al. (1997) method, it becomes spatially and temporally variable. In this study it is obtained from the length scale of the baroclinic region and the Eady growth rate of unstable baroclinic waves (Visbeck et al., 1997). In section 5.4.2, to examine the sensitivity to eddy representation, two prognostic runs are made: both use the GM parameterization but one uses a constant eddy diffusivity coefficient (PCon) whereas the other utilises the variable eddy diffusivity coefficient (PVar). In PCon the constant value of the eddy transfer coefficient used is $2.74 \times 10^6 \mathrm{cm}^2\mathrm{s}^{-1}$, obtained from the spatial and temporal average of the eddy transfer coefficients calculated in Deacu and Myers (2005).

A number of ocean models (eg. Sarmiento and Bryan, 1982) use restoring terms that directly constrain temperature and salinity to climatolgy as a form of data assimilation. An indirect method of restoring temperature and salinity is the semi-diagnostic method (Zhai et al., 2004) that allows the salinity and temperature fields to evolve prognostically. The semidiagnostic method makes adjustments by replacing the density field in the hydrostatic equation by a linear combination of model computed and climatological density. We use the Levitus (1982) for our climatological estimates of our temperature, salinity and density. In order to determine the sensitivity of sea ice

to this ocean data assimilation scheme, it is implemented in the ocean component of NEMO. A summary of the experiments performed in this study is given in Table 5.1.

Method		Eddy transfer coefficient
Prognostic	PCon	$2.74 \times 10^6 \text{cm}^2\text{s}^{-1}$
	PVar	variable $((0.5 - 10) \times 10^6 \text{cm}^2\text{s}^{-1})$
Semi-diagnostic	SDVar	variable $((0.5 - 10) \times 10^6 \text{cm}^2\text{s}^{-1})$

Table 5.1: Summary of the experiments performed with variable eddy diffusivity coefficients: prognostic (PVar) and semi-diagnostic (SDVar) experiments, and with constant eddy diffusivity coefficient: prognostic (PCon).

5.3 Mean Ice Fields

The NATL4 configuration of the NEMO model is integrated for 14 years in a perpetual year mode using a version which has both the variable eddy diffusivity coefficient and the semi-diagnostic oceanic assimilation (SDVar). The resulting mean seasonal sea ice concentration, thickness and extent are examined in this section.

5.3.1 Sea ice concentration

Simulated seasonal sea ice concentrations of monthly averages in September, December, March and June together with corresponding satellite observations from years 1970-1998 in Walsh (1978) and the Canadian Ice Service (CIS) monthly ice concentration archive charts are shown in Figs. 1,2. CIS data are found at http://ice-glaces.ec.gc.ca/ and is a composite of shore, ship and aircraft based visual observations and remote sensing devices, with additional analysis done by forecasters. Walsh (1978) observations are low resolution ($1^o \times 1^o$) satelite data and as a result are not as detailed as CIS data. However, due to its larger spatial coverage (especially along Eastern Greenland coast where there is no CIS data), Walsh (1978) data is also used in this study for comparison.

In the GIN seas a comparison between Walsh (1978) data and SDVar (Figs.

5.1,5.2) shows generally a similarity in the sea ice concentration seasonal cycle spatial patterns over all the months, except for some differences that could be attributed to the low resolution of Walsh (1978) data. In September (Fig. 5.1a) along the north-eastern Greenland coast a maxima of over 60% is observed (in Walsh, 1978) which gradually reduces to about 0% near 72°N at the Eastern Greenland coast, while SD-Var concentrations (Fig. 5.1b) of 90% gradually decrease to 0% near 75°N at the Eastern Greenland coast. SDVar is generally of lower concentration overall especially along the sea ice edges in the GIN seas (Fig. 5.1c). In December, the 90% contour in SDVar (Fig. 5.1f) is further south to about 70°N at the Eastern Greenland coast and has also protruded deeper into the GIN seas, while the Walsh (1978) 90% (Fig. 5.1d) contour is narrower and spreads south to about 75°N. As a result, in December (Fig. 5.1g) the sea ice concentrations appear to be larger in SDVar especially along the sea ice edges. By winter (March, Fig. 5.2c) in the Denmark Strait (between Greenland and Iceland) SDVar concentration is generally over 90% with the 90% contour spreading all the way down to 65°N, while in Walsh (1978) the 90% contour remains near 73°N, resulting in a large (over 80%; Fig. 5.2d) concentration difference along the ice edges just north of Iceland in the GIN seas. By June (Fig. 5.2g) the concentration pattern is more irregular in SDVar in the Denmark Strait, has decreased and retreated northwards along the East Greenland coast, while the 0% contour is still present around the southern tip of Greenland in the Walsh (1978) data.

In all the other regions consisting of Baffin Bay, Davis Strait, Foxe Basin, Hudson Bay, and eastern Labrador coast (except GIN seas and Eastern Greenland coast) reasonable agreements exist between CIS and SDVar seasonal cycles of sea ice concentrations. In September some sea ice is present in Foxe Basin while the rest of the Eastern Canadian and the Western Greenland coasts are ice free in Walsh (1978) data (Fig. 5.1a). In SDVar (Figs. 5.1b,c), however, there is some ice still present in Baffin Bay in addition to Foxe Basin similar to CIS data (not shown; only Labrador coast

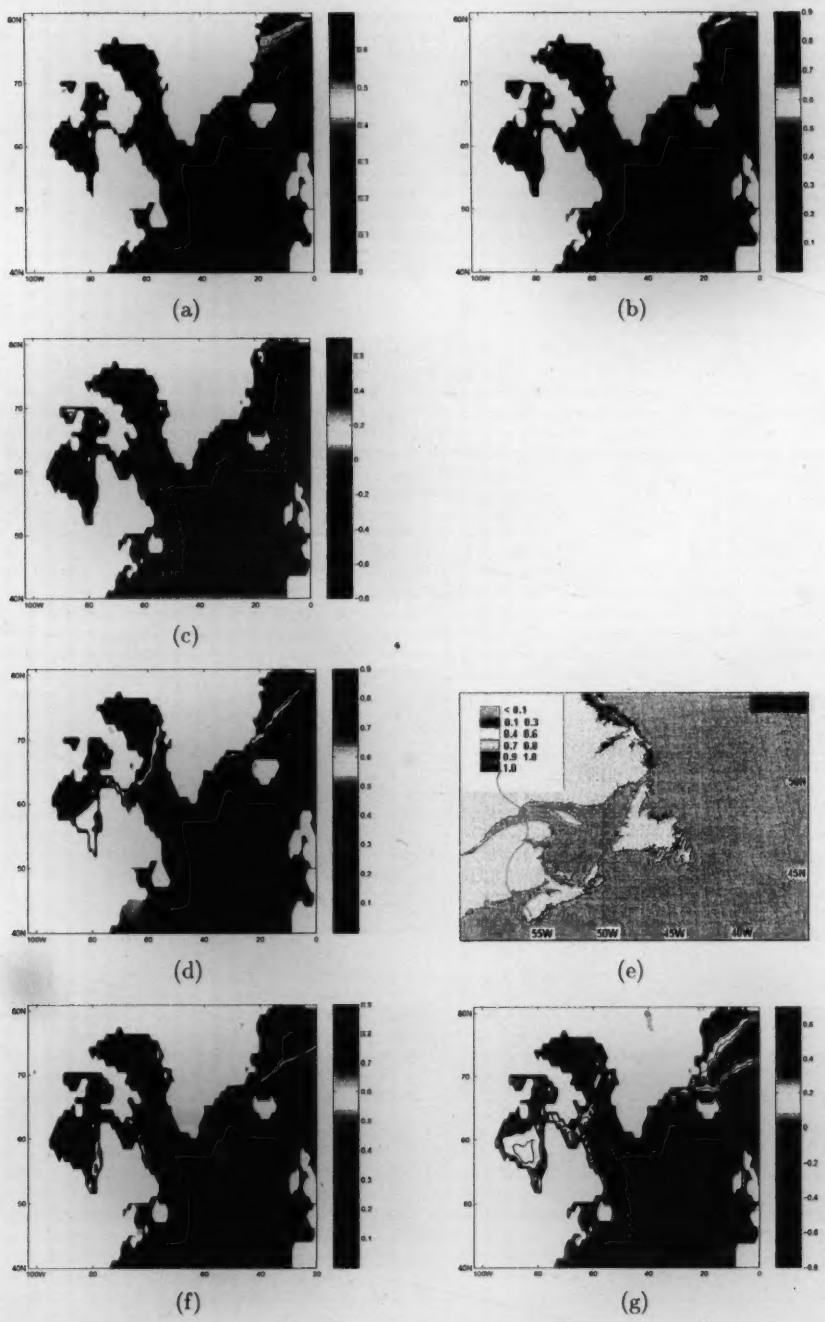

Figure 5.1: Sea ice concentration ($\times 100\%$) during September in (a) Walsh (1978) observation, (b) SDVar and (c) difference (SDVar-Walsh (1978)). September CIS sea ice concentration is not available. Also shown is sea ice concentration ($\times 100\%$) during December in (d) Walsh (1978) observation, (e) CIS observation, (g) SDVar (h) difference (SDVar-Walsh (1978)).

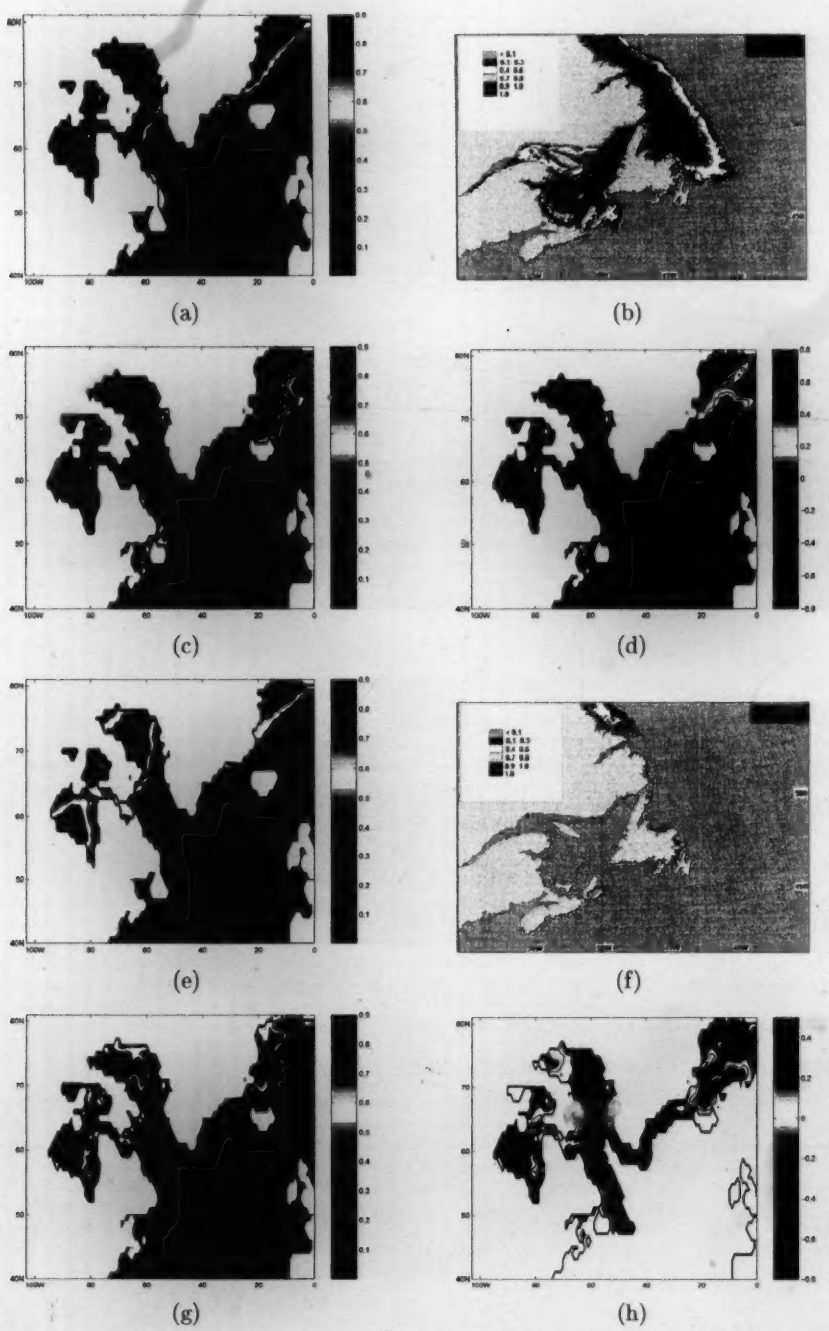

Figure 5.2: Sea ice concentration ($\times 100\%$) during March in (a) Walsh (1978) observation, (b) CIS observation, (c) SDVar (d) difference (SDVar-Walsh (1978)). Also shown is sea ice concentration ($\times 100\%$) during June in (e) Walsh (1978) observation, (f) CIS observation, (g) SDVar (h) difference (SDVar-Walsh (1978)).

CIS data shown).

In December (Figs. 5.1d,e,f,g) the model and observations are in close agreement as far as sea ice fields are concerned in the Baffin Bay, Davis Strait, Foxe Basin, Hudson Bay, and eastern Labrador coast except for tighter sea ice edges in the model. The coarser resolution Walsh (1978) ice edges (Fig. 5.1d) are broader with a gradual increase of concentrations from open water to over 90% concentration while SDVar (Fig. 5.1f) does not have such a gradual transition. In the Foxe Basin and Hudson Bay, the 90% concentration contour in SDVar (Fig. 5.1f) has a larger coverage than the Walsh (1978) data. Comparison of SDVar in terms of both structure and concentration magnitudes with CIS data (not shown), especially the position of the 90% concentration contour, shows much closer agreement. CIS data along a portion of the Labrador coast is shown in Fig. 5.1e. It shows ice concentrations of upto 90% near the coast, which is in closer agreement with SDVar (shows concentration of upto 70%) than Walsh (1978) data (shows concentration of upto 40%).

In March (Figs. 5.2a,c,d) Hudson Bay, Baffin Bay and Foxe Basin are completely covered with sea ice concentrations of over 90% in both SDVar and the Walsh (1978) data. The sea ice edges in the Walsh (1978) data (Fig. 5.2a) are still not as tight as in SDVar (Fig. 5.2c). As a result the difference plot (Fig. 5.2d) shows that SDVar is an underestimate by as much as 80% concentration. Comparison of CIS data (not shown) with SDVar shows that the 90% concentration contours between the two are in better agreement. Along the Eastern Canadian coast to just south of Newfoundland (into the Gulf of St. Lawrence), sea concentrations as high as 90% are observed in SDVar (Fig. 5.2c) and CIS data (Fig. 5.2c), but completely missing in the Walsh (1978) data (Fig. 5.2a).

In June (Fig. 5.2e,g) sea ice on the Eastern Canadian coast is absent in the model when compared with the Walsh (1978) data which has concentrations of about 40%. Sea ice concentrations of about 40-60% is also present along Eastern Labrador coast

in CIS data (Fig. 5.2f) since it is an early June average plot. Later during most parts of June, CIS data (not shown) does not have sea ice present as in SDVar. The model also slightly overestimates the sea ice concentrations in Baffin Bay and eastern Hudson Bay with some underestimation present in western Hudson Bay when compared with the Walsh (1978) data but is more in agreement with CIS data (not shown).

5.3.2 Sea ice thickness

The monthly sea ice thickness (Figs. 5.3a,b,c,d) patterns follow closely the sea ice concentration fields. Smooth spatial distribution of thickness magnitudes are hard to compare with observations due to limited availability of sea ice thickness data. However, some sea ice thickness data exists in the GIN seas (Bourke and Garret, 1987) and a number of CIS sea ice thickness observing stations also exist in Hudson Bay, Baffin Bay and eastern Canadian coasts.

In the GIN seas the seasonal cylce of sea ice thickness follows closely observations of Bourke and Garret (1987). During September (Fig. 5.3a) along the northeastern Greenland coast a maxima of over 3.5 m is observed which gradually reduces to about 0.5 m near 74^{o}N at Eastern Greenland coast, in close agreement with Fig. 5.3 of Bourke and Garret (1987). In December, the 0.5 m contour moves further south to about 65^{o}N at the Eastern Greenland coast, also consistent with Fig. 4 of Bourke and Garret (1987). By winter, in Denmark Strait (between Greenland and Iceland) the thickness have increased to 1.5 m with the 0.5 m contour spreading all the way down to the southern tip of Greenland. The model is consistent with Bourke and Garret (1987) data which unfortunately only extends upto Denmark Strait. One major discrepancy between the model and the observation is that there is an underestimation by about 0.5-1m thickness in the Denmark Strait in the model. By June (Fig. 5.3d) the thickness in the Denmark Strait has decreased and the ice has retreated northwards along the East Greenland coast, though a slight underestimation is evident when

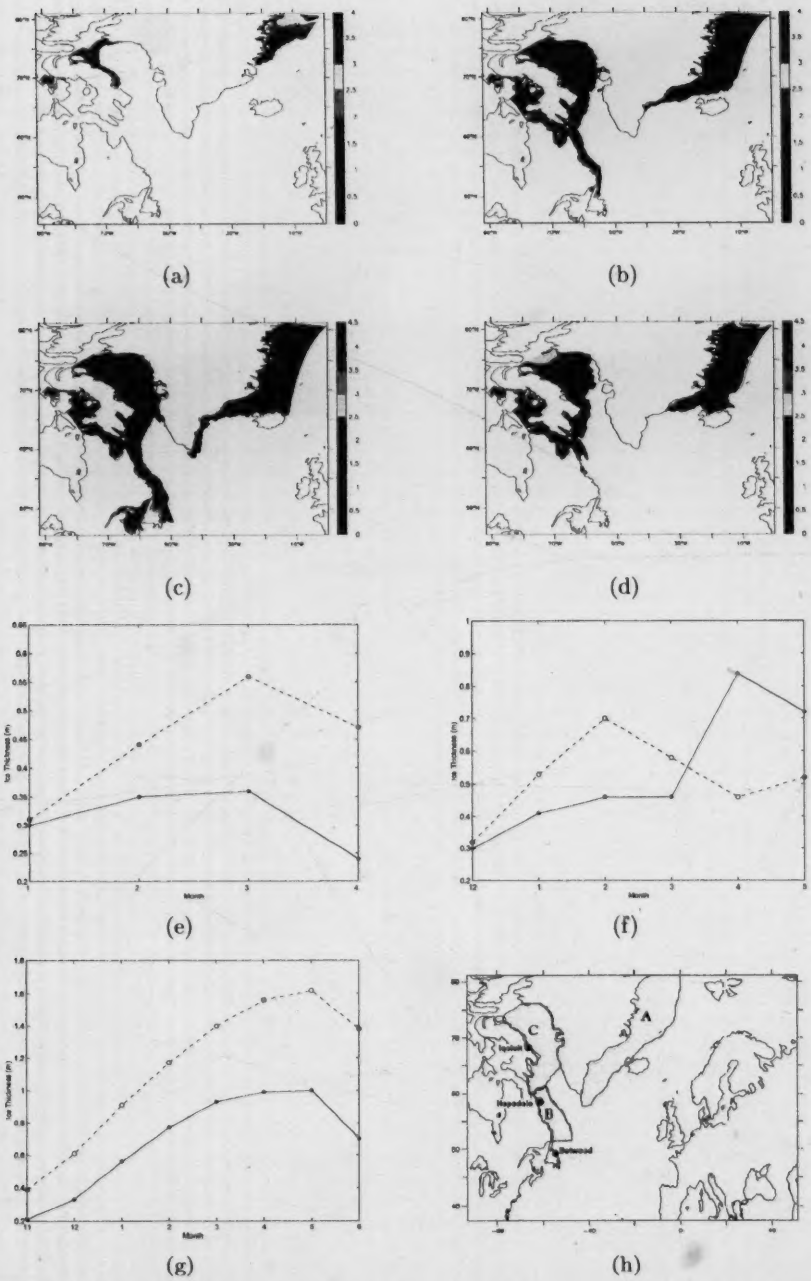

Figure 5.3: Sea ice thickness (m) in SDVar during (a) September, (b) December, (c) March and (d) June. Also shown is sea ice thickness (m) in SDVar (solid) and observation (dashed) calculated at (e) Botwood, (f) Hopedale and (g) Iqaluit. Panel (h) shows the location of stations Botwood, Hopedale and Iqaluit together with regions A (East Greenland), B (West Greenland) and C (Labrador Slope).

compared with Fig. 2 of Bourke and Garret (1987).

For comparison along the Eastern Canadian coast the Bourke and Garret (1987) data is not as detailed as the CIS thickness data. As such three stations in Eastern Canada from CIS data are used. A model and observational comparison of CIS data but of different stations with a different model has been also done previously in Brown and Cote (1992). In this study three stations Botwood (49.2°N, 54.7°W), Hopedale (55.5°N, 59.8°W), and Iqaluit (63.7°N, 67.5°W) are used. They are labelled in Fig. 5.3h. At Botwood monthly means for the months January-April are calculated from weekly observations from years 1974-1995 and plotted in Fig. 5.3e together with the SDVar monthly means. Similary Hopedale is obtained from the years 1960-1984 (Fig. 5.3f) and Iqaluit is obtained from the years 1975-1999 (Fig. 5.3g). Generally, the sea ice thickness magnitudes have been underestimated at all the three locations, except for Hopedale where there is some overestimation in April and May. At Botwood the underestimation is by 1-20cm which is equivalent to 3-49% underestimation whereas at Hopedale underestimation is by 2-24cm (6-34%). The largest underestimation is at the northernmost station Iqaluit of 20-70cm (33-49%). At any particular time, the sea ice thickness mangitudes increase northwards and correspondingly we can also observe that the sea ice thickness represenation in the model gets poorer with increasing latitude. Nevertheless, although the thickness magnitudes are under-represented in the model, the phase of sea ice thickness has been well captured by the model especially at Botwood and Iqaluit.

The three stations in the eastern Canadian coast when compared with CIS data and model output show a general underestimation of sea ice thickness magnitude but a general agreement with phase, except maybe at Hopedale. A similar problem is evident along the eastern Greenland coast especially in the Denmark Strait when model output is compared with Bourke and Garret (1987) data. Sea ice thickness is controlled by thermodynamic parameterisations in the LIM sea ice model. Hence it

appears that the sea ice model still inadequately represents thermodynamic processes which affect vertical growth and decay of sea ice (that subsequeantly affect its thickness) such as bottom and top of ice surface heat fluxes, approximation of the heat diffusion equation, and several ice constants. Improvements in thermodynamic parameterizations may be possible in the future by considering a multi-category ice thickness model (Lipscomb, 2001) which removes the physically unrealistic assumption in LIM model that sea ice has a single uniform thickness in each grid cell. Dynamic factors such as mean ocean surface currents could be also playing a role since changes in pathways of colder currents such as East Greenland Current and Labrador Current would affect the heat fluxes at the bottom of the ice. Further under-representation of sea ice in the model especially in north Baffin Bay could be due to the closed domain at the north end of Baffin Bay and thus lacking any input of ice from the Canadian Arctic Archipelago. As far as CIS observations are concerned, the data at the three locations (Hopedale, Botwood and Iqaluit) range from 1960-1999. CIS data especially from the period 1960-1988 coincided with lower North Atlantic Oscillation (NAO) index (Hurrel, 1995), implying colder conditions on the Canadian coast, probably leading to thicker ice in the observations while the model is using climatological forcing averaged over the years 1958-2004.

5.3.3 Sea ice extent

The sea ice extents are calculated for three regions: A (East Greenland), B (Labrador coast) and C (Western Greenland) as shown in Fig. 5.3h. Fig. 5.4 shows the annual monthly mean seasonal cycle of sea ice extent in our model compared with the available digitized sea ice extent data of Walsh (1978). Sea ice extent is not compared in areas south of region B as it appears from Figs. 5.1,5.2 that the coarse resolution data of Walsh (1978) is unreliable in this region.

In region A (Fig. 5.4a) the winter ice extent has been overestimated in SDVar

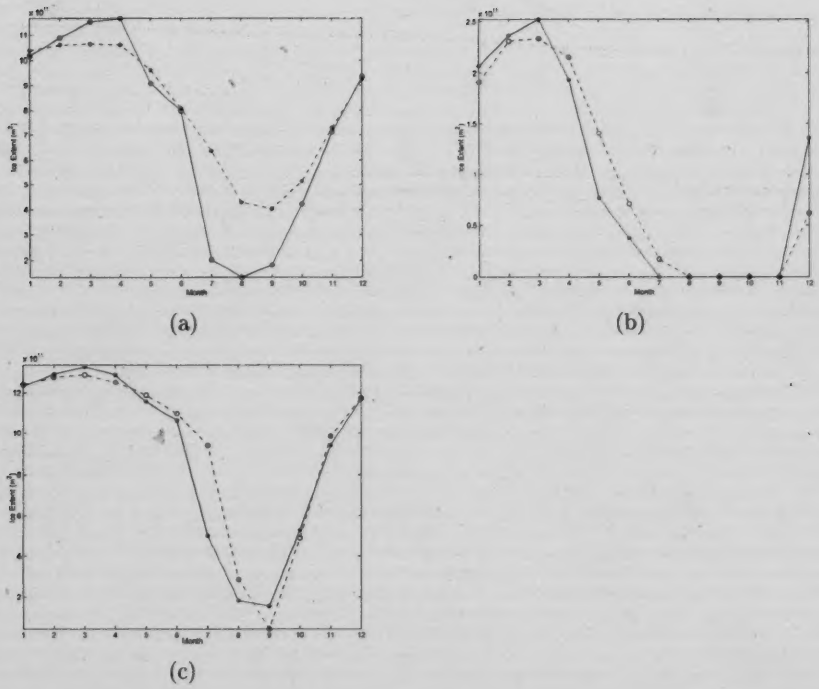

Figure 5.4: The sea ice extent (m^2) in SDVar (solid) and observation (dashed) calculated in region (a) A (East Greenland Coast) (b) B (Labrador Coast) (c) C (West Greenland).

by about 9% while in summer (especially during July-October) the ice extent is significantly underestimated, with a maximum underestimation of 68% occuring in July. In region B (Fig. 5.4b) the winter ice extent has been overestimated in SDVar by about 7% while the ice extent underestimation starts just after March with a maximum of 50% underestimation occuring in May. Like the other regions, Region C (Fig. 5.4c) also experiences winter ice extent overestimation in SDVar by about 5%. In region C, underestimations range from May-August with a maximum of 47% underestimation occuring in July. Hence in all the three regions sea ice extent has been overestimated during winter (5-9%) and underestimated during summer (47-68%), with the summer underestimation being about 10 times larger than the winter overestimation. An examination of sea ice concentrations (especially contours close to 15%) in Walsh (1978) and SDVar (Figs. 5.1,5.2) show that in all the regions, largest differences are present in the structures of SDVar and Walsh (1978) during summer. Since ice extent is calculated using concentrations greater than 15% (which occur near ice edges) and we had seen large differences in ice edges between SDVar and Walsh (1978) in Figs. 5.1,5.2: this could explain further the differences in ice extents between SDVar and Walsh (1978) data. The phase of the sea ice extent in SDVar, however, in all the three regions are not affected by the low resolution Walsh (1978) data and are in close agreement with it.

5.4 Sensitivity Analysis

5.4.1 Sensitivity to oceanic assimilation

The sensitivity of sea ice to oceanic temperature and salinity assimilation through the hydrostatic equation (Zhai et al., 2004) is investigated in this section. A comparison is made between two experiments: SDVar which includes oceanic assimilation, and PVar which does not have any assimilation. A regional analysis (ie. regions A, B,

C representing Eastern Greenland, Labrador Slope and Western Greenland respectively as shown in Fig. 5.3h) of concentration, thickness, and extent is performed. Changes are observed between SDVar and PVar in each of these regions with varying degrees for each of the parameters examined.

In region A (Eastern Greenland coast) sea ice concentration (Fig. 5.5a) changes (of about 12%) are mostly evident along the sea ice edges especially southeast of Greenland. As far as areal coverage of concentration is concerned, Figs. 5.5b,c show a monthly distribution of the ice concentration versus area in SDVar and PVar, depicting maximum ice coverage area of about $5 \times 10^{11}\mathrm{m}^2$ in March. The difference plot (Fig. 5.5d) shows that there are areal changes of about $0.5 \times 10^{10}\mathrm{m}^2$ between the two runs during winter months, especially with respect to the 90-100% ice covered regions with differences peaking in March. Hence in March the areal difference ($0.5 \times 10^{10}\mathrm{m}^2$) between the two experiments is about 1% of the total ice covered area ($5 \times 10^{11}\mathrm{m}^2$). An examination of the thickness changes shows that differences of about 15 cm (Fig. 5.5e) are present along the ice edges especially in the southeastern part of Greenland. Unlike sea ice concentration the thickness differences in Region A extend beyond winter months (March-June; Fig. 5.5f), with the maximum areal difference in the two runs (Fig. 5.5f; $0.42 \times 10^{10}\mathrm{m}^2$) close to the areal difference ($0.5 \times 10^{10}\mathrm{m}^2$) in concentration fields.

In region B (Labrador coast) sea ice concentration (Fig. 5.5a) changes (of about 6%) are mostly evident along the sea ice edges especially in the southern half of this region. As far as areal coverage of concentration is concerned, Figs. 5.6a,b show a monthly distribution of the ice concentration versus area in SDVar and PVar, depicting maximum ice coverage area of about $7 \times 10^{10}\mathrm{m}^2$ in March. The difference plot (Fig. 5.6c) shows that there are areal changes of about $5 \times 10^{9}\mathrm{m}^2$ between the two runs during winter months, especially with respect to the 90-100% ice covered regions with differences peaking in March. Hence in March the areal difference ($5 \times 10^{9}\mathrm{m}^2$)

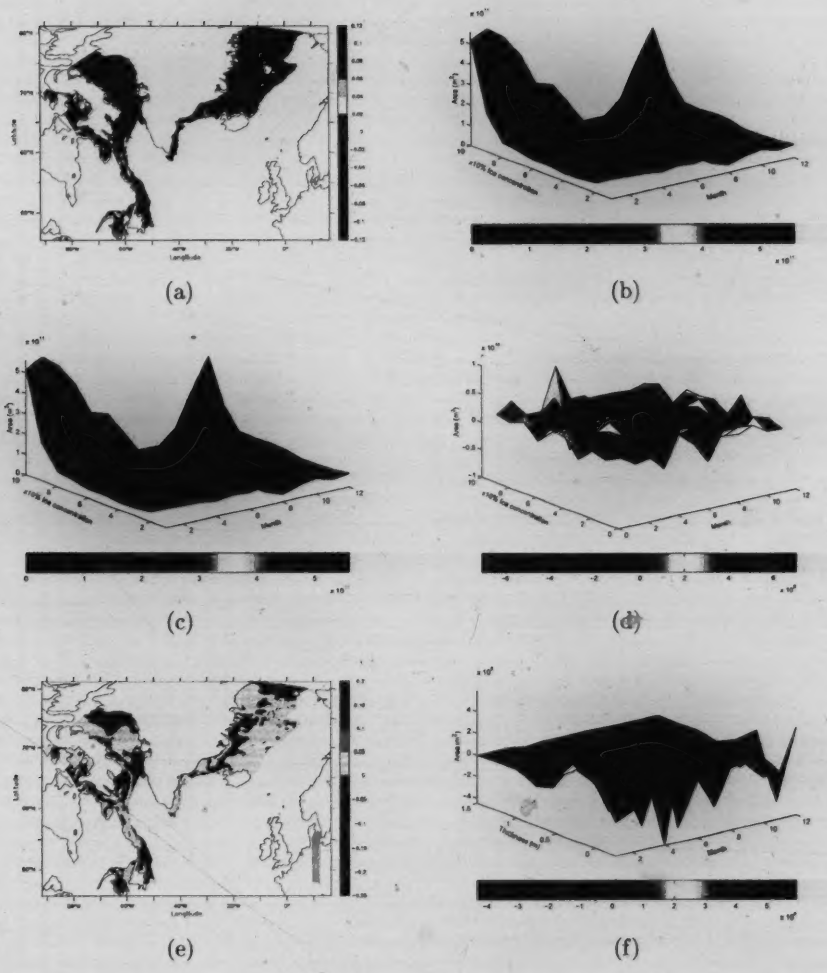

Figure 5.5: Shown is (a) March mean spatial plot of concentration differences (SDVar-PVar; $\times 100\%$), Also shown is region A (Eastern Greenland coast) areal extents of monthly mean distributions of sea ice concentrations (from 0 to 100%) in (b) SDVar ($0 - 5 \times 10^{11}\mathrm{m}^2$), (c) PVar ($0 - 5 \times 10^{11}\mathrm{m}^2$), and (d) SDVar-PVar ($-1 - 1 \times 10^{10}\mathrm{m}^2$). Also shown is (e) March mean spatial plot of thickness differences (SDVar-PVar; m), and (f) region A (Eastern Greenland coast) areal extent of monthly mean thickness (m) differences SDVar-PVar ($-4 - 4 \times 10^{9}\mathrm{m}^2$).

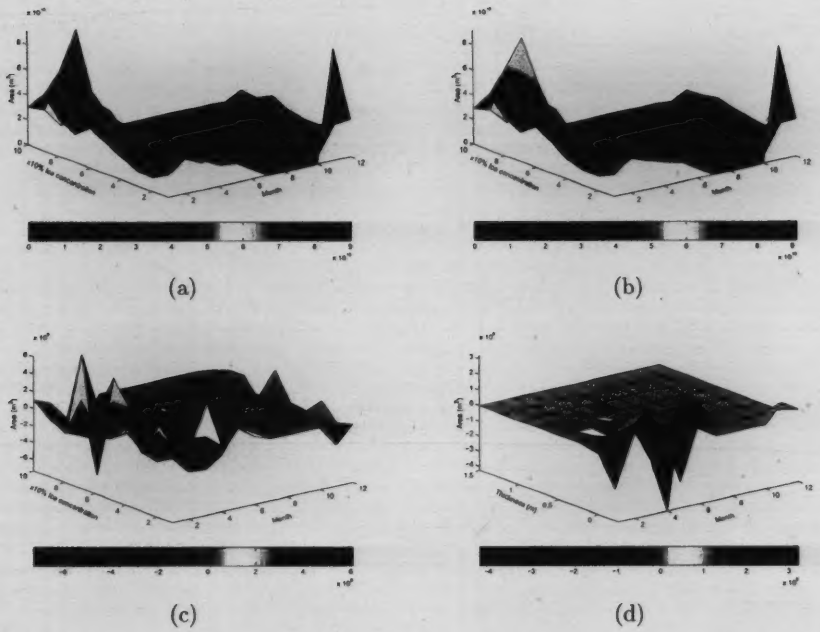

Figure 5.6: Shown is region B (Labrador coast) monthly mean distributions of sea ice concentrations (from 0 to 100%) in (a) SDVar, (b) PVar, and (c) SDVar-PVar. Also shown is (d) region B monthly mean distribution thickness (m) differences (SDVar-PVar).

between the two experiments is about 7% of the total ice covered area ($7 \times 10^{10}\mathrm{m}^2$). An examination of the thickness changes shows that differences of about 5 cm (Fig. 5.5e) are present along the ice edges. Unlike sea ice concentration the thickness differences in Region B extend beyond winter months (January-June; Fig. 5.6d), with the maximum areal difference in the two runs (Fig. 5.6d; $4.2 \times 10^9\mathrm{m}^2$) close to the areal difference ($5\times10^9\mathrm{m}^2$) in concentration fields.

In region C (Western Greenland coast) sea ice concentration (Fig. 5.5a) changes (of about 6%) are mostly evident along the sea ice edges especially southeast of Greenland. As far as areal coverage of concentration is concerned, Figs. 5.7a,b show a monthly distribution of the ice concentration versus area in SDVar and PVar, depicting maximum ice coverage area of about $7 \times 10^{11}\mathrm{m}^2$ in March. The difference

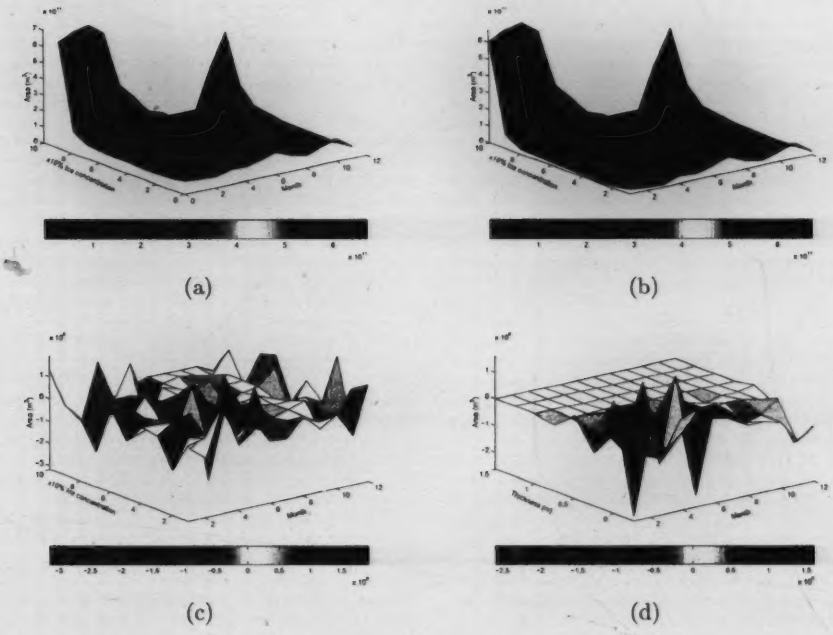

Figure 5.7: Shown is region C (Western Greenland coast) monthly mean distributions of sea ice concentrations (from 0 to 100%) in (a) SDVar, (b) PVar, and (c) SDVar-PVar. Also shown is (d) region C monthly mean distribution thickness (m) differences (SDVar-PVar).

plot (Fig. 5.7c) shows that there are areal changes from December to June over all the concentrations, with differences of about $3 \times 10^9 m^2$ peaking in March. Hence in March the areal difference ($3 \times 10^9 m^2$) between the two experiments is about 0.4% of the total ice covered area ($7 \times 10^{11} m^2$). An examination of the thickness changes shows that differences of about 15 cm (Fig. 5.5e) are present along the ice edges especially in the southeastern part of Greenland. The thickness differences in Region C also occur over the months December-June as in concentration (Fig. 5.7d), with the maximum areal difference in the two runs (Fig. 5.7d; $2.5 \times 10^9 m^2$) close to the areal difference ($3 \times 10^9 m^2$) in concentration fields.

In all cases the differences in the run with assimilation occur along the ice edge. Here, the ice is thinnest and thus small changes in oceanic temperatures and thus

ice-ocean heat fluxes will have the biggest effect on ice concentration. Although the areal extent of the changed regions are not large, they are potentially significant. By adding or removing the insolation effect of the sea ice, significant changes in the air/sea flux of upwards of 200 Wm^{-2} are observed. Such fluxes will significantly impact the overlying atmosphere (in a coupled situation), as well as properties and depth of the oceanic mixed layer. In an operational sense, small changes in the ice edge position and even ice thickness can play a significant role for users of a sea ice forecast. In all the regions the maximum sensitivity to oceanic assimilation is observed in winter months, peaking in March. The percentage change in sea ice concentration and thickness due to oceanic assimilation in March is 1%, 7% and 0.4% respectively for Regions A, B and C whereas maximum surface heat fluxes change respectively upto $200Wm^{-2}$, $120Wm^{-2}$, and $80Wm^{-2}$.

5.4.2 Sensitivity to eddy representation

In order to investigate the sensitivity to oceanic eddy representation on sea ice, a comparison is made between PVar (with improved eddy representation mentioned in section 5.2) and PCon (without improved eddy representation). A regional analysis of averages of concentration, thickness, extent, areal concentration and thickness changes together with surface heat fluxes and surface currents are shown in Figs. 5.8-5.11.

In region A (Eastern Greenland coast) sea ice concentration (Fig. 5.8a) changes (of up to 50%) are evident along the sea ice edges. A large drop in concentration of up to 50% is also observed in the GIN Seas. As far as areal coverage of concentration is concerned, Fig. 5.8b shows a monthly distribution of the ice concentration versus area in PCon, depicting maximum ice coverage area of about $5 \times 10^{11} m^2$ in March. The difference plot (Fig. 5.8c) shows that there are areal changes of about $5 \times 10^{10} m^2$ between the two runs (PVar and PCon) during winter months, especially with 90-100% ice covered regions in March. Hence in March the areal difference ($5 \times 10^{10} m^2$)

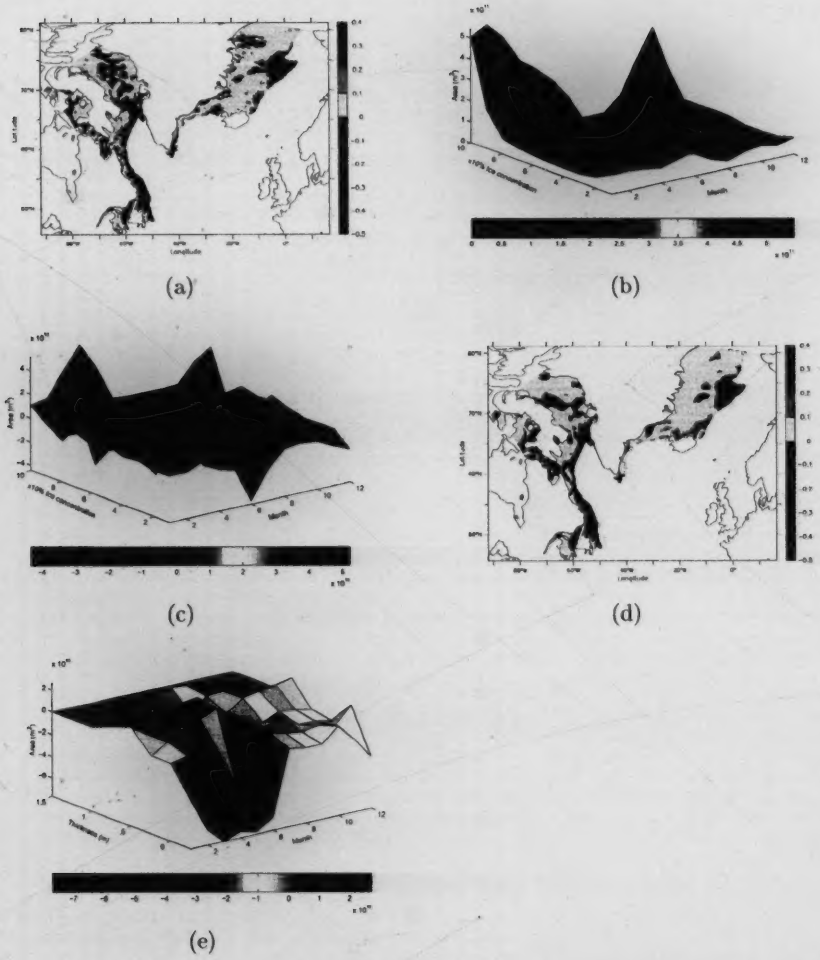

Figure 5.8: Shown is (a) March mean spatial plot of concentration differences (PVar-PCon; $\times 100\%$). Also shown is region A (Eastern Greenland coast) monthly mean distributions of sea ice concentrations (from 0 to 100%) in (b) PCon, and (c) PVar-PCon. Also shown is (d) March mean spatial plot of thickness differences (PVar-PCon; $\times 100\%$), and (e) region A (Eastern Greenland coast) monthly mean distribution thickness (m) differences (PVar-PCon).

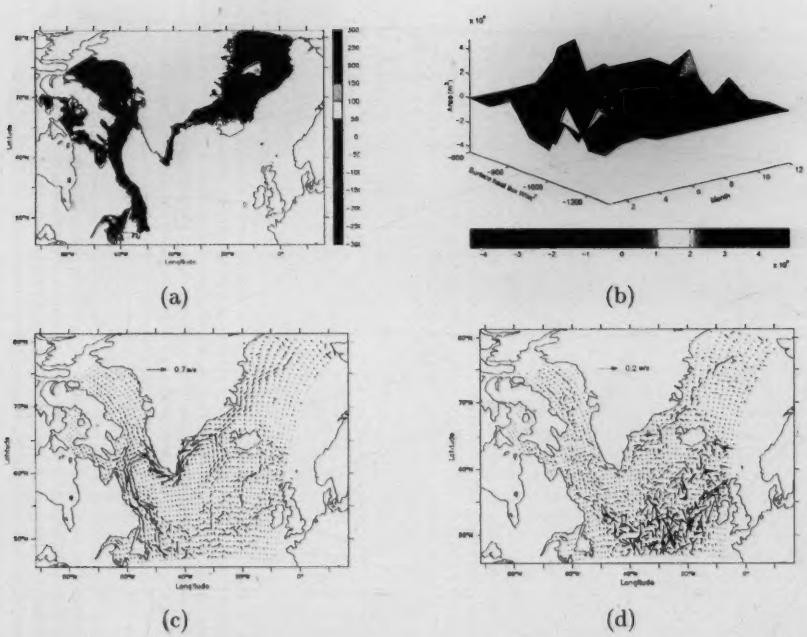

Figure 5.9: Shown is monthly mean spatial plots of differences (PVar-PCon) in (a) surface heat flux (Wm^{-2}) and (b) region A (Eastern Greenland coast) monthly mean distributions of surface heat flux (Wm^{-2}) in PVar-PCon. Also shown is annual mean ocean surface currents drawn at every 5 grid points in both meridional and zonal directions for (c) PCon, and (d) PVar-PCon.

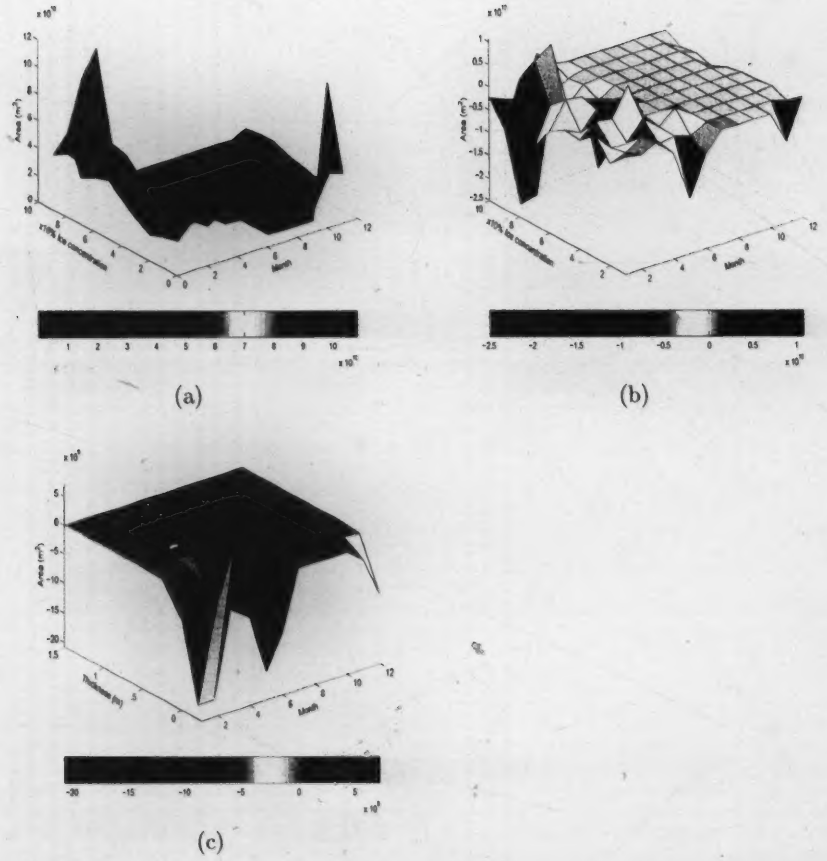

Figure 5.10: Shown is region B (Labrador coast) monthly mean distributions of sea ice concentrations (from 0 to 100%) in (a) PCon, and (b) PVar-Pcon. Also shown is (c) region B monthly mean distribution of thickness (m) differences in PVar-PCon.

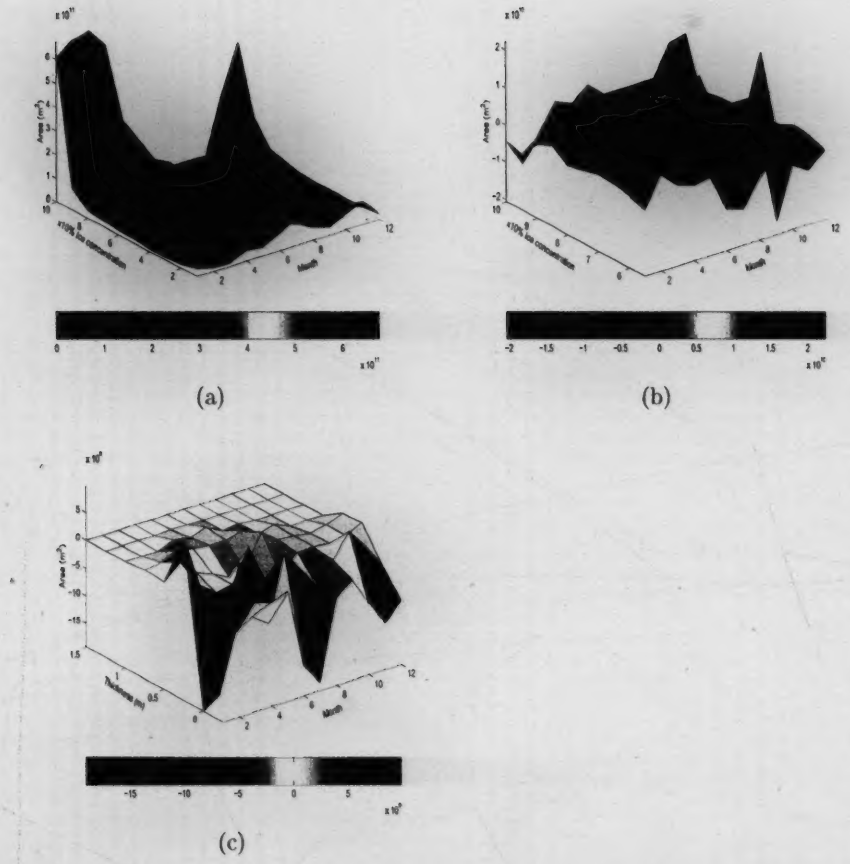

Figure 5.11: Shown is region C (Western Greenland coast) monthly mean distributions of sea ice concentrations (from 0 to 100%) in (a) Pcon, (b) PVar-Pcon. Also shown is (c) region C monthly mean distribution thickness (m) differences (PVar-Pcon).

between the two experiments is about 10% of the total ice covered area (5×10^{11}m^2). An examination of the thickness changes shows that differences of about 50 cm (Fig. 5.8d) exist along the ice edges, with a large reduction in the GIN Seas. Unlike sea ice concentration the thickness differences in Region A extend beyond winter months (March-June; Fig. 5.8e), with the maximum areal difference between the two runs (Fig. 5.8e; 8×10^{10}m^2) being slightly larger than the areal difference (5×10^{10}m^2) in concentration fields. An examination of surface heat fluxes (Fig. 5.9a) show changes of up to 300Wm^{-2} along the sea ice edges with a large change in the GIN seas, coinciding with the region that we had earlier observed that had changes in concentration and thickness fields. These changes in surface heat flux occur mostly around the winter months (January-April; Fig. 5.9b) over an area of about 0.4×10^{10}m^2.

In region B (Labrador coast) sea ice concentration (Fig. 5.8a) changes (of up to 50%) are evident along the sea ice edges. A large drop in concentration of up to 50% is also observed along Labrador coast ice edges. As far as areal coverage of concentration is concerned, Fig. 5.10a shows a monthly distribution of the ice concentration versus area in PCon, depicting maximum ice coverage area of about 10×10^{10}m^2 in March. The difference plot (Fig. 5.10c) shows that there are areal changes of about 2.5×10^{10}m^2 between the two runs (PVar and PCon) during winter months, especially with 90-100% ice covered regions in March. Hence in March the areal difference (2.5×10^{10}m^2) between the two experiments is about 25% of the total ice covered area (10×10^{10}m^2). An examination of the thickness changes shows that differences of about 30 cm (Fig. 5.8d) exist along the ice edges. Unlike sea ice concentration the thickness differences in Region A extend beyond winter months (March-June; Fig. 5.10c), with the maximum areal difference between the two runs (Fig. 5.10c; 2×10^{10}m^2) being slightly smaller than the areal difference (2.5×10^{10}m^2) in concentration fields. An examination of surface heat fluxes (Fig. 5.9a) show changes of up to 300Wm^{-2} along the sea ice edges, coinciding with the region that we had earlier

observed that had changes in concentration and thickness fields. These changes in surface heat flux occur mostly around the winter months (January-April; Fig. 5.10d) over an area of about $2\times10^9 m^2$.

In region C (West Greenland coast) sea ice concentration (Fig. 5.8a) changes (of up to 50%) are evident along the sea ice edges. A large drop in concentration of up to 50% is also observed along Davis Strait ice edges. As far as areal coverage of concentration is concerned, Fig. 5.11a shows a monthly distribution of the ice concentration versus area in PCon, depicting maximum ice coverage area of about $7 \times 10^{11} m^2$ in March. The difference plot (Fig. 5.11b) shows that there are areal changes between the two runs (PVar and PCon) spread over a number of months, with maximum changes of upto $2 \times 10^{10} m^2$ occuring in November. An examination of the thickness changes shows that differences of about 50 cm (Fig. 5.8d) exist along the ice edges. Unlike sea ice concentration, thickness differences in Region C has a maximum areal difference occuring in February between the two runs (Fig. 5.11c; $1.8 \times 10^{10} m^2$). An examination of surface heat fluxes (Fig. 5.9a) show changes of up to $200 Wm^{-2}$ along the sea ice edges, coinciding with the region that we had earlier observed that had changes in concentration and thickness fields. These changes in surface heat flux occur around the months December-June (Fig. 5.11d) over an area of about $2 \times 10^9 m^2$.

Hence the impact of improved oceanic eddy representation has a significant impact on sea ice properties such as concentration and thickness, arising from eddy heat fluxes at the front separating the ice covered boundary currents from the basin interiors. With a two way coupling between the ocean and sea ice, the modified sea ice characteristics eventually affect the ocean surface heat fluxes and surface currents too. In all the regions the maximum sensitivity to oceanic assimilation is observed in winter months. The percentage change in sea ice concentration and thickness due to oceanic assimilation in March is 10%, 25% and 10% respectively for Regions A,

B and C whereas maximum surface heat fluxes changes in all the regions are upto 300Wm^{-2}. The surface currents, with oceanic assimilation, change by upto 5-20 cm/s with the largest change occuring along Region A ice edges. Comparing the sensitivity of oceanic eddy parameterization to oceanic assimilation, the former has greater impact.

5.5 Summary and Conclusion

We have presented results from the NATL4 configuration of NEMO. The configuration produces a realistic large-scale reproduction of sea ice in terms of sea ice concentration, thickness and extent in the North Atlantic. The results are sensitive to both oceanic eddy parameterization and oceanic data assimilation, implying that improving subgridscale parameterization and oceanic data assimilation can lead to improvements in dynamics and thermodynamics of the ocean surface which in turn contributes to the sea ice fields and vice versa.

In this study two observational datasets from the Canadian Ice Service (CIS) and the Walsh (1978) are compared with model output. Walsh (1978) climatology is not as detailed as CIS climatology in the Eastern Canadian coast due to its low resolution. However, the Walsh (1978) data has a larger spatial coverage than CIS data. The seasonal cycle of sea ice concentration in the model agrees reasonably well with the CIS data. Along the Eastern Canadian sea ice edges, the major differences between the model and Walsh (1978) data are due to the Walsh (1978) data having low ice concentration (0-30%) present along the ice edges. In Eastern Greenland, the tongue of sea ice protruding into the Greenland Sea is missing in Walsh (1978) data, leading to a large discrepancy. Comparison with Comiso (1999) dataset cited in Timmermann et al. (2005) shows that the model does reasonably well. In fact, the coarse resolution model of Timmermann et al. (2005) completely missed the tongue of sea ice that is

present in our model study.

The thickness data was compared with three stations on the eastern Canadian coast. An overall underestimation of sea ice thickness magnitude was found in the model. A similar problem was also found along the eastern Greenland coast especially in the Denmark Strait when the model output was compared with Bourke and Garret (1987) data. The differences in the model and observations have been attributed to a number of reasons such as the observed CIS data used in this study being biased towards a phase of NAO, deficiencies in the LIM model in adequately parameterizing thermodynamic processes and having closed ocean boundaries in northern Baffin Bay. However, sea ice extent phase agrees overall with the Walsh (1978) data.

Comparing the performance of our model output with earlier studies, we find that some of the model deficiencies mentioned in Melia (2002) and Timmermann et al. (2005) are overcome in this study. The Melia (2002) study had lack of sea ice that was seen during March in Labrador Sea while in summer overestimation of sea ice was present in Baffin Bay in Timmermann et al. (2005). Further during September Melia (2002) had overestimated ice concentration in Denmark Strait and GIN seas while Timmermann et al. (2005) had also overestimated ice concentration in this region during winter.

Two sensitivity studies are also performed in this study. One sensitivity study utilizes the semidiagnostic method of Zhai et al. (2004) to assimilate temperature and salinity into the ocean model. Our results show that this approach has an impact on sea ice. Hence, it appears that the hydrographic changes brought about by the oceanic assimilation are significant enough to impact the sea ice fields. Since the ocean and sea ice components in our model have a two way coupling, the changes to sea ice fields eventually affect the ocean surface heat flux and currents too. Improved representation of oceanic eddy processes through the utilization of a variable eddy transfer coefficient (Visbeck et al., 1997) in the Gent and McWilliams (1990) parame-

terization also shows significant impact on sea ice characteristics. An increase in mean concentration and thickness is observed along Eastern and Western Greenland coasts while a decrease is observed along Labrador coast. Significant differences is evident in the surface fluxes, and surface currents especially along sea ice edges. In both sensitivity studies, Region B (Labrador Coast) has the largest change in concentration and thickness fields.

Sea ice is a critical component of the climate because it strongly influences albedo, surface turbluent heat fluxes, surface wind drag and upper-ocean stratification (Alexander et al., 2004; Ogura et al., 2004). Thus changes in sea ice strongly impact local climate variability and could potentially alter the global climate through changes in the thermohaline circulation. Hence accurate representation of sea ice in models is important, with the role of oceanic eddies being a factor to be significantly considered.

5.6 Acknowledgements

This work is supported by the Natural Sciences and Engineering Research Council of Canada, & CFCAS grants awarded to PGM (CLIVAR & GOAPP).

Bibliography

[1] Alexander, M.A.; U.S. Bhatt; J.E. Walsh; M.S. Timlin; J.S. Miller and J.D. Scott. 2004. The atmospheric response to realistic arctic sea ice anomalies in an AGCM during winter. *J. Clim.*, 17: 890-905.

[2] Adcroft, A.; C. Hill and J. Marshall. 1997. Representation of topography by shaved cells in a height coordinate ocean model. *Mon. Weather Rev.*, 125: 2293-2315.

[3] Brown, R.D. and P. Cote. 1992. Interannual variability of landfast ice thickness in the Canadian high arctic 1950-89. *Arctic*, 45: 273-284.

[4] Comiso, J. 1999. Bootstrap sea ice concentrations for NIMBUS-7 SMMR and DMSP SSM/I. National Snow and Ice Data Center, Boulder, CO, USA. Digital media.

[5] Cuny, J.; P.B., Rhines; P.P. Niiler and S. Bacon. 2002. Labrador Sea boundary currents and the fate of the Irminger Sea Water. *J. Phys. Oceanography*, 32: 627-647.

[6] Deacu, D., and P.G. Myers. 2005. Effect of a variable eddy transfer coefficient in an eddy-permitting model of the Sub-Polar North Atlantic. *J. Phys. Oceanography*, 35: 289-307.

[7] Fichefet, T. and Morales Maqueda M.A. 1997. Sensitivity of a global sea ice model to the treatment of ice thermodynamics and dynamics. *J. of Geophys. Res.* 102: 12609-12646.

[8] Gent, P.R. and J.C. McWilliams. 1990. Isopycnal mixing in ocean circulation models. *J. of Phys. Oceanography,* 20: 150-155.

[9] Goosse, H., and T. Fichefet. 1999. Importance of ice-ocean interaction for the global ocean circulation: A model study. *J. Geophys. Res.* 104 (C3): 23337-23355.

[10] Hurrel, J.W. 1995. Decadal trends in the North Atlantic Oscillation: regional temperatures and precipitation, *Science*, 269: 676-679.

[11] Lipscomb, W.H. 2001. Remapping the thickness distribution in sea ice models, J. Geophys. Res. 106 (C7): 13989-14000.

[12] Ogura, T.; A. Abe-Ouchi; H. Hasumi. 2004. Effects of sea ice dynamics on the Antarctic sea ice distribution in a coupled ocean atmosphere model. *J. Geophys. Res.* 109: C04025, doi: 10.1029/2003JC002022.

[13] Rothrock, D.A., J. Zhang, Y. Yu. 2003. The arctic ice thickness anomaly of the 1990s: a consistent view from observations and models. *J. Geophys. Res.* 108 (C3): 3082, doi: 10.1029/2001JC001208.

[14] Sarmiento, J. L., and K. Bryan. 1982. An ocean transport model for the North Atlantic. *J. Geophys. Res.* 87(C1): 394-408.

[15] Sheng, J.; R.J. Greatbatch; D.G. Wright. 2001. Improving the utility of ocean circulation models through adjustment of the momentum balance. *J. Geophys. Res.* 106: 16711-16728.

[16] Theetten, S. and A.M. Treguier. 2004. Validation and analysis of the first NATL4 run of the DRAKKAR project. Laboratoire de Physique des Oceans, CNRS-Ifremer-UBO, Brest, France, Internal report DOPS/LPO 05-01.

[17] Visbeck, M.; J. Marshall; T. Haine; M. Spall. 1997. Specifications of eddy transfer coefficients in coarse-resolution ocean models. *J. Phys. Oceanography* 27: 567-580.

[18] Walsh, J.E. 1978. A data set on northern hemisphere sea ice extent. World Data Centre-A for glaciology (snow and ice), glaciological data, part I, tech Report GD-2.

[19] Zhai, X.; R.J. Greatbatch; J. Sheng. 2004. Diagnosing the role of eddies in driving the circulation of the northwest Atlantic ocean. *Geophys. Res. Lett.* 31: L233304, doi: 10.1029/2004GL021146.

[20] Zhang, J; W.D. Hibler III; M. Steele; D.A. Rothrock. 1998. Arctic Ice-ocean modelling with and without climate restoring, J. Phys. Oceanography 22: 191-217.

Chapter 6

General Discussion and Conclusion

A number of experiments have been performed with the Subpolar Ocean Model (SPOM; Myers, 2002) and the Nucleus for European Modeling of the Ocean (NEMO; Madec et al., 1998) coupled ocean-sea ice model, to answer questions raised in the introductory chapter of this thesis. The main objectives of this study were to improve SPOM and NEMO models and then to utilize them for scientific process studies of the North Atlantic ocean and sea ice. We have answered questions pertaining to model drift, role of oceanic data assimilation, and role of subgridscale parameterization on computed ocean hydrography and circulation. The role of oceanic eddies in heat and freshwater transports are also investigated by utilizing the SPOM model, while the role of different water masses in the subpolar gyre (especially the Labrador Sea Water (LSW) and Subpolar Mode Water (SPMW)) and their interaction and effect on the meridional overturning circulation (MOC) are assessed using the NEMO model. Improved oceanic subgridscale parameterization and oceanic data assimilation are implemented in NEMO model and their effect on sea ice properties such as concentration, thickness and extent are studied.

We have focussed on an important issue facing eddy-permitting models of the North Atlantic: maintaining a correct salinity field in the central Labrador Sea. Con-

siderable degradation of (computed) water mass characteristics has been found in both high resolution modeling studies of the North Atlantic (Treguier et al., 2005) and low-resolution eddy-permitting models of the subpolar North Atlantic (Boning et al, 1996; Willebrandt et al., 2001; Myers and Deacu, 2004). Comparing two solutions of the NEMO model with different water formation regimes to examine this problem, we note a gradual progression of Subpolar Mode Water (SMPW) properties from the eastern subpolar gyre to the Labrador Sea through Cape Farewell, implying the eastern subpolar gyre as a possible source of Labrador Sea salinification. A reduction in LSW density, formation rate, salinity, and maximum mixed layer depths arise from changes in water formation properties in the eastern subpolar gyre leading us to conclude that changes in SPMW propagate to LSW and affect its formation. The results of this study are important because, apart from showing a source of the spurious salinization of Labrador Sea, we show that improved eddy pararameterization improves an eddy-permitting ocean general circulation model. Improvement in subgridscale parameterization is achieved through the implementation of a variable eddy transfer coefficient (Visbeck et at., 1997) for the Gent-McWilliams (GM) parameterization (Gent and McWilliams, 1990). In this scheme the constant eddy transfer coefficient used to simulate eddy-induced tracer transports (Gent and McWilliams, 1990) is replaced by a spatially and temporally varying eddy transfer coefficient. Deacu and Myers (2005) had earlier implemented this scheme in the SPOM model and found that it improved the representation of salinity in the Labrador Sea to some extent.

On the role of SPMW on LSW, an important issue that has arisen from this study is that in order to improve LSW one of the options is to improve the circulation and hydrography of the eastern subpolar gyre. We have not looked at specifically improving the eastern subpolar gyre in this study, though two of the schemes that we implemented have an effect on the entire subpolar gyre. Hence there is a need for further studies of the eastern subpolar gyre to improve our understanding of the

processes that effect the eastern subpolar gyre: both oceanic and atmospheric. As far as atmospheric forcings are concerned, the property changes in the SPMW (Thierry and Mercier, 2007) are North Atlantic Oscillation (NAO) driven changes, hence our improved understanding of the NAO would affect the understanding of SPMW. On the role of other forcings such as precipitation minus evaporation (P-E) fluxes, some studies (Josey and Marsh, 2005; Gonzalez-Pola et al., 2005; Myers et al., 2007) show an increased role of P-E in the region while other studies (Thierry et al., 2007; Hatun et al., 2005; and Holliday, 2003) exclude any role of such fluxes on SPMW. This contradiction shows that we still need further studies to understand the processes in this region. Net heat fluxes (Hakkinen and Rhines, 2004) and wind stress (Boning et al 2006) also affect the strength of the subpolar gyre, hence further sensitivity studies with several data sets need to be carried out in order to provide our model with improved surface forcing data sets.

As far as model drift is concerned, for an almost complete removal of model drift we have shown that we need another technique known as oceanic data assimilation. As in Deacu and Myers (2005), we found that improved subgridscale parameterization on its own only partially removes model drift. A combined approach of improved oceanic eddy parameterization and a recent semi-diagnostic method (Zhai et al., 2005) when implemented in the SPOM model is found to reduce the drift in freshwater content of the Labrador Sea almost completely and also improves the circulation of the subpolar North Atlantic. This method utilizes the climatological temperature and salinity fields to adjust the momentum balance of the model, while leaving the tracer equations fully prognostic and unconstrained. The combined subgridscale parameterization and data assimilation approach is just a natural extension. When improved subgridscale prameterization and oceanic data assimilation are implemented independently, we do not observe a large improvement.

On the role of oceanic eddies in heat and freshwater transport, the combined ap-

proach improves the representation of total and eddy heat and freshwater transports equally well, in agreement with observations, highlighting the importance of their role in the subpolar gyre circulation. A number of studies (eg. Katsman et al., 2004) show enhanced eddies associated with the Irminger Current (IC) that transport the SPMW into the interior of Labrador Sea. Improved representation of the IC eddies would improve the freshwater and heat content of the Labrador Sea. As suggested by our NEMO modeling study, these improvements could be due to the improved SPMW being transported into the Labrador Sea. Although we have shown the role of improved subgridscale parameterization and oceanic data assimilation in the SPOM model, further study needs to be done to determine if the role of the combined approach is not model specific and is transferable to other regions: hence the approach needs to be implemented in the NEMO model, for example, to determine if we get results similar to SPOM model. Since NEMO does not have a strong surface temperature and salinity relaxation as SPOM, examination of NEMO results would also highlight the role of strong surface relaxations on model drift. Hence further studies could also perform a comparative analysis of the differences and similarities in an ocean only model (SPOM) and a coupled ocean sea ice model (NEMO).

The role of improved eddy subgridscale paramterization and oceanic data assimilation on sea ice was also studied in the NEMO model. Sensitivity studies performed showed that the sea ice in the model is sensitive to both oceanic eddy parameterization and oceanic data assimilation, with sensitivity to former being more than the latter. We also noted our improved configuration (with improved eddy subgridscale parameterization and oceanic data assimilation) reproduced a realistic large-scale spatial and seasonal sea ice in terms of sea ice concentration, thickness and sea ice extent, in agreement with a number of observational data sets used. Our eddy permitting study has also captured important ice features along Eastern Canadian and Greenland coasts, a deficiency observed in the few previous coupled ocean-sea ice modeling

studies in this region. In some of our comparisons (eg. sea ice extent) we have used Walsh's (1978) coarse resolution data which has been found unreliable. Hence future work needs to use high resolution sea ice data with open domains near Baffin Bay and the Canadian Archipelago. Validation with observations should utilize longer time series (eg. Canadian Ice Service data) such that there is no bias towards any phase of NAO. There is also demand for sea ice thickness observations to validate the results of our modeling study. Since we observed a general underestimation in ice thickness by NEMO, one suggestion is to couple a multi-category ice thickness model (Lipscomb, 2001) to the ocean component of NEMO.

In this study, in summary we have looked at the role of freshwater and salt transport on the composition of the Labrador Sea. In our experiment with the NEMO model, we looked solely at the role of the salty IC on LSW. We have not examined the role of fresher boundary currents (East Greenland Current (EGC) and Labrador Current (LC)) on LSW formation. There is room for further research to identify the contribution from these currents in reducing salinity drift in eddy-permitting models. Preliminary analysis shows that the contribution from such sources is not as significant as that from the IC originating from eastern subpolar gyre. However, EGC and LC currents carry meltwater from Arctic or Greenland sea ice and as such it is worth quantifying the role of these two freshwater boundary currents on Labrador Sea salinification. At the onset of summer, there is a large contribution of freshwater from melting sea ice, the impact of this freshwater source on Labrador Sea salinification is an area that needs to be looked into. Other sources of freshwater in the North Atlantic include export of sea-ice from the Arctic Ocean (Dickson et al., 2006; Myers et al., 2005), river runoff (Peterson et al., 2002), and melt from the Greenland ice cap (Steffen et al., 2004).

Bibliography

[1] Boning, C.W., Holland, W.R., Bryan, F.O., Danabasoglu, G., McWilliams, J.C.,1995. An overlooked problem in model simulations of the thermohaline and heat transport in the Atlantic ocean. Journal of climate 8, 515-523.

[2] Gent, P.R., McWilliams, J.C., 1990. Isopycnal mixing in ocean circulation models. Jounal of Physical Oceanography 20, 150-155.

[3] Madec, G., Delecluse, P., Imbard, M., Levy, C., General circulation model reference manual, Notes de l'IPSL, Universite P. et M. Curie, B102 T15-ES, 4 place Jussie, Paris cedex 5, N°11, 91p, 1998.

[4] Myers, P.G., 2002. SPOM: A regional model of the sub-polar North Atlantic. Atmosphere-Ocean 40, 445-463.

[5] Myers, P.G. 2005: Impact of freshwater from the Canadian Arctic Archipelago on Labrador Sea Water formation, Geophysical Research Letters, 32, L06605, doi:10.1029/2004GL022082.

[6] Peterson, B.J., Holmes, R.M., McClelland, J.W., Vorosmarty, C.J., Lammers, R.B., Shiklomanov, A.I., Shikomanov, I.A., Rahmstorf, A., 2002. Increasing river discharge to the Arctic Ocean. Science 298, 2171-2173.

[7] Steffen, K., Nghiem, S.V., Huff, R., Neumann, G., 2004. The melt anomaly of 2002 on the Greenland Ice Sheet from active and passive microwave satellite observations, Geophysical Researh Letters, 31.

[8] Treguier, A.M., Theetten, S., Chassignet, E.P., Penduff, T., Smith, R., Talley, L., Beismann, J.O., Boning, C., 2005. The North Atlantic subpolar gyre in four high resolution models. Journal of Physical Oceanography 35, 757-774.

[9] Visbeck, M., Marshall, J., Haine, T., Spall, M., 1997. Specifications of eddy transfer coefficients in coarse-resolution ocean models. Journal of Physical Oceanography 16, 680-693.